Characteristics of polar lows in the Nordic Seas and the impact of orography and sea ice on their development

A thesis submitted to the
School of Environmental Sciences
of the
University of East Anglia
in partial fulfilment of the requirements for the degree of
Doctor of Philosophy

Denis Sergeev

August 2018

Abstract

Polar lows in the Nordic Seas have been examined through a case study based on unique observations gathered during a field campaign, numerical simulations, sensitivity experiments with altered orography and sea ice cover, and a climatology based on objective tracking and two reanalysis products.

A detailed analysis of a shear-line polar low has been presented using comprehensive observations from a research aircraft, dropsondes, the ASCAT scatterometer, and the CloudSat radar; in conjunction with convection-permitting simulations performed with the Met Office Unified Model. High winds to the north and west were within the cold-air mass and associated with large surface turbulent heat fluxes and convective clouds. This suggested that barotropic instability manifested by mesoscale waves coalescing into polar low's centre, and diabatic processes, were important for its intensification. The model generally captured the polar low structure well — in particular the thermodynamic fields and the strength of the horizontal shear. The spatial structure of the convective cloud bands was simulated reasonably well, but the model significantly underestimated the liquid water content and height of the cloud layers compared to observations.

Through sensitivity simulations of two typical Nordic Sea polar lows, it was found that Svalbard blocked Arctic air masses, and acted as an additional source of cyclonic vorticity aiding polar low development. A decrease in sea ice near Svalbard resulted in a moderate intensification of the polar lows, while an increase in sea ice significantly hindered their growth. These environmental changes modified the polar lows' tracks and development, but did not eradicate them.

A new climatology has been compiled from nine extended winters using two reanalyses: ERA5 and ERA-Interim. Mesoscale cyclones were tracked by an objective vorticity-based method. Compared to ERA-Interim, ERA5 reproduces the spatial distribution of cyclone density more like those from satellite-based studies, as it is able to resolve the wind field gradients with higher fidelity. An increase of polar lows near Scandinavia was found and there is tentative evidence that this is a result of sea ice loss in the northern Nordic Seas.

Contents

List of Figures

List of Tables

List of Acronyms

ACCACIA	Aerosol-Cloud Coupling And Climate Interactions In The Arctic
ASCAT	Advanced Scatterometer
ASR	Arctic System Reanalysis
AVHRR	Advanced Very High Resolution Radiometer
CAO	Cold Air Outbreak
CAPE	Convective Available Potential Energy
CISK	Conditional Instability Of Second Kind
CMIP5	Coupled Model Intercomparison Project Phase 5
ECMWF	European Centre For Medium-Range Weather Forecasts
FAAM	Facility For Airborne Atmospheric Measurements
GTS	Global Telecommunication System
IFS	Integrated Forecast System
IWC	Ice Water Content
LHF	Latent Heat Flux
LWC	Liquid Water Content
NWP	Numerical Weather Prediction
OLR	Outgoing Long-wave Radiation
PL	Polar Low
PMC	Polar Mesoscale Cyclone
PV	Potential Vorticity
SAR	Synthetic Aperture Radar
SHF	Sensible Heat Flux
SLP	Sea Level Pressure
SST	Sea Surface Temperature
STARS	Sea Surface Temperature And Altimeter Synergy For Improved Forecasting Of Polar Lows
TWC	Total Water Content
WISHE	Wind-induced Surface Heat Exchange

Acknowledgements

I would like to sincerely thank Ian Renfrew for giving me the chance to obtain a PhD in the topic I am deeply fascinated about, for inspiring supervision, for preparing me for the future career in science, and for all the British humour present in the meetings. I have been fortunate to participate in the IGP field campaign; thanks to Ian for organising it. Massive thanks go to Thomas Spengler, teaching me to ask the right research questions and greatly helping me to develop as a scientist; as well as making me to leave my computer to go sailing in Bergen or hiking in Davos. I am also grateful to Steve Dorling for his encouraging advice and stimulating discussions at supervisory meetings. Thanks to Annick for joining me at numerous conferences and having thought-provoking rants about dynamic meteorology, the Universe, and Everything. I would like to thank my examiners, Tom Bracegirdle and Ben Webber, for an interesting and stimulating viva.

It was a great privilege to have been given the opportunity to study at the University of East Anglia, and I express my deep gratitude to the School of Environmental Sciences for awarding me the Lord Zuckerman scholarship, as well as providing financial support to travel to conferences and summer schools. Thanks to EnvEast for financing my little Python language training bootcamp.

Big thanks to all in 3.16 and beyond for making this journey a fun and pleasant one. Thanks to Marina, Michael, Elise, Peter, Stuart, Helen, Richard, Andy, *et al.* for being awesome comrades, whether during endless procrastination in the gym, getting the MetUM to run without errors, on memorable nights out on Prince of Wales road, completing a (half-)Tough Mudder, flying on an research aircraft in Iceland, or just having a nice cuppa in the office.

To my Mum, my Dad, and my brother Oleg I say a huge thank you for years of encouragement and support, and for visiting me on these faraway shores. Above all, I would like to thank my dear wife Maria, for being my soul mate and my reviewer number zero, for her infinite love, care, and understanding.

1

Introduction

1.1 Background and motivation

Polar lows (PLs) continue to receive considerable attention in modern dynamic meteorology, attracting scientists by the complexity and non-linearity of processes driving them. From an aesthetic perspective, these mesoscale vortices are amongst the most visually striking of all atmospheric phenomena on the planet (Fig. 1.1). What are PLs and why are they important?

The generic term is *polar mesoscale cyclone (PMC)*, which includes all maritime tropospheric sub-synoptic-scale cyclones developing poleward of the main polar front (Rasmussen and Turner, 2003). PLs comprise a subclass of the most intense PMCs and are usually defined as meso-α-scale cyclones accompanied by surface winds near or above gale force (15 m s^{-1}). The horizontal scale is given according to Orlanski's classification of mesoscale systems and corresponds to approximately 200–1000 km in diameter (Orlanski, 1975). Thus, PLs are smaller than typical mid-latitude cyclones, and the weakest of them can even fall into meso-β-scale category (20–200 km). Compared to mid-latitude or tropical cyclones, PLs exhibit a short lifetime, typically only 3–36 h (Renfrew, 2003), although occasionally they last for more than 2 days (e.g. Claud et al., 2004). The main focus of the present study is PLs, though in Chapter 4, the climatology includes PMCs too.

The distribution of PLs around the planet favours certain regions, which are prone to marine cold air outbreaks (CAOs). The latter happens when cold and dry continental air mass is advected over relatively warm, mostly ice-free waters (Papritz and Spengler, 2017). As Fig. 1.2 shows, in the Northern Hemisphere PLs usually develop in

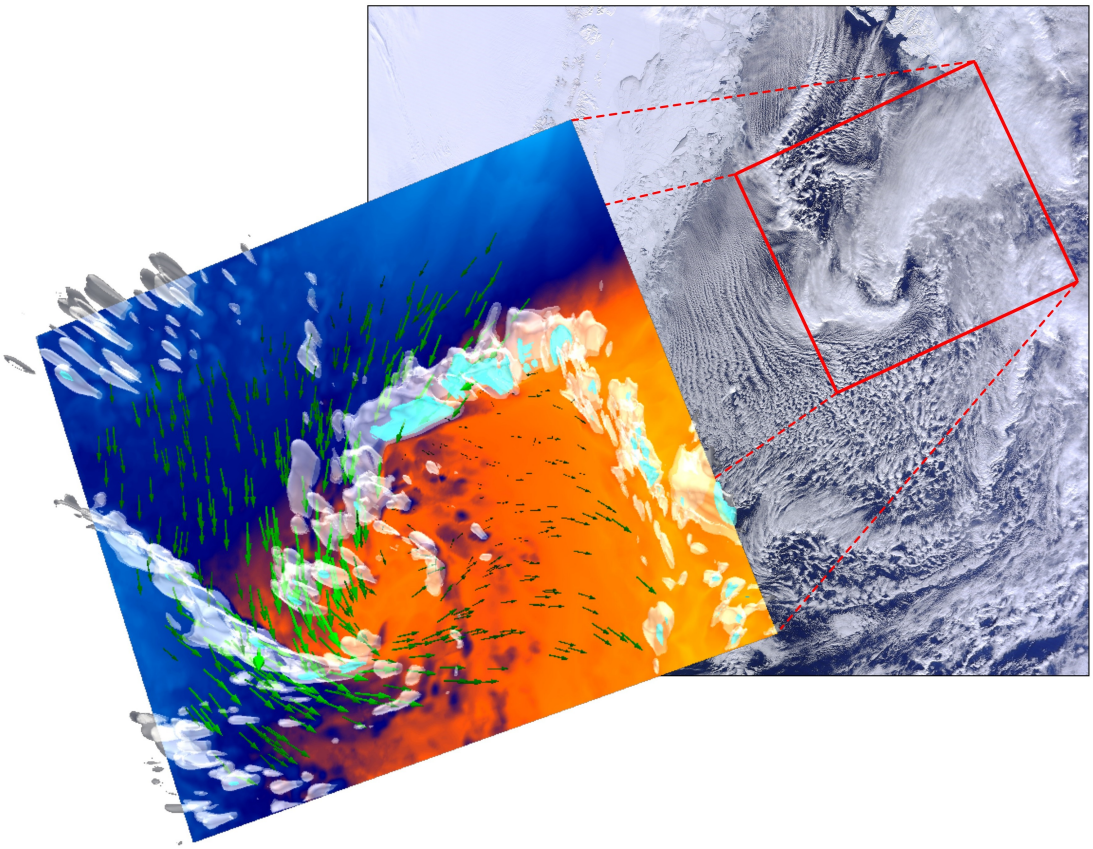

FIGURE 1.1: The shear-line PL, which developed during the Aerosol-Cloud Coupling And Climate Interactions in the Arctic (ACCACIA) field campaign and described in Chapter 2. The background image shows the cloud signature captured by the MODIS instrument in true colour (Provided by NEODAAS Satellite Receiving Station, Dundee University). The 3D image shows a model simulation of the PL, including the wind field (green arrows), potential temperature in lower troposphere (blue to orange colours), total cloud (white colours) and frozen (cyan colours) water.

the Nordic Seas (the Greenland, Iceland, Norwegian and Barents Seas), Hudson Bay, the Labrador Sea, the Bering Sea, the Sea of Okhotsk and the Japan Sea (e.g. Noer et al., 2011; Albright et al., 1995; Pagowski and Moore, 2001; Kolstad, 2011; Yanase et al., 2016; Stoll et al., 2018). In the Antarctic region, the Bellingshausen, and to a lesser extent the Amundsen and the Davis Seas are regular locations of mesoscale cyclogenesis (Verezemskaya et al., 2017; Stoll et al., 2018).

A seasonal cycle in PL occurrence is more distinct in the Northern Hemisphere with prevalence of PL between November and April (Blechschmidt et al., 2009; Stoll et al., 2018), designating them as a predominantly wintertime phenomenon, although Harold et al. (1999a) mention summertime occurrence too. In the Southern Hemisphere, the austral winter maximum is less pronounced. As for low-frequency changes, climatologies exhibit strong interannual variability, but weak decadal variability both for North Atlantic (Zahn et al., 2008; Michel et al., 2018) and North Pacific (Chen and Storch, 2013) PLs.

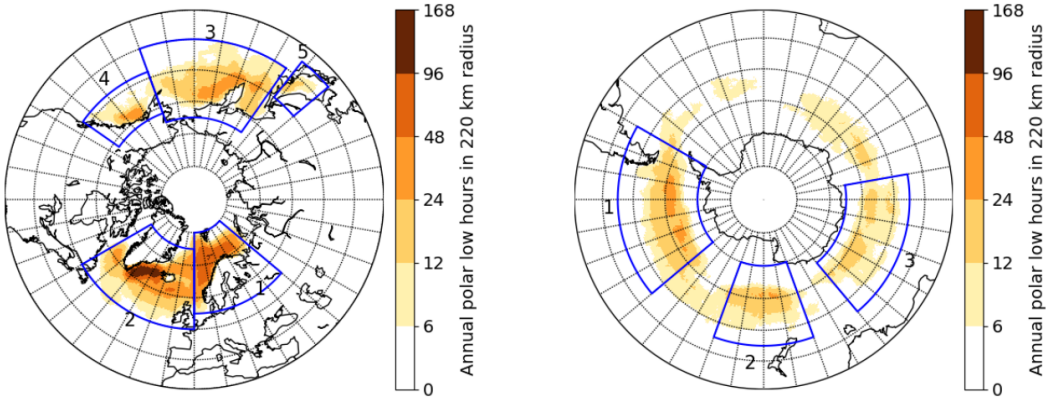

FIGURE 1.2: Spatial distribution of the average annual PL duration within a radius of 220 km for (left) the Northern and (right) the Southern Hemisphere derived from ERA-Interim (Stoll et al., 2018).

Our study focuses on the Nordic Seas area (Fig. 1.3). The position of warm ocean currents and the distribution of sea ice makes this region favourable for the formation of PLs (see Sec. 1.3). Moreover, a rapid decline in Arctic sea ice is observed in this area (Cavalieri and Parkinson, 2012) and is predicted to continue towards the end of the twenty-first century (Overland and Wang, 2007). This opens shorter and potentially more economically viable trade routes between Atlantic and Pacific ports (Melia et al., 2016). The PL occurrence in this area is likely to affect the safe passage of ships. In addition, oil and gas exploitation is active throughout the year, including winter months, and the most intense PLs can constitute a significant threat to these offshore activities.

From the point of view of the coupled atmosphere-ocean climate system, the Nordic Seas are an important region of heat exchange with the overlying atmosphere (e.g. Moore et al., 2015a). Mesoscale cyclones have been reported to affect the open-ocean convection (Condron and Renfrew, 2013), which leads to the formation of deep water masses. Changes in PL activity can have an integrated effect on the strength of thermohaline circulation, and thus potentially on the whole climate system (Marshall and Schott, 1999).

PLs have been known to explorers and inhabitants of polar regions as fierce storms that appeared seemingly out of nowhere and brought devastation to ships and coastal settlements. Even nowadays, heavy snow and hail showers, strong wind gusts and high waves, icing and thunderstorms are often associated with intense PLs (Rojo et al., 2015), and present potential risks to the growing maritime traffic, fishing, petroleum industries and other activities in high-latitude seas. Polar regions are notorious for the scarcity of in situ observations. This means that small-scale and rapidly developing weather systems such as PLs are often not captured by monitoring networks. As a result, PLs are challenging to forecast even for modern numerical weather prediction (NWP) models. Furthermore, the lack of high-resolution observational data hinders

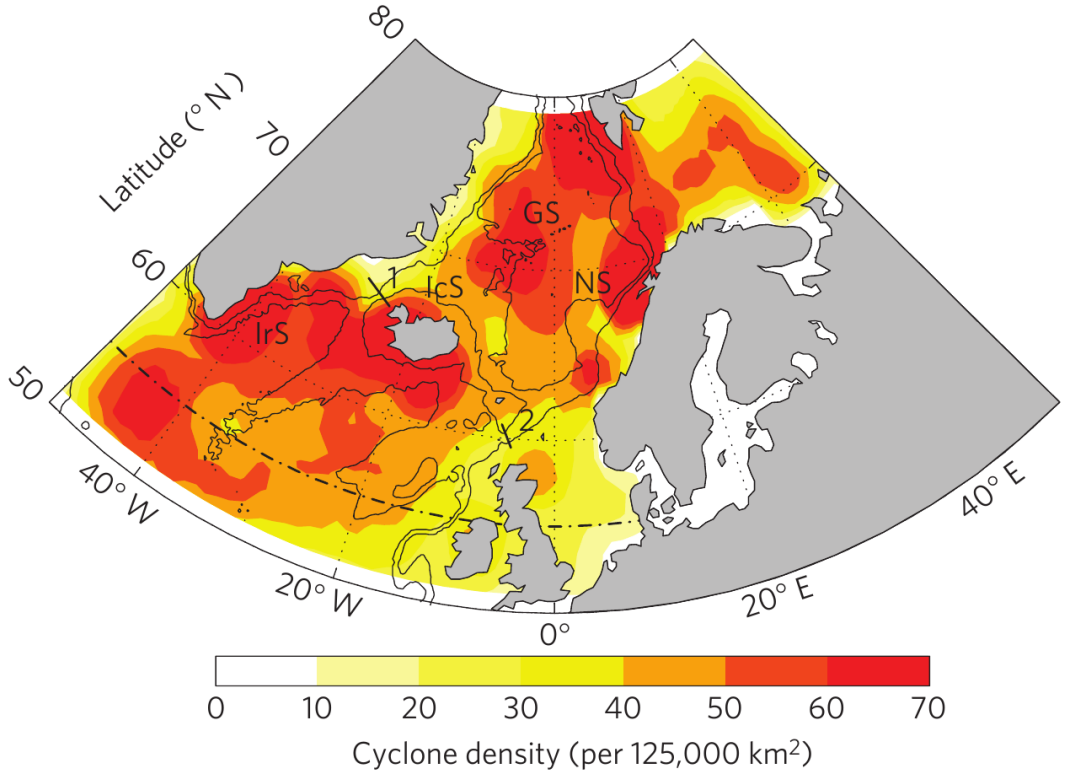

FIGURE 1.3: The annual mean density of PLs (shading, per 125.000 km^2) over the northeast Atlantic Ocean from Condron and Renfrew (2013). The density is averaged over 1978–1998. The locations of the Greenland (GS), Norwegian (NS), Iceland (IcS) and Irminger (IrS) Seas are marked.

our understanding of the dynamical mechanisms involved in the development of PLs.

While some targeted flights through PLs have been undertaken by research aircraft, such endeavours are very expensive and there is always the difficulty of having the aircraft in the right place at the right time. Only a handful of PL events have been investigated by research aircraft, but these cases provide otherwise unobtainable details of the three-dimensional structure of PLs and their temporal evolution (e.g. Shapiro et al., 1987; Douglas et al., 1991; Brümmer et al., 2009; Føre et al., 2011).

To some extent, the shortage of observations is alleviated by the growing volume of various satellite products. Infrared satellite imagery was in fact the basis for early PL research, including case studies, e.g. the 'most beautiful PL' (Nordeng and Rasmussen, 1992), as well as climatologies (e.g. Wilhelmsen, 1985). Several studies have demonstrated the benefits of satellite retrievals for PL studies, especially when images from several different sensors are combined (e.g. Heinemann, 1996; Claud et al., 2004). Ocean wind vectors estimated by scatterometers provide crucial information about the structure of near-surface circulation in mesoscale cyclones and other severe maritime weather events (Valkonen et al., 2017). Furevik et al. (2015) showed that synthetic aperture radar (SAR) brings added value of high-resolution wind speed estimates, resolving such finescale features of PLs as shear lines and low-level jets (Fig. 1.4). A

new tool for studying PL cloud composition has become available with the launch of the CloudSat satellite. CloudSat measures radar reflectivity versus altitude in a nadir slice along the satellite track (Tourville et al., 2015). To the author's knowledge there are no PL investigations based on CloudSat data except for a short note by Forsythe and Haynes (2015).

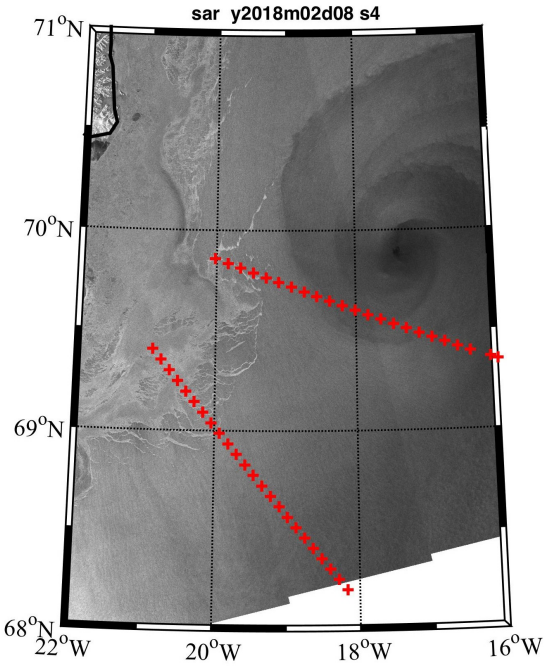

FIGURE 1.4: SAR image of a PL that developed on 8 February 2018 during the Iceland Greenland seas Project (IGP) field campaign, in which the author was lucky to participate. Red crosses indicate sections of oceanographic observations. SAR data are downloaded from `www.polarview.aq/arctic`. Image courtesy G. W. K. Moore.

Ideally, a complete portrait of PLs is achieved by combining direct observations from aircraft or ships with all available satellite data. Such a study is presented as the first part of this thesis for a PL event that unfolded during the ACCACIA field campaign in late March 2013 (Fig. 1.1). The study amalgamates various satellite and in situ observations with NWP simulations, allowing us to look at the PL in full detail.

Throughout the life cycle of this PL a number of dynamical mechanisms played a role, which is in fact typical for many mesoscale cyclones. It is now accepted in the scientific community, that there is a spectrum of PLs with convective systems on one end of the spectrum, and baroclinic on the other end (Rasmussen and Turner, 2003). The development mechanisms are briefly discussed in the next section.

1.2 Development mechanisms

One of the distinctive hallmarks of PLs is the spiral of cloud bands, resembling their tropical counterparts in satellite images. More often than not these cyclones have a

warm core and sometimes a clear 'eye' in the centre. On the other hand, PLs may have well-defined fronts and a comma-shaped cloud structure, suggesting similarity with mid-latitude synoptic cyclones. Dynamically, intense PLs are hybrid systems: their development is usually attributed to a mix of baroclinic and convective processes, the relative contribution of which can vary during a PL life cycle. In other words, a PL can transform from one type to another during its life cycle, shifting along the baroclinic-convective spectrum (Carleton and Carpenter, 1990; Nielsen, 1997). Purely barotropic mesoscale cyclones tend to remain weaker and smaller, but may help to spin up a PL at the early stages of their development.

In addition, PLs typically have multiscale structure. Several meso-β-scale and meso-γ-scale vortices can be embedded in a PL, suggesting that the development of these weather systems is affected simultaneously by the large-scale environment and small-scale processes, e.g. cumulus convection (Watanabe and Niino, 2014).

1.2.1 Baroclinic instability

Many instabilities of meteorological importance occur in a form of wave propagation. In general, an air current in the atmosphere has both horizontal and vertical wind shear. In terms of wave instability the flow can be unstable to small perturbations, which may grow due to barotropic or baroclinic instability (Vallis, 2006). The former is associated with horizontal shear and its role in PL dynamics will be discussed later (see Sec. 1.2.2).

Baroclinic instability is associated with vertical shear of the mean flow. Vertical wind shear implies, via thermal wind balance, the existence of a horizontal temperature gradient on an isobaric surface. From an energetics viewpoint, this results in the uneven distribution of potential energy, that can be converted to kinetic energy, i.e. atmospheric motion. The conversion happens when the warm air ascends and simultaneously cold air sinks, relocating the centre of mass and providing a relaxation of the basic state potential energy gradient.

The role of baroclinic instability in the development of PLs was first explored via simple linear models, using normal mode techniques to examine the growth rates of disturbances of different wavelengths (e.g. Sardie and Warner, 1983). The pioneering work of Mansfield (1974) compared observations of a PL with a dry baroclinic model. Although the model included parameterizations of surface momentum and sensible heat fluxes, the assumed depth of perturbations was too low. Combined with the unrealistic absence of diabatic heating this error actually lead to a good match between observed and predicted perturbation features, allowing the author to claim that dry baroclinic instability largely accounts for PL dynamics. Another study on dry baroclinic waves and possible role of low static stability in the growth of PLs was by Duncan (1977). Duncan's quasi-geostrophic model was able to reproduce wave properties for two cases out of three. It was concluded that PLs could be considered

as shallow baroclinic waves and the required amount of energy was released in the lower troposphere when the low-level static stability was small. A similar approach was employed by Reed and Duncan (1987), who showed that the growth rate did not agree well with observed values. Together with Craig and Cho (1988) they noted the presence of widespread convection in the vicinity of PLs, which can reduce the static stability and shorten the wavelengths of the perturbations.

Thus, dry baroclinic instability theory was not successful in explaining PL development, so the next logical step was to include diabatic effects, such as air-sea interaction and latent heat release, into the theoretical models. Latent heating or cooling due to water phase transitions creates a local perturbation of temperature, changing the amount of available potential energy (which is proportional to temperature variance on isobaric surfaces). To test if PL development can be described by dry, moist baroclinicity or convective mechanisms (namely conditional instability of second kind, CISK), Sardie and Warner (1983) used a three-layer quasi-geostrophic model with a simple parameterization for latent heating. The overall result of their study was that neither CISK nor dry baroclinicity on their own were capable of reproducing the necessary growth characteristics. Further evidence for the crucial role of latent heat release for realistic PL development was provided by Craig and Cho (1988), who incorporated CISK into a simple model of baroclinic instability. This study demonstrated that not only the mere presence of latent heating is important, but also its amplitude. When the value of the diabatic heating is low, the baroclinic instability is affected by static stability of the atmosphere.

A different paradigm of baroclinic instability is the initial-value problem. This method is motivated by the recognition that in general the perturbations from which storms develop cannot be fully described as single normal mode disturbances — they tend to have a complex structure. The initial growth of such disturbance depends on the initial potential vorticity (PV) distribution (Hoskins et al., 1985). This so-called PV-thinking regards baroclinic instability as the interaction between PV anomalies at different levels. For example, PLs may often be initialised or reinforced by an upper-level precursor (PV anomaly), which induces growth near sea surface. To achieve rapid growth, an upper-level PV anomaly acts in synergy with a low-level baroclinic zone. The induced near-surface cyclonic circulation deforms the temperature field, creating its own PV anomaly. The upper-level and lower-level anomalies reinforce each other, resulting in reciprocal intensification (Renfrew, 2003).

Benefits of the PV approach come from the fact that PV is conserved for adiabatic and frictionless flow, and therefore its distribution in space can be derived from the stream function and temperature fields by assuming a balanced state. This method is called the invertibility principle and is reported in depth in (Hoskins et al., 1985). Its extension — piecewise PV inversion — allows one to estimate the contribution of different PV anomalies separately. A number of studies applied this method for various

atmospheric phenomena, including tropical and midlatitude cyclones. In the context of PL dynamics, recent works by Bracegirdle and Gray (2009), Nordeng and Røsting (2011), and Wu et al. (2011) have shown that the PV approach can be successfully used to identify the relative impact of local and remote PV anomalies in real PL cases. The PL in Bracegirdle and Gray (2009), for instance, was dominated by an upper-level PV anomaly only during the initial phase of its life cycle, while for the cases in the latter two studies the upper-level PV was crucial throughout their development. It should be noted that PV inversion assumes negligible contributions from the divergent component of the flow, which does not necessarily hold for intense mesoscale cyclones. Caution should be taken when using this technique (Egger and Spengler, 2018).

The combination of baroclinic instability and condensational heating from the PV viewpoint is a central concept of different models of cyclogenesis. Montgomery and Farrell (1992) envisaged PL development as a two-stage process, in which mutually beneficial interaction between upper- and lower-level PV anomalies followed by a diabatic destabilisation phase, when reduced static stability causes vortex stretching at low levels, enhancing PL vorticity.

Another conceptual model for PL development is an extension to the Type A & B cyclogenesis scheme of Petterssen and Smebye (Deveson et al., 2002). The type C cyclones that are the closest to a typical PL are characterised by pre-existing upper-level troughs, weak baroclinicity and large contribution from latent heat release (Bracegirdle and Gray, 2009). Bracegirdle and Gray (2008) found that approximately 31 % of the Nordic Seas PLs pass the threshold for type C cyclogenesis, the majority of which occur in the southern Norwegian Sea.

Yet another way to conceptualise the interaction of latent heat and baroclinicity is known as diabatic Rossby vortex (DRV). It was introduced by Parker and Thorpe (1995) and Moore and Montgomery (2005), and applied for idealised PL development by Terpstra et al. (2015). The DRV is fundamentally different from a dry baroclinic mode modified by moisture, because condensational heating plays a crucial role and presence of an upper-level anomaly is not required (Terpstra et al., 2015).

The studies discussed above established the concept that PLs often owe their growth to baroclinic processes acting in conjunction with diabatic effects. Indeed high-resolution numerical modelling has confirmed that latent heat acts to enhance growth rates and reduce wavelengths that reflects small scales and rapid development of PLs, in both idealised studies (Yanase and Niino, 2007; Adakudlu, 2012; Terpstra et al., 2015) and real case studies (Claud et al., 2004; Shimada et al., 2014; Watanabe and Niino, 2014).

1.2.2 Barotropic instability

Another type of wave instability in the atmosphere is barotropic instability, which is usually associated with horizontal wind shear. All the concepts discussed above generate kinetic energy through conversion from the available potential energy that

is created in a different way in each mechanism. In contrast, barotropic instability is driven at the expense of the large-scale kinetic energy. It may be expected to prevail for the development of relatively small (meso-β-scale) vortices when large vorticity values are concentrated in a narrow filament (Nagata, 1993). The number of PLs with barotropic instability being a key development mechanism is thought to be significantly less than the number of baroclinically or convectively driven ones (Rasmussen and Turner, 2003).

On the other hand, Rasmussen and Turner (2003) pointed out that PLs may form as 'shear vortices' in the shear zones west of Svalbard. Such shear lines are frequently observed to roll up forming numerous vortices on different scales, the largest of which may become a PL. Using a high-resolution model, Nagata (1993) simulated the formation of PMCs along a convergence zone over the Japan Sea. The disturbances were characterised by spiral cloud bands around dry and warm centres. The importance of barotropic instability was confirmed by comparing energy transformation rates over the strip region of high cyclonic vorticity.

Discussing the genesis and development mechanisms of a PMC over the Japan Sea, Watanabe and Niino (2014) demonstrated that cumulus convection contributes more to the development of the vortices than barotropic instability during the early development stages. Consequently, the PMC had a smaller horizontal wavelength than predicted by barotropic instability theory. In contrast, during the intermediate development stage, the cyclone acquired most of its kinetic energy from barotropic conversion. After exceeding a strength threshold, as it matured, the PMC changed its primary energy source from horizontal shear instability to 'a hurricane-like mechanism' (Watanabe and Niino, 2014).

It appears that such detailed kinetic energy analyses have not been carried out for PLs over the Nordic Seas. At the same time, theory and observations indicate the presence of series of vortices along narrow shear lines within cold-air outbreaks prior to PL developments (Rasmussen and Turner, 2003). Thus it may be anticipated that minor barotropic perturbations sometimes focus deep convection within a convectively or baroclinically unstable environment and trigger rapid growth of a PL.

1.2.3 Air-sea interaction and convective instability

Striking similarities between some PLs and tropical cyclones, such as spiraliform cloud bands and the presence of a clear 'eye of the storm', as visible on satellite images, suggest that development mechanisms may be similar too. This idea prompted some researchers to adapt hurricane development theories to high-latitude conditions. All of these theories are essentially based on the idea of air-sea interaction, since PLs spend most of their life cycle over the open ocean with its vast amount of energy ready to be released through enthalpy fluxes during cold-air outbreaks. The concept of air-sea interaction in PL dynamics, sometimes referred to as thermal instabilities (Rasmussen

and Turner, 2003) or convective instabilities (Renfrew, 2003) are briefly discussed in the present section.

To explain the maintenance of organised convection within a PL, conditional instability of the second kind (CISK or wave-CISK) was applied (e.g. Rasmussen, 1979; Økland, 1987; Craig and Cho, 1988). According to the CISK theory, an initial disturbance causes low-level convergence and ascent, which leads to latent heat release if the atmosphere is conditionally unstable[1]. The diabatic heating destabilises the environment, enhancing low-level convergence and upper-level divergence. This generates cyclonic vorticity, which reinforces low-level moisture pumping. The latter provides a continued source of latent heat and thus a positive feedback is established. The growth rate of a CISK-driven disturbance depends on the amount of convective available potential energy (CAPE). Several studies argued for the CISK mechanism to be active in PL dynamics, but a scrupulous examination of dropsonde soundings during PL events over the North Sea by Linders and Saetra (2010) demonstrated that the atmosphere was not conditionally unstable. More importantly, the observed CAPE values were equivalent to the heat flux from the surface and therefore it was unlikely that the CAPE represented any significant part of the energy budget of a PL, integrated over a long period. Instead, Linders and Saetra (2010) suggest that CAPE expresses not a reservoir of energy, but a flux.

An alternative convective theory was proposed by Emanuel (1986) and has continued to be refined (Montgomery et al., 2015). It is known as wind-induced surface heat exchange (WISHE). The essence of the theory consists of the direct feedback between low-level wind speed and speed-dependent surface heat fluxes. Emanuel and Rotunno (1989) applied WISHE for PL development using an axisymmetric model and concluded that this mechanism explains at least some PL events. Another idealised study (Craig and Gray, 1996) found that PL growth is more sensitive to surface drag than to surface heat fluxes, providing evidence in favour of the WISHE mechanism over CISK. It was also supported by a real case study of a PL during the IPY-THORPEX campaign (Føre et al., 2012), and by another case study of a PL in the Barents Sea (Kolstad and Bracegirdle, 2017).

However, this mechanism has some caveats, such as the required assumption of gradient-wind balance and axisymmetry of the vortex (or a closed circulation in the vertical plane). Climatological studies have shown that less than one third of all PLs are identified as symmetric on satellite images (e.g. Blechschmidt, 2008). This calls for further improvements in the theory of convective PLs, possibly by incorporating some of the novel ideas in tropical cyclogenesis, such as rotating convective paradigm, also referred to as 'vortical hot towers' (Montgomery and Smith, 2014).

[1] i.e. when lapse rate of temperature is less than the dry-adiabatic lapse rate but greater than the moist-adiabatic lapse rate

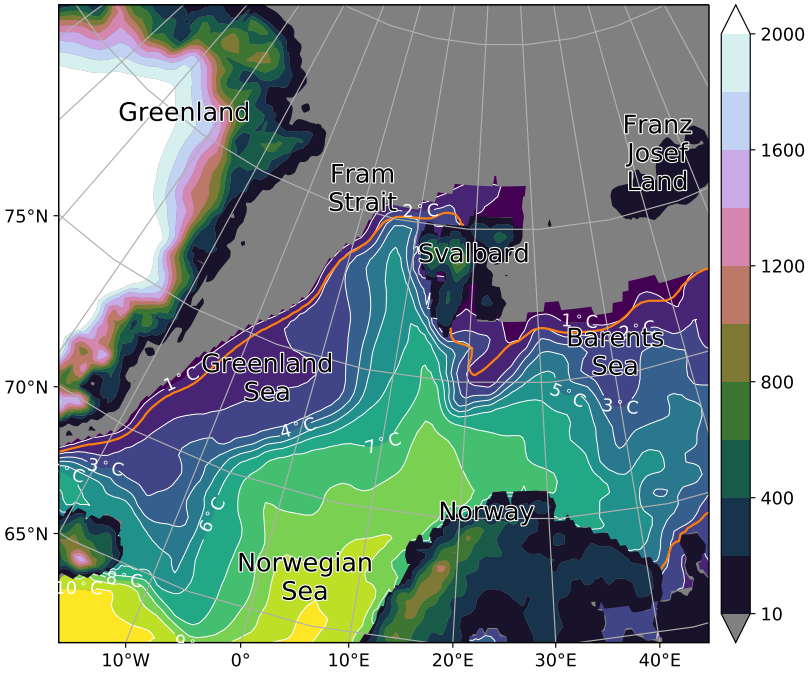

FIGURE 1.5: Sea surface temperature (°C, contours), sea ice boundary (15 %, orange line), sea ice cover(gray area), and surface elevation (m, shading) in ERA5 reanalysis. The mean is taken over October–April 2008–2017.

To some extent the above mechanisms are similar or can even be regarded as 'variations of convective closure rather than being fundamentally different' (Renfrew, 2003). They are also hard to distinguish given the constraints of limited observational data. Moreover, a common requirement for these convective theories is an initial finite-amplitude disturbance that would somehow organise the convection. It is clear though, that the role of convection in PL development is far greater than in mid-latitude synoptic-scale cyclones.

Finally, radiative processes remain as a less explored factor in PL development. Craig (1995) applied an axisymmetric model to show that larger long-wave radiative cooling can lead to higher growth rates in convective PLs. The main mechanism for this enhancement is the increase of the radial temperature gradient between the warm core with latent heat release and the surrounding regions where radiative cooling takes place. However, being short-lived wintertime phenomena, PLs are unlikely to be affected by the diurnal cycle of incoming solar radiation.

1.3 Environments conducive to polar low development

1.3.1 Atmospheric circulation

Certain patterns of the large-scale atmospheric circulation in high latitudes can be conducive to PL activity. In a study by Forbes and Lottes (1985), the location of incipient disturbances relative to synoptic-scale environment was found to be decisive for their evolution into intense PLs. For instance, non-developing cyclones were characterised by unfavourable vorticity advection. Businger (1985) conducted one of the first synoptic-scale composite analyses with regards to PL activity in the North Atlantic. His results were broadly confirmed by Blechschmidt et al. (2009) who found that PLs in the Barents Sea preferentially develop during a strong blocking over Iceland and low pressure over the Barents Sea, while western Nordic PLs preferentially develop during a blocking over Greenland and a surface low over the Norwegian Sea. These findings were also refined by Mallet et al. (2013) and Mallet et al. (2017). They found that PL activity is mostly observed in the Atlantic Ridge regime and in the negative phase of the North Atlantic Oscillation (NAO), see Fig. 1.6. It is important to be cautious when averaging the circulation patterns for different types of PLs. For instance, Terpstra et al. (2016) show that forward-shear PLs (mean wind aligned with thermal wind) are associated with a synoptic-scale ridge over Scandinavia (opposite of AR in Fig. 1.6), while their reverse-shear siblings favour the situation with a trough over that region.

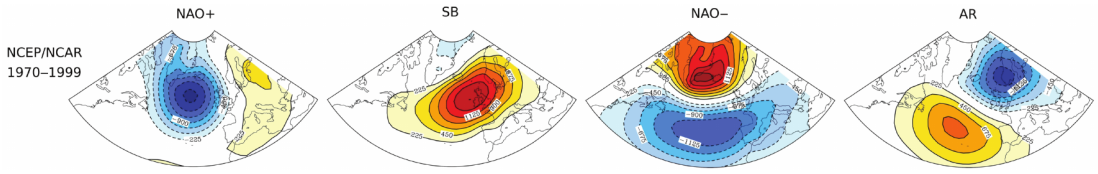

FIGURE 1.6: The four wintertime (November–March) weather regimes over the North Atlantic region from Mallet et al. (2017). The contours show sea level pressure (SLP) daily anomalies (Pa).

The Atlantic ridge and negative NAO weather regimes are generally characterised by a northerly geostrophic flow over the Nordic Seas, which results in the advection of cold air from the Arctic over an ice-free surface of the Atlantic Ocean, i.e. CAOs (Kolstad et al., 2009; Papritz and Spengler, 2017). Consequently, the *modus operandi* of Norwegian forecasters is to look at the temperature difference between sea surface temperature (SST) and the temperature of the middle troposphere (typically at 500 hPa). Kolstad (2011) suggested a refinement of this criterion by combining the marine CAO index (Kolstad and Bracegirdle, 2008) with the pressure at the tropopause level. It is suggested that the reduced tropopause height is imperative to the frequency, whereas the static stability determines the location of PL events.

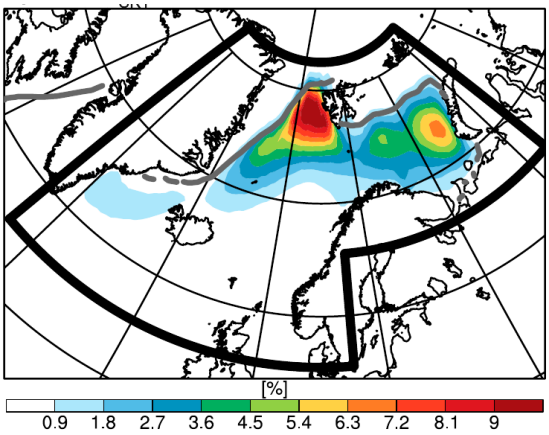

FIGURE 1.7: Mean frequency of the most intense category of CAOs from Papritz and Spengler (2017).

1.3.2 Surface forcing

Geographical features of certain high-latitude regions can make the background environment more favourable for PL development. In the Nordic Seas, these include a number of environmental factors, namely the distribution of ocean currents and sea ice, as well as the location of mountainous islands.

Fig. 1.5 demonstrates a persistent anomaly of SST associated with warm ocean currents off the coast of Norway. The high temperature contrast between the relatively warm ocean surface and cold air coming from the sea-ice covered Arctic can lead to large surface heat fluxes and widespread convection, which can be organised into a PL. The presence of the warm West Spitsbergen Current (Fig. 1.8) results in a concave wedge of open water just west of Svalbard which coincides with the strongest CAOs in the Nordic Seas (Fig. 1.7). This ice-free region is associated with PL genesis and is sometimes referred to as the 'cradle of polar lows' (T. E. Nordeng, personal communication).

The role of sea ice in PL development is twofold. First, the sea-ice edge represents a zone with sharp gradients of temperature, roughness, and albedo, resulting in large differences in the energy budget of the atmospheric boundary layer, especially during winter. Due to the differential heating from the surface, shallow frontal zones are commonly formed, which often lead to the formation of mesoscale vortices and eventually intense PLs (Albright et al., 1995; Heinemann, 1997; Harold et al., 1999b). Second, the difference in momentum fluxes due to surface roughness over the ocean, marginal ice zone (Elvidge et al., 2015a), and the sea ice, can result in barotropic vorticity generation (Rasmussen and Turner, 2003).

In the context of the Nordic Seas, there has been little research focusing on how sea ice affects PLs. In a quasi-idealised study, Dierer and Schluenzen (2005) estimated the interaction between a mesoscale cyclone and different sea ice parameters. They

demonstrated that the surface heat fluxes strongly depended on the sea ice distribution, which is more important than the absolute amount of sea ice in the area. The cyclone development was also highly influenced by its track relative to the ice edge, while the impact of the ice thickness and the ocean currents was negligible. Adakudlu and Barstad (2011) investigated the life cycle of a Barents Sea PL and tested its sensitivity to the distribution of sea ice and SST. A minor weakness of their study is that the model did not reproduce a PL in the control case. They concluded that the removal of sea ice allows the simulated PL to fully develop, while the increased SST leads to a strong vertical coupling between the cyclone and an upper-level PV anomaly. To some extent, the research presented in Chapter 3 continues the work of Adakudlu and Barstad, but concentrates on PLs that develop in a different synoptic situation.

Returning to Fig. 1.5, it can be seen that the northern part of the region is bounded by several orographic obstacles, namely Greenland to the west, Svalbard to the north, Novaya Zemlya to the east, and Scandinavia to the south-east. Although Greenland's orography is not the most common cause for intense PLs (Kristjánsson et al., 2011), forecast failures still occur, with model errors in some cases propagating downstream towards Scandinavia and the British Isles (Kristjánsson et al., 2009). The mentioned studies indicate that model representation of cyclogenesis in the region off east Greenland is sensitive to the orography of the island.

Svalbard has received practically no attention with regards to its role in PL activity. Notwithstanding its rather small size, the flow distortion associated with the archipelago is comparable to that of larger mountains in low latitudes due to typically high static stability (Skeie and Grønås, 2000). The deflection of the northerly or northeasterly flow by Svalbard often produces low-level jets at its flanks (Reeve and Kolstad, 2011), and the shear vorticity associated them can create conditions prone to barotropic cyclogenesis (e.g. Smith, 1989a; Petersen et al., 2003). Whether Svalbard's orography contributes to the formation or maintenance of PLs downstream, is also addressed in Chapter 3.

Even less research has been dedicated to the interaction of PLs with isolated islands and their orography. However, it can be anticipated that with Arctic sea ice retreating northward due to the climate change, archipelagos such as Svalbard will change their role in PL development. According to some of the recent climate modelling studies (e.g Zahn and Storch, 2010; Romero and Emanuel, 2017), the area of PL genesis will shift to the north of Svalbard. Hence, for southward moving PLs originating there, Svalbard will represent a downstream obstacle. This can lead to various flow distortion regimes such as lee intensification through vortex stretching and cyclone splitting (Kristjánsson et al., 2011). Cyclone splitting, for instance, was the focus of Moore and Vachon (2002), in which an unusual case of PL formation over the Labrador Sea was investigated. It developed out of a remnant of a synoptic-scale cyclone that underwent a bifurcation due to interaction with the high topography of southern Greenland. A

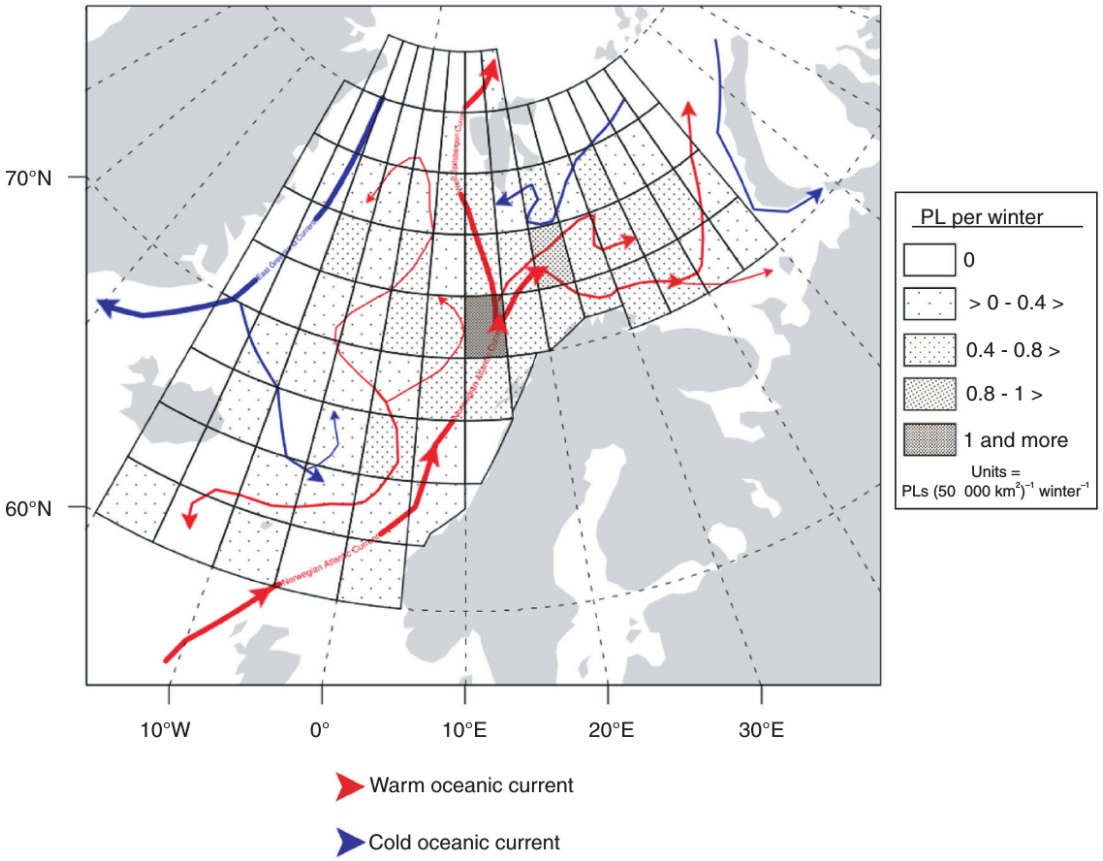

FIGURE 1.8: Area of PL genesis over the Nordic Seas from winter 1999–2000 to winter 2012/2013 (Rojo et al., 2015). Red and blue arrows approximately show the warm and cold ocean currents.

part of the split cyclone moved northward and with the aid of an upper-level PV anomaly grew into a spiral-like PL.

The PLs' kinship with tropical cyclones may be of help due to the fact that tropical cyclone interaction with orography has received more attention. For example, Tang and Chan (2014) and Tang and Chan (2015) provide new insights into the effect of local and remote topographies (Taiwan, Philippines and China terrain) on typhoon tracks. The authors found that tropical cyclone movement is deflected by terrain-induced diabatic heating and secondary gyres, rotating cyclonically around the vortex (Tang and Chan, 2014). In the second part of their study Tang and Chan (2015) extended their investigation to assess the importance of the initial location of a tropical cyclone on the degree of its deflection by Taiwan. Moreover, China's orography appears to shift the tropical cyclone tracks westward due to the advection and diabatic effects.

A lot of mentioned above studies on the role of orography and sea ice in PL evolution permit for a detailed examination of their dynamics and modification of their structure in sensitivity experiments. However, to make broader conclusions about the importance of these factors, a climatological study is required. In the next section, recent climatological studies for the Nordic Seas are briefly reviewed, as a motivation

for Chapter 4.

1.4 Statistical studies of polar lows in the Nordic Seas

Using satellite imagery over a two-year period, Blechschmidt (2008) revealed that the main PL genesis regions lie between Iceland and Finnmark in the Norwegian Sea, in the Barents Sea and in the lee region of Cape Farewell. Blechschmidt reports that Nordic Seas PLs generally occur in winter with a maximum in November or January, but also exhibit high interannual variability.

With the help of forecasters at the Norwegian Meteorological Institute, Noer et al. (2011) developed the Sea Surface Temperature and Altimeter Synergy for Improved Forecasting of Polar Lows (STARS) database, which is the most commonly used record of manually-tracked PLs in the Nordic Seas area. The genesis density was found to be rather evenly distributed over the Norwegian and Barents Seas, following the warm ocean current zones mentioned in Sec. 1.3. A weak local maximum was located close in the eastern Norwegian Sea and is known as 'Tromsø flake'. The authors suggest a link between this 'hot spot' and the convergence of CAOs in the lee of Svalbard. With regards to the seasonal cycle, Noer et al. (2011) confirm the earlier findings of Wilhelmsen (1985) and Bracegirdle and Gray (2008) that there is a minimum of PL activity in February and explain it by the prevalence of a surface anticyclone over the Scandinavian mainland.

The study by Noer et al. (2011) was extended by Rojo et al. (2015), who examined the basic PL characteristics (e.g. lifetime, diameter, vector of propagation, etc). Amongst their new findings was an eastward shift of the PL genesis area throughout the cold season. They also speculated that the formation of two PLs in seemingly unusual locations (one in the Kara Sea and one to the north of Svalbard) could be attributed to a reduction of sea ice cover.

The caveat of most statistical studies mentioned above is that they rely on different definitions of PLs, and their tracks are based on subjective identification from satellite images, which inevitably introduces ambiguity and makes it hard to reproduce the results. Only a handful of studies utilise objective detection methods and reanalyses to compile a present-day climatology of PLs in the Nordic Seas (e.g. Condron et al., 2006; Bracegirdle and Gray, 2008; Zappa et al., 2014; Michel et al., 2018; Stoll et al., 2018). In most of these studies reanalyses' grid spacing was too coarse to resolve the full spectrum of mesoscale cyclones, missing the smaller and weaker ones. Moreover, these studies focused neither on the correlations between PL activity and Arctic sea ice (except for a small section in Michel et al. (2018) and Smirnova et al. (2015)), nor on the climatological role of Svalbard. The third part of this thesis is built on a new climatology and attempts to identify possible links between the Arctic sea ice decline and mesoscale cyclone density over the northeastern North Atlantic.

1.5 Questions addressed in this work

In short, this thesis aims to answer a number of questions.

- What is the mesoscale wind, thermal, and cloud structure of a typical shear-line PL?
- How well does the UK Met Office Unified Model reproduce the evolution and dynamics of PLs?
- To what extent does the presence of Svalbard influence the generation and intensification of mesoscale cyclones in the Nordic Seas?
- How important for PL evolution is the distribution of the sea ice in the area around Svalbard?
- How does the new ERA5 reanalysis compare to its predecessor with respect to objective tracking of PMCs?
- Are the local changes in cyclone tracks related to the Arctic sea ice decline?

1.6 Thesis outline

There is still some controversy in our current understanding of the mechanisms of PMC development, as well as their large-scale patterns. Addressing the questions mentioned above, the structure of the present work is as follows. In chapter 2, a detailed analysis of a shear-line PL at the leading edge of a CAO is presented using comprehensive observations from a well-instrumented aircraft, dropsondes, scatterometer and CloudSat data, and numerical modelling output from a convection-permitting configuration of the UK Met Office Unified Model. This provides a unique insight into the structure of this type of PL and validates the numerical model for subsequent work. In Chapter 3, we investigate the influence of the orography of Svalbard and the sea ice cover in the Norwegian and Barents seas on PL development using a case study approach. In Chapter 4, we expand our study of PLs to a climatological perspective. We use the state-of-the-art ERA5 reanalysis and an objective tracking algorithm to examine spatiotemporal distribution of PLs, as well as the differences between the representation of PLs in ERA5 and in ERA-Interim. Chapter 5 gives a summary of our work and outlines possible directions for future research.

2

Structure of a shear-line polar low

This chapter is based on a paper that has been published in the Quarterly Journal of the Royal Meteorological Society with the same title (Sergeev et al., 2017). The text in the chapter is largely unchanged from the published manuscript. D.E. Sergeev was responsible for the work, under supervision by I.A. Renfrew, T. Spengler, and S. Dorling, who provided scientific input and helped revise the text for publication. The comments of three anonymous reviewers also helped to improve the manuscript.

2.1 Introduction

Myriads of mesoscale vortices emerge over the Norwegian Sea during the extended winter period (Rojo et al., 2015; Kolstad, 2011). The life cycle of each of these vortices is uniquely shaped by its environment and by complex interactions between different physical processes such as baroclinic instability, latent heat release, and surface heat exchange. Under favourable conditions, some of these vortices gain sufficient energy to produce near-surface gale force winds and are referred to as polar lows (PLs) — one of the most extreme weather events of the high latitudes. With their intensity, they are a threat to coastal and maritime socio-economic activities (Hamilton, 2004). The chronic lack of in situ observations at high latitudes makes it challenging to forecast these small-scale and explosive weather phenomena accurately, even for modern numerical weather prediction (NWP) systems (Kristiansen et al., 2011). This shortcoming is especially true at the early stages, when incipient perturbation PLs can be embedded in convergence zones with large horizontal wind shear. We present the evolution of

such a shear-line PL using comprehensive observations obtained during the Aerosol-Cloud Coupling And Climate Interactions in the Arctic (ACCACIA) field campaign, in conjunction with satellite data and high-resolution model simulations performed with the UK Met Office's Unified Model (MetUM) — their operational NWP model.

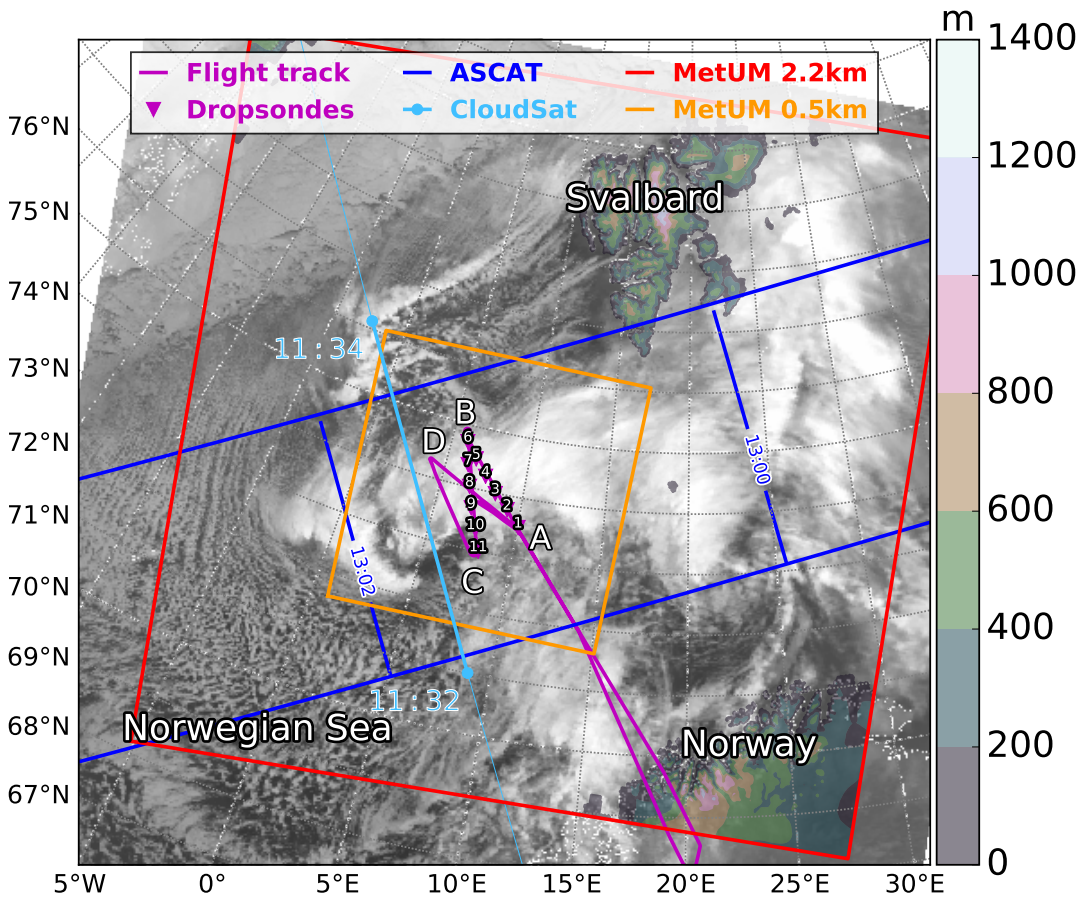

FIGURE 2.1: Observational and modelling domains. Cloud cover is shown as Advanced Very High Resolution Radiometer (AVHRR) channel 4 image (1220 UTC 26 March 2013). The modelling domains with 2.2 km and 0.5 km grid spacing are marked by the red and orange boxes, respectively. The flight track (1016–1405 UTC) is shown by the purple line and dropsonde locations are marked as numbered triangles. The CloudSat (cyan) and Advanced Scatterometer (ASCAT) (blue) swaths are also overlaid. Model topography is shaded (m).

Several modelling studies have been focused on the dynamics of PLs over the Nordic Seas, for example, Adakudlu and Barstad (2011), Nordeng and Røsting (2011), and Claud et al. (2004). To improve our theoretical concepts and to verify numerical models, it is necessary to gather detailed information about the anatomy and life cycles of archetypal PLs, ideally with high-quality airborne observations. However, aircraft field campaigns are expensive, with the additional impediment that it is difficult to have the aircraft in the right place at the right time to obtain the most useful observations. Consequently, less than a dozen PLs have been investigated by research aircraft.

The classic case study by Shapiro et al. (1987) of a Norwegian Sea PL provides a vivid picture of a meso-α-scale vortex with well-defined mesoscale fronts and strong winds. Using data from an extensive range of observations, they conclude this PL was induced by a propagating upper-level trough and intensified due to baroclinic instability and convection. The wind speeds exceeded 30 m s^{-1} and were observed below 2 km at a radius of 100 km, with relative vorticity above 2×10^{-3} s^{-1}, representing the 'truly mesoscale' nature of the PL. Subsequent studies report similar PL structures with diameters typically in the range 300–700 km and maximum wind speeds usually above 20–25 m s^{-1} (e.g. Douglas et al., 1995; Brümmer et al., 2009; Føre et al., 2011). Estimated latent and sensible heat fluxes range between 200–500 W m^{-2} with the Bowen Ratio close to unity.

Modern aircraft observations of PLs can be substantially complemented by airborne lidar. For example, Wagner et al. (2011) used two lidars, including a Doppler wind lidar, to provide high-resolution cross-sections of water-vapour mixing ratio, backscatter ratio, and horizontal wind speeds through the inner part of a PL. These observations provide a very thorough description of a PL 'eye' and were essential to compare against the authors' axisymmetric and NWP models.

In the absence of in situ observations, satellites provide a sweeping source of observational data for PL detection and analysis, for instance through cloud imagery from the Advanced Very High Resolution Radiometer (AVHRR) (Harold et al., 1999a). Ocean wind vectors from scatterometers are among the spaceborne data assimilated by forecasting centres (Chelton et al., 2006). A few case studies also pinpoint the benefits of using synthetic aperture radar (SAR) images to examine the finescale (resolution of 100–200 m) features of near-surface winds within PLs (Moore and Vachon, 2002; Furevik et al., 2015). A new powerful tool to study the internal properties of PL clouds has become available with the launch of NASA's CloudSat in 2006. CloudSat measures radar reflectivity versus altitude in a nadir slice along the satellite track. Unlike hurricanes (Tourville et al., 2015) and mid-latitude cyclones (Field et al., 2011), to the authors' knowledge there are no detailed PL investigations based on CloudSat data except for a short note by Forsythe and Haynes (2015), who briefly illustrate CloudSat's intersection of a PL that developed over the Labrador Sea in November 2013.

There were multiple PL events around the Svalbard Archipelago during the ACCACIA intensive observational period in March–April 2013, and one of the most intense was investigated by the research aircraft on 26 March. The objective of this study is to scrutinise the structure of this PL, which developed along a shear line south of Svalbard. We focus specifically on the mesoscale features of the wind and temperature fields and especially on the cloud properties of the PL, assessing the liquid water and ice concentration at different levels. We use a wealth of observations, including direct measurements and dropsondes from the research aircraft; CloudSat radar data

and MetOp-A's scatterometer products. In addition, the MetUM is run at convection-permitting 2.2 km grid spacing, in order to to deepen our analysis of the PL and validate this state-of-the-art operational model against the aforementioned observations. The choice of this PL is dictated by the uniqueness of the successful aircraft observations and their coincidence with appropriate satellite overpasses.

Sections 2.2 and 2.3 describe the observational data and the model set-up respectively. Section 2.4 presents the large-scale synoptic conditions before and during the PL development. Section 2.5 discusses the evolution of the PL and section 2.6 describes the mesoscale structure of the PL, while both evaluate the performance of the model. Section 2.7 synthesises and concludes this study.

2.2 Observational data

2.2.1 Direct observations

Our domain of interest is shown in Fig. 2.1. Data were gathered by the Facility for Airborne Atmospheric Measurements (FAAM) BAe-146 aircraft during flight B763 on 26 March 2013. The on-board instruments provided standard meteorological variables, including the three components of wind velocity, pressure, temperature, and humidity (see e.g. Renfrew et al., 2008). Cloud droplet and ice crystal concentrations were sampled by the Cloud Droplet Probe (CDP) and the Two-Dimensional Stereoscopic Probe (2D-S) respectively; both optical scattering probes. The particles were categorised by size and shape, and their number densities were converted to liquid (LWC) and ice water content (IWC). In addition, estimates of liquid water content (LWC) and total (ice plus liquid) water content (TWC) were provided by the hot-wire deep cone Nevzorov probe (Korolev et al., 1998). For convenience, all aircraft measurements are shown at 1 Hz resolution, which corresponds to a resolution of ≈100 m in the horizontal.

In addition, eleven GPS dropsondes (Vaisala RD93) were released sequentially every ≈5 min to obtain the vertical structure of the atmosphere. With typical terminal velocities of about 10 m s^{-1} (Petersen et al., 2009), they provide vertical profiles of wind speed and direction, pressure, temperature, and humidity.

The B763 flight took place in the northern part of the Norwegian Sea, approximately within the area of 73°–75°N, 4°–10°E with the flight track following a 'butterfly' pattern (A-B-C-D-A). The period of measurements lasted from 1100 to 1400 UTC. Two legs (A-B, B-C) were made at an altitude of ≈6000 m above sea level (ASL) when the dropsondes were released and their data sent to the Global Telecommunication System (GTS). The descent from C to D gave information about clouds on the northern side of the PL. The low-level quasi-horizontal run from D to A (with partial legs from A back towards D) was mainly at 35 m ASL to allow estimates of surface layer characteristics. However, due to low visibility the aircraft ascended to 300 m ASL for 15 min. The mission finished with an ascending profile, in calm conditions close to

point A. Overall, the flight was successful as both sides of the shear line were probed with profiles and legs at several altitudes.

2.2.2 Satellite data

Satellite remote-sensing instruments provide estimates of cloud composition, surface winds, and radiative fluxes.

Near-surface wind speed was obtained by the ASCAT installed on the polar-orbiting MetOp-A satellite. The dataset used in this study has 12.5 km resolution and covers the ocean surface in two 550-km-wide swaths. The applicability of ASCAT data to PL studies is discussed by Zabolotskikh et al. (2013) and Furevik et al. (2015). Although the satellite orbit goes through the same high-latitude region several times a day, only a few of the overpasses fully captured the observed shear-line. We will focus on the 1300 UTC overpass.

Another satellite product comprises snapshots of top-of-atmosphere outgoing long-wave radiation (TOA OLR) retrieved by NOAA's AVHRR instrument. Observations are made in the thermal infra-red channel (10.3–11.3 µm) with 1.09 km spatial resolution and give an excellent overview of the cloud features associated with the cold air outbreak (CAO) (see Fig. 2.1).

Until recently, the vertical structure of high-latitude marine weather phenomena could only be sampled by direct airborne observations or, rarely, by a research vessel's radar (e.g. Shapiro et al., 1987). With the advent of CloudSat, carrying a highly sensitive 94 Hz cloud profiling radar, it has become possible to dissect and study the internal structure of such phenomena more comprehensively. Being a polar-orbiting satellite with sun-synchronous orbit, CloudSat provides a good coverage of high latitude regions. It repeats the same ground track every 16 days, meaning that the Norwegian Sea, for example, is probed on average 4 times per day. Fortunately, the CloudSat orbit passed exactly over the area of interest within the period of aircraft observations (around 1130 UTC), allowing us to complement the observational dataset with radar reflectivity and other derived quantities sampled at 240 m vertical resolution and with 1.4×1.7 km footprint size. The reflectivity is measured within -30 to 40 dBZ range (Tourville et al., 2015).

2.3 Numerical model

We use one of the latest versions (`vn10.2`) of the UK Met Office's Unified Model (MetUM) in atmosphere-only mode for this study. The model has been used several times in previous PL studies (e.g. Irvine et al., 2011; Bracegirdle and Gray, 2009). The basic equations of the model are described in Davies et al. (2005) and essentially represent the atmosphere as a deep non-hydrostatic fully compressible fluid. The equations are discretised on an Arakawa C-grid in the horizontal and a Charney-Phillips grid in the

vertical. Recently, significant improvements to the numerical schemes have been implemented in the model's dynamical core, now referred to as 'ENDGame' (Wood et al., 2014). Changes to the model's physics, amongst many, included a new orographic drag scheme, a corrected convection entrainment scheme, and revised turbulent mixing for stable, unstable, and shear-dominated boundary layers, which improves the representation of clouds in polar CAOs (Brown et al., 2008).

TABLE 2.1: MetUM set-up.

Category	Specification
Version; nesting suite id	`10.2`; `u-aa753`
Dynamical core	Fully compressible non-hydrostatic Navier-Stokes equations
Advection scheme	Semi-implicit, semi-Lagrangian predictor-corrector scheme
Turbulence closure	• Unstable conditions: non-local closure with entrainment fluxes • Stable conditions: SHARPEST scheme
Microphysics	Single-moment 3-phase
Convection	Explicit
Cartographic projection	rotated pole
Horizontal grid spacing	2.2 km
Horizontal domain	1300 km $\times$ 1300 km
Rim width (grid points)	24
Vertical grid	70 levels, including 16 levels below 1 km
Time step	60 s
Output frequency	1 h

The MetUM cloud microphysics scheme is a single-moment three-phase representation based on Wilson and Ballard (1999), with the use of multiple sub-time stepping and extensive modifications (e.g., the particle size distribution is described in Abel and Boutle, 2012). The parametrisation uses prognostic cloud water and rain mixing ratios for the liquid phase. For ice there is a prognostic variable that represents all ice in the grid box. Production or loss of cloud water, ice and rain is governed by such processes as condensation, evaporation, autoconversion, accretion, droplet settling, freezing of droplets by ice nucleation, diffusional growth, and riming. The maximum ice nucleation temperature was set to -10°C. For the large-scale cloud, the Smith scheme was used, which depends on the diagnostic cloud fraction and condensate variables, based on a symmetric triangular PDF of subgrid variability.

The model calculates surface fluxes separately on each tile using the similarity theory. For the boundary layer, the scheme described by Brown et al. (2008) is used. Although the sensitivity of PLs to the sub-grid mixing parameterization is beyond the scope of this chapter, the MetUM schemes used in the present study have been tested

in PL cases by e.g. Irvine et al. (2011) and McInnes et al. (2011), who have shown that the boundary layer and surface fluxes paramerizations are suitable for reproducing these events. Table 2.1 shows key model specifications. More details of the MetUM can be found in Walters et al. (2017) and references therein.

A global MetUM simulation with N768 resolution (17 km) was initialised using the operational analysis and generated boundary conditions for a nested model (Nesting Suite version `u-aa753`). The horizontal grid spacing of the limited area model was ≈2.2 km, while the time step was 60 s. The domain was centred at 74°N, 15°E to capture the movement of the shear line and the emerging PL, as well as the northerly CAO flowing around the Svalbard archipelago (Fig. 2.1).

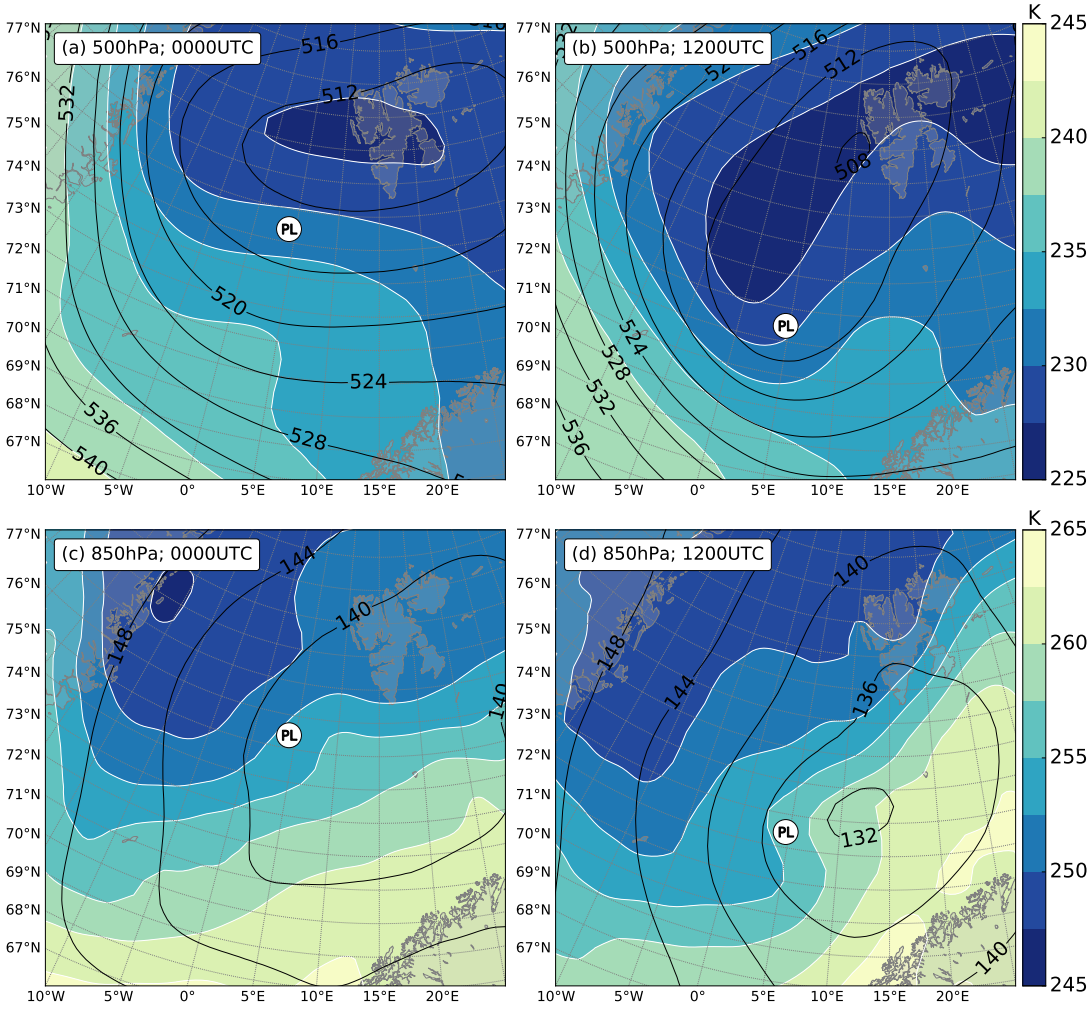

FIGURE 2.2: ERA-Interim air temperature (colour shading, K) and geopotential height (cyan contours, 10 m) at 500 hPa (a, b) and 850 hPa (c, d) for 0000 UTC (left column) and 1200 UTC (right column) 26 March 2013. The location of the PL (from subjective satellite analysis) is marked.

We tested the impact of the initialisation time, starting the simulations at 0600 UTC,

1200 UTC, 1800 UTC 25 March, and 0000 UTC 26 March. The majority of the analysis focuses on the midday conditions on 26 March. An additional experiment was performed with even smaller horizontal grid size (0.5 km) for the central part of the coarse-resolution domain (orange box in Fig. 2.1).

The model output frequency was set to 10 minutes during the aircraft observations period and to one hour for the remaining time. All variables were interpolated to the middle points of grid boxes, to avoid problems with data analysis on the staggered grid. We use the Python packages `iris` (Met Office, 2016) and `matplotlib` (Hunter, 2007) for analysis and visualisation. All the code used in this study is publicly available on GitHub[1].

2.4 Synoptic overview

To understand the background state of the atmosphere prior to and during the PL event, we examined the 6-hourly European Centre for Medium-Range Weather Forecasts (ECMWF) ERA-Interim reanalysis. Although there are notable constraints on how accurately PLs are represented in this dataset (Zappa et al., 2014; Laffineur et al., 2014), its purpose here is to give a general picture of the large-scale circulation over the North Atlantic. At the end of March 2013, polar maritime air masses over the western part of the Norwegian Sea were swept away by colder Arctic air during an intense CAO. An upper-level ridge shifted south-westwards, and the study area began to be dominated by a cold trough, which stretched from the eastern Barents Sea with core temperatures below -45°C (Fig. 2.2a). By the time of the PL event the temperature at 500 hPa had lowered by $\approx$8 K over the Norwegian Sea. Upper-level forcing appears important due to a large potential vorticity (PV) anomaly on the 285 K isentropic surface (Fig. 2.3). The PV maximum reached values of 4–4.5 PVU and was located to the north (upstream) of the developing PL.

The 850 hPa thermal field reveals an intensification of the baroclinic zone, as shown in Fig. 2.2c, d. Shaped by the CAO to the west and warm sector advection to the east, it spreads all the way from Iceland to the eastern coast of Svalbard, and its orientation slowly became more meridional. The northern part of the baroclinic zone was characterised by a vertical velocity dipole with maximum amplitude at the height of 700 hPa, about 5° to the east of of the observed PL position (not shown).

In the lower troposphere, a stationary large-scale depression prevails over the area of interest, as shown by 850 hPa geopotential height (Fig. 2.2d) and also evident in the SLP simulated by the MetUM (Fig. 2.4a,c,e). The synoptic depression slowly deepens, and the cloud bands of several mesoscale vortices can be clearly distinguished on its periphery, including the one that was probed by the aircraft (Fig. 2.1, 2.4e). Originating

[1] https://github.com/dennissergeev/structure-of-a-shear-line-polar-low-notebooks

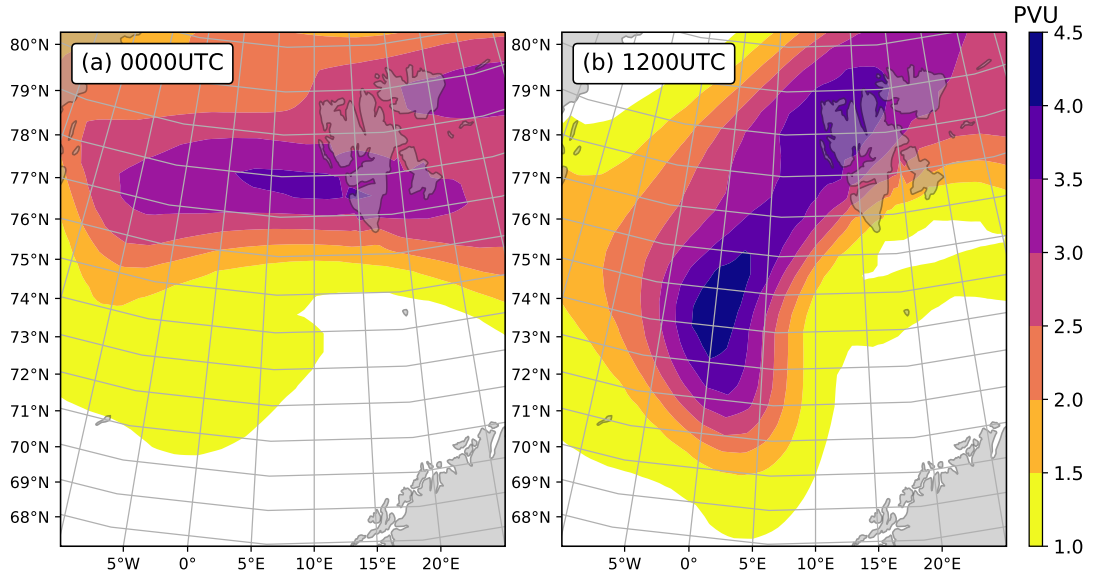

FIGURE 2.3: ERA-Interim isentropic PV (colour shading, PVU) at 285 K for (a) 0000 UTC and (b) 1200 UTC 26 March 2013.

in the CAO in the rear part of the synoptic low, the vortices are steered by the cyclonic flow and form a typical 'merry-go-round' pattern (Forbes and Lottes, 1985).

The CAO appears in the cloud imagery as an area of shallow cellular convection, which again indicates significant surface-atmosphere temperature contrasts. In fact, the so-called marine cold-air outbreak (MCAO) index, which is proportional to the potential temperature difference between surface skin temperature and 700 hPa height (Bracegirdle and Kolstad, 2010), on 26 March was at its highest for the ACCACIA campaign period, implying that the observed PL developed during the strong advection of an Arctic air mass over the relatively warm ocean surface. These conditions often result in PL propagation being opposite to the thermal wind, i.e. reverse shear conditions (Terpstra et al., 2016).

Given the outlined synoptic conditions, it is not surprising that PLs developed. The observed PL of interest started to grow on a convergence line (a trough in the SLP field, Fig. 2.4a) in the lee of Svalbard. The convergence line, discernible in the relative vorticity field (Fig. 2.4b,d,f) at the leading edge of the trough, folds into the PL of interest and spawns chains of mesoscale waves along the NW and NE shear lines (see Sec. 2.5.2). In the satellite image at 1220 UTC (Fig. 2.1), when the PL is centred at 73°N, 5°E, it can be pinpointed as a beak-like signature of bright (and hence, deep convective) cloud bands. The large-scale circulation during the PL event is common in this region: for example, the PL of 3–4 March 2008 developed in a similar background (Kristjánsson et al., 2011).

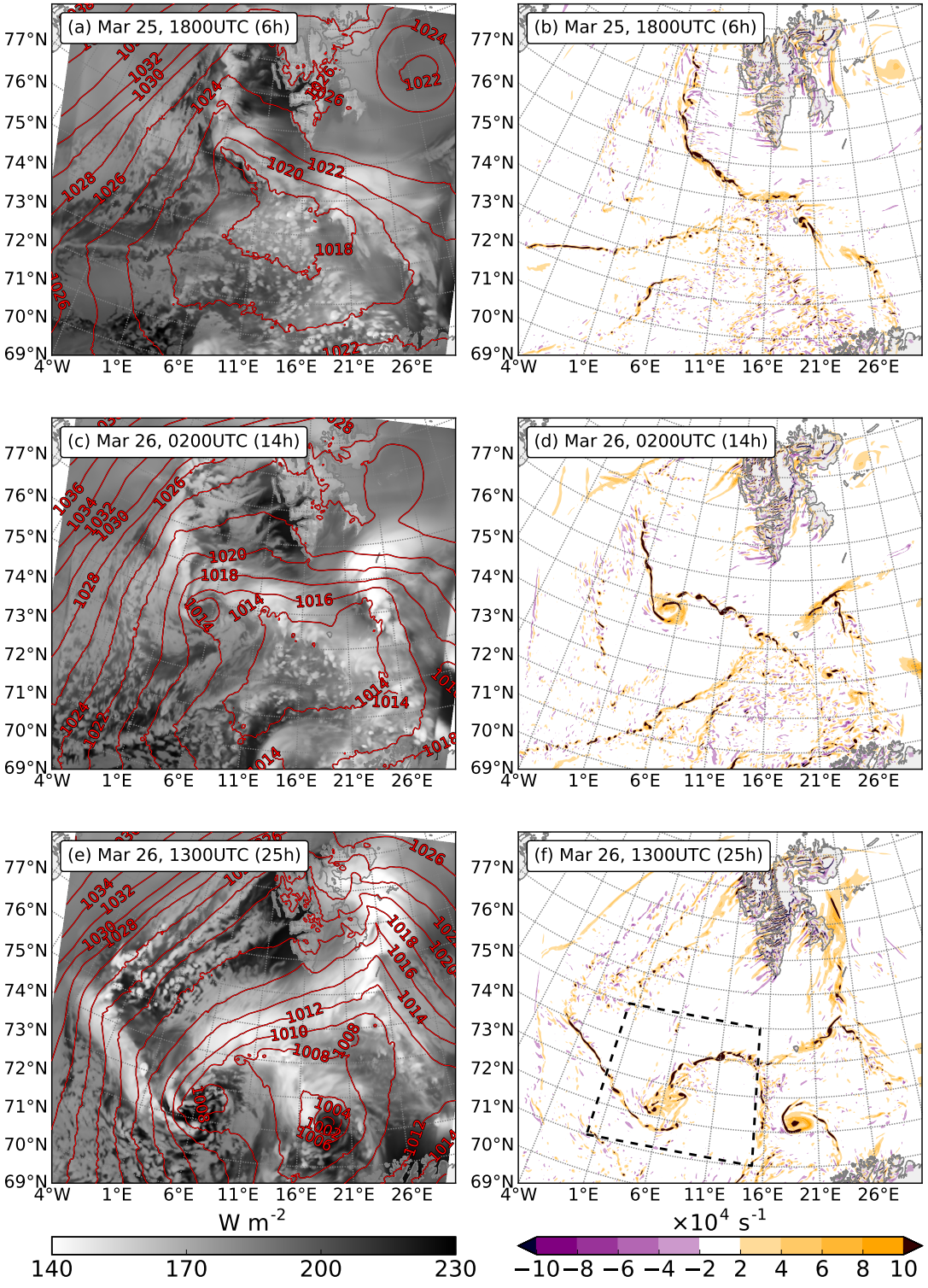

FIGURE 2.4: Temporal evolution of the PL shown by (a,c,e) simulated TOA outgoing longwave radiation (OLR) ($W\,m^{-2}$) with overlaid sea level pressure (SLP) (red contours, hPa) and (b,d,f) relative vorticity ($10^{-4}\,s^{-1}$) at 950 hPa. (a,b) 25 March 1800 UTC, (c,d) 26 March 0200 UTC (e,f) 26 March 1300 UTC. The dashed box displays the close-up area shown in Fig. 2.5 and 2.9.

2.5 Polar low simulation

Several model experiments have been conducted before analysing the weather phenomenon in detail. The set of experiments with 2.2 km grid spacing simulates the flow evolution skilfully, even with the default parameterization settings, usually applied for operational NWP over the British Isles. We carry out the MetUM validation primarily for wind velocity (u and v components), air temperature (T), air pressure (p), specific humidity, LWC and IWC, as well as sea surface temperature (SST), and surface sensible (SHF) and latent (LHF) heat fluxes.

2.5.1 Sensitivity to grid spacing and initialisation time

For the first time, a PL is simulated using a horizontal grid size of 0.5 km. The corresponding domain 500×500 km in size is nested in the 2.2 km domain (Fig. 2.1). Despite a finer representation of discrete convective cells, a qualitative comparison of wind speed and surface pressure revealed that this reduction in grid spacing does not give a remarkable improvement in model performance. This finding agrees with McInnes et al. (2011) for the same numerical model, who found that going from 12 km to 4 km in horizontal spacing lead to considerably better results, while going further to 1 km was less fruitful.

Forecasting such rapidly evolving PLs is known to be sensitive to the numerical model's initialisation time (Irvine et al., 2011). Comparing the satellite data with the modelled total cloud amount we noticed that the model reproduces the cloud patterns accurately both when initialised at 0000 UTC 26 March or 12 hours earlier (not shown). On the other hand, the cloud bands surrounding the PL eye in the forecast from 0000 UTC mismatch reality as observed by AVHRR and the 1200 UTC 25 March simulation, e.g. the cloud-free gap between the two main cloud bands is missing in the 0000 UTC forecast (See Fig. 2.1, 2.4e). In terms of SLP, the PL minimum is slightly deeper in the later forecast (0000 UTC), leading to a stronger pressure gradient and higher than observed wind speeds. In longer lead-time simulations, the model skill deteriorates significantly, e.g. in the experiment starting at 0600 UTC 25 March, the wind maximum has a different shape and is located quite far from the observed shear line (not shown).

The initialisation time experiments expose a degree of sensitivity in the location and shape of the shear line. The simulation initialised at 1200 UTC 25 March best matches the observations, particularly of low-level winds. This lead time (≈24 h) is probably not significant, as the size of the limited area domain was a factor, as well as the atmospheric state at initialisation time.

To sum up, the forecast run starting at 1200 UTC 25 March is chosen as the control experiment, as it qualitatively resembled the observations best, and is thus used for the further analysis of the internal structure of the PL.

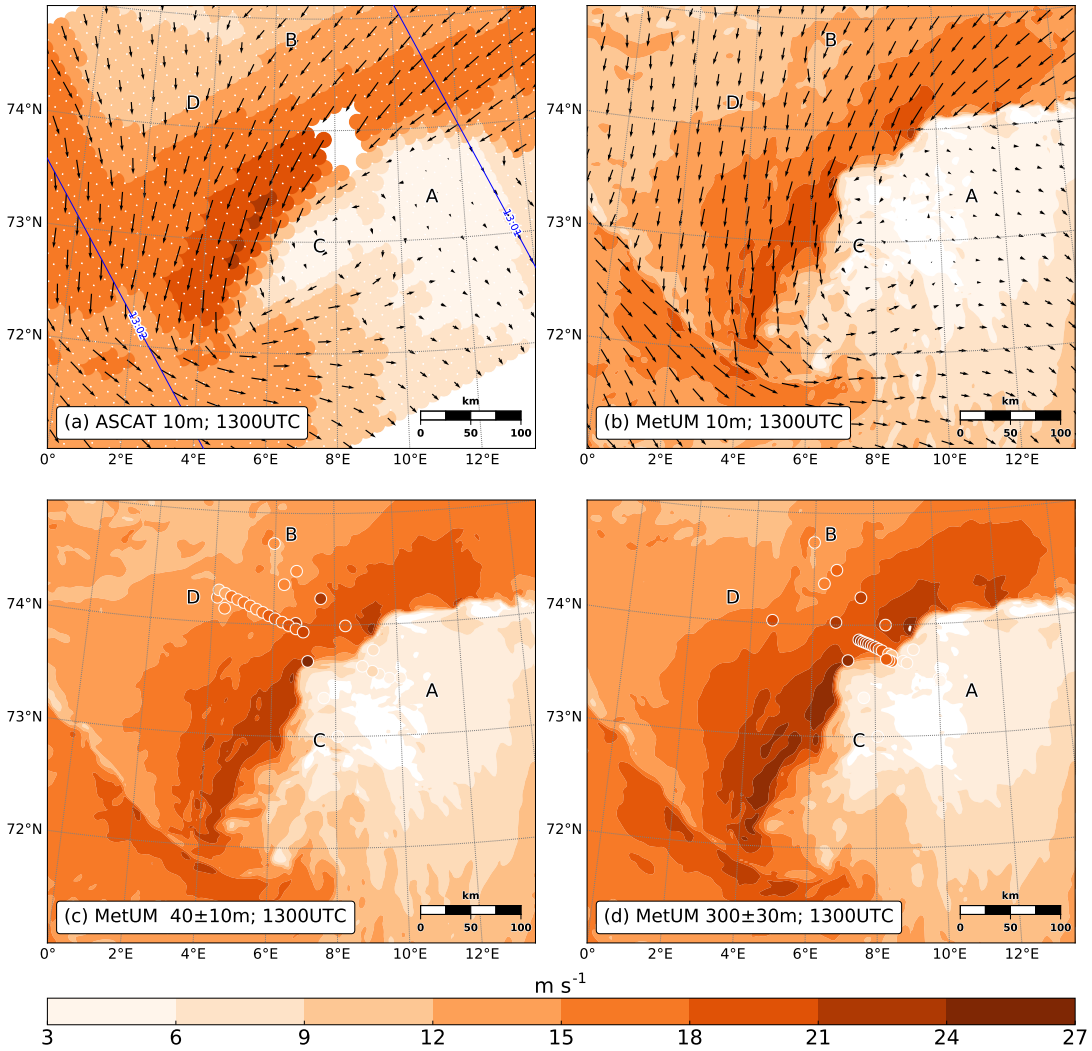

FIGURE 2.5: Surface wind magnitude and direction (a) estimated by ASCAT and (b) simulated by MetUM. Wind speed from the model (colour shading, $\mathrm{m\,s^{-1}}$) and airborne observations (coloured circles, $\mathrm{m\,s^{-1}}$) at 1300 UTC (25 h of the simulation) sampled and vertically averaged over: (c) 40 ± 10 m, (d) 300 ± 30 m.

2.5.2 Life cycle of the polar low

The results of high-resolution numerical experiments in conjunction with satellite imagery provide the opportunity to scrutinise the PL development in great detail. On 25 March, the NE flow of the CAO from the Barents Sea converged with the main branch of the northerly flow, forming a high relative vorticity banner with maxima of order $10^{-3}\,\mathrm{s^{-1}}$ (Fig. 2.4b). The banner was oriented from N to SE and had a silhouette resembling the Svalbard coastline, while almost the whole area of the Norwegian Sea was speckled with smaller vortical disturbances. Starting from 1800 UTC (forecast time 6 h), the positive vorticity band began to bend and undulate, generating mesoscale shear-instability waves. The most unstable of these developed into a quasi-axisymmetric cyclonic disturbance at 0200 UTC 26 March, at the forecast time of 14 h

(Fig. 2.4d). The vorticity band continued to roll up, and smaller waves merged into the dominant mesocyclone, increasing its radius and pressure deficit.

In the morning of 26 March, even though the associated cloud structures do not stand out in the satellite imagery, they are discernible in the simulated top-of-atmosphere OLR field, as well as in the surface pressure field (Fig. 2.4c). Over the next 14 hours the mesocyclone steadily deepened, dominating the vorticity field and maintaining a cloud-free core (Fig. 2.4e,f). At midday, the PL centre is clearly seen as an SLP minimum (closed 1008 hPa-isobar) and as a dark patch in the OLR field. The main cloud bands have relatively low OLR ($\approx$140 W m^{-2}), highlighting deep convection, and concur with the high-vorticity banners. Further to the SE, another band of shallow convection is located (grey colours in the satellite imagery). The simulated OLR generally corresponds very well with the AVHRR image (compare 2.4e to Fig. 2.1), as does the simulated surface wind and scatterometer data (see Sec. 2.6.1).

At this time (midday, 24 h of the simulation), another mesoscale cyclone develops on a similarly folding vorticity banner a few hundreds of kilometres from the continental coast (Fig. 2.4f) and becomes deeper in SLP than the observed PL (Fig. 2.4e) The new vortex moves northward, creating a large spiral cloud band and developing a much deeper trough within its core. Meanwhile, the observed PL continues to travel south-eastward following the large-scale cyclonic flow. The PL grows in diameter, deepens to $\approx$1000 hPa and forms a more spiraliform cloud signature, but soon starts to disintegrate into smaller disturbances that are visible both in the real and simulated cloud imagery (not shown). These disturbances fill the inner region of the PL, which can no longer be identified by a clear eye. Eventually the PL ceases to exist as a separate vortex and its remnants are absorbed into the new, stronger cyclone.

2.6 Mesoscale structures

The morphology of the shear-line PL is investigated via a combined analysis of aircraft flight-level observations, dropsonde profiles, ASCAT wind estimates, radar measurements from the CloudSat and model results. The analysis here is confined to 1100-1400 UTC 26 March 2013. Note the PL translation velocity was about 10 m s^{-1} from the NW at this time, subjectively determined from AVHRR imagery.

2.6.1 Horizontal structure

In the lower troposphere, the horizontal wind reaches values of almost 25 m s^{-1} within the NE shear line (Fig. 2.5). The second shear line with wind speeds up to 10 m s^{-1} is related to NW flow and separated from the former shear line by a thin trail corresponding to the cloudless gap. The scatterometer data generally confirm the model results, but the gradients are weaker compared to the model and not all the shear-line waves are well captured, most likely due to the relatively coarse spatial resolution

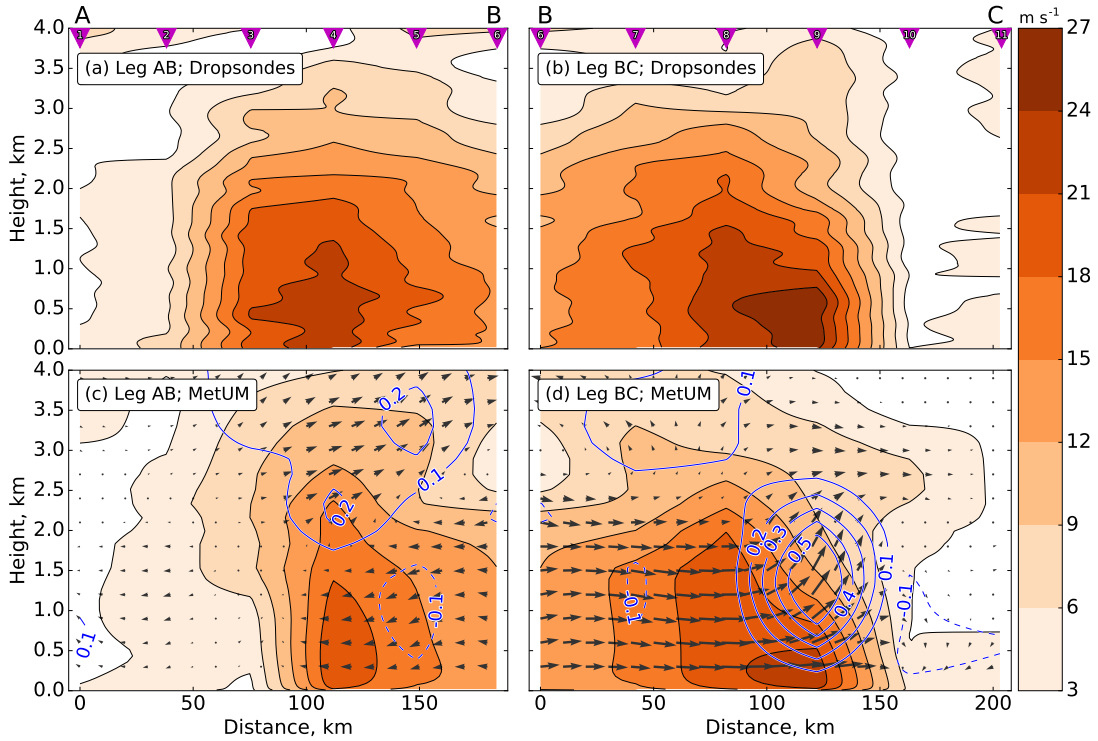

FIGURE 2.6: Vertical cross-sections of wind speed (colour shading, m s^{-1}) along the two flight legs across the shear line based on interpolated dropsonde soundings (top) and model output (bottom). The simulated vertical velocity (blue contours, m s^{-1}) and tangential wind speed (black vectors) are overlaid on the bottom panels. Numbered triangles mark sounding locations. The dropsonde data (top) were smoothed using a 25-second 6-order Butterworth filter.

(12.5 km). The NW shear line and the convergence zone are less sharp in ASCAT data. Quantitatively, one can see the scatterometer's estimate is larger by 2–3 m s^{-1}, especially closer to the PL centre (Renfrew et al., 2009a). Finally, scatterometer retrievals do not provide a well-defined circulation centre in that region.

The horizontal wind structure is very similar at 300 m ASL, but the magnitude is several m s^{-1} higher than at 40 or 10 m (cf. Fig. 2.5b,c,d). The PL core appears as an area of calm wind conditions, surrounded by shear lines. At this time its diameter is 100–150 km, so it can be classified as a meso-β-scale cyclone. In fact, the core of the PL consists of several small and weak vortices rotating around the main circulation axis (Fig. 2.4f). Animations of the wind field suggest that shear instability waves feed the growing PL, while the vorticity source is concentrated upstream within the NE shear line. The shear line is comprised of typically 5–6 meso-γ-scale undulations with wavelengths ranging from 20 to 100 km. With velocity exceeding 27 m s^{-1}, horizontal gradients are sharper across the shear line than within the PL core.

One of the most active 'wavy' parts of the NE shear line was the area of our airborne observations, which are illustrated in Fig. 2.5c,d by scattered circles. Note that the markers show not only the aircraft data sampled within the 40 ± 10 m and 300 ± 30 m layer, but also the vertically averaged dropsonde measurements, though

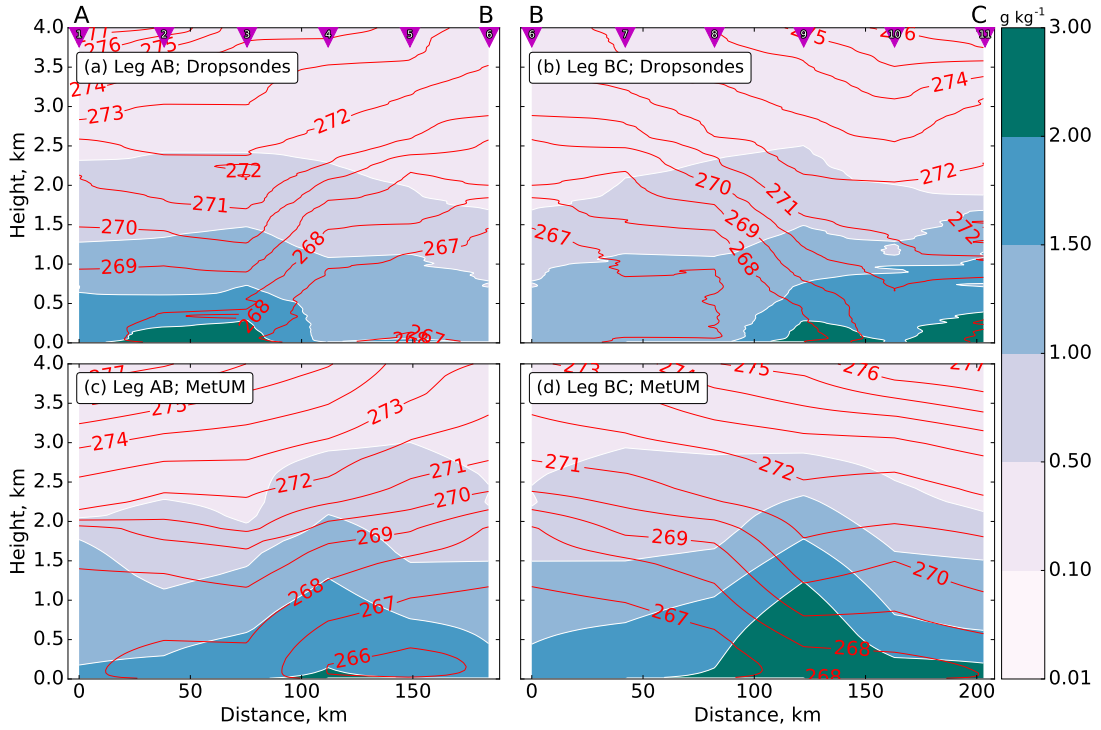

FIGURE 2.7: Vertical cross-sections of water vapour mixing ratio (log-scaled colour shading, g kg^{-1}) and potential temperature (red contours, K), as in Fig. 2.6.

these are from 1.5 h earlier. Both levels demonstrate an excellent match between the numerical simulation and the observations in terms of the location, shape, and amplitude of shear instability waves.

2.6.2 Vertical structure

The shear line was penetrated several times during the research flight. The first two times occurred during high-altitude aircraft legs when the dropsondes were released (Fig. 2.1), providing snapshots of the atmosphere below. As shown in Fig. 2.6, the vertical cross-sections along the two flight legs, from SE to NW (A-B, left panel) and back to the SSE (B-C, right panel), present the shear line as a zone with a very sharp wind speed gradient with a typical width of about 50 km, where the wind speed changes by more than 25 m s^{-1}, yielding a horizontal shear of 0.5×10^{-3} s^{-1}. The low-level jet is located to the NW of the shear zone and was captured by the dropsondes 4 and 9. The jet core is encircled by the 24 m s^{-1} contour and is confined to the lowest 1000 m, while the horizontal shear remains large up to about 3000 m. Northward of the jet the shear is not as strong, defining the forefront of the CAO with steadily intense northerly flow. The overall correspondence between the observed and simulated winds is quite good. The simulated jet, however, is slightly misplaced and more vertically constrained, while its magnitude is also lower by several m s^{-1}.

The shear line is evidently sharper along the B-C leg (Fig. 2.6b,d), which traverses a crest of one of the instability waves (Fig. 2.5d). Here, the low-level jet concurs with convection represented by high upward velocities in the model cross-section panels. Convective updraughts reach $0.55\,\mathrm{m\,s^{-1}}$ and are concentrated precisely above the jet core, with a peak at 1500 m. The calm region to the south of the shear line has continuous downward motions with a minimum of $< -0.10\,\mathrm{m\,s^{-1}}$ (along the B-C cross-section).

Two different boundary layers can be identified in the cross-sections of potential temperature and water vapour mixing ratio (Fig. 2.7). The marine boundary layer of the warm air mass appears weakly stable and contains more moisture. Due to the high humidity, the vertical gradient of the equivalent potential temperature (θ_e, not shown) reveals that the boundary layer is conditionally neutral to ≈1500 m, while below 100–200 m there is a conditionally unstable surface layer. In the colder and drier Arctic air mass, on the other hand, a neutrally stratified boundary layer develops to ≈1000 m, capped by enhanced stratification above. The isentropic surfaces slant at a relatively small angle with respect to the surface, forming a thermal front with a θ gradient of 3 K per 50 km in the lower 500–1000 m that appears to be in balance with the wind shear.

The MetUM skilfully reproduces the temperature field, with the exception of the very edge of the CAO where the slope of isentropes is smoothed too much. In addition, the model makes the warm air too stable and colder than the in situ measurements show. In terms of atmospheric moisture, the model amplifies the boundary layer water vapour maximum at the shear line, which is linked with the strong latent heat flux (LHF) (next section) and coincident with high vertical velocity (Fig. 2.6d) associated with strong convection. Quantitatively, our results are similar to those obtained for similar PL cases (Shapiro et al., 1987; Brümmer et al., 2009; Wagner et al., 2011) where in the cloud bands near the PL core the water vapour mixing ratio is usually observed to be of the order of 2–3 $\mathrm{g\,kg^{-1}}$. The θ_e field is also simulated very close to the observations, though at the shear line due to the overly humid air, the θ_e maximum is larger than in the dropsonde data.

2.6.3 Surface layer characteristics

The high-frequency data collected during the low-level flight legs (D–A) at ≈35 m ASL allow us to study the shear zone boundary layer in great detail. The first part of the flight leg (1240–1258 UTC) took place within the CAO, where the steady NNW wind rose from 15 to $26\,\mathrm{m\,s^{-1}}$ towards the jet (Fig. 2.8). The time series of potential temperature also indicates a gradual warming of the surface layer towards the shear line. At about 1300 UTC, the visibility severely worsened, and the aircraft had to climb to a higher altitude of ≈300 m ASL for safety reasons. As evident in Figs. 2.5, 2.6, the

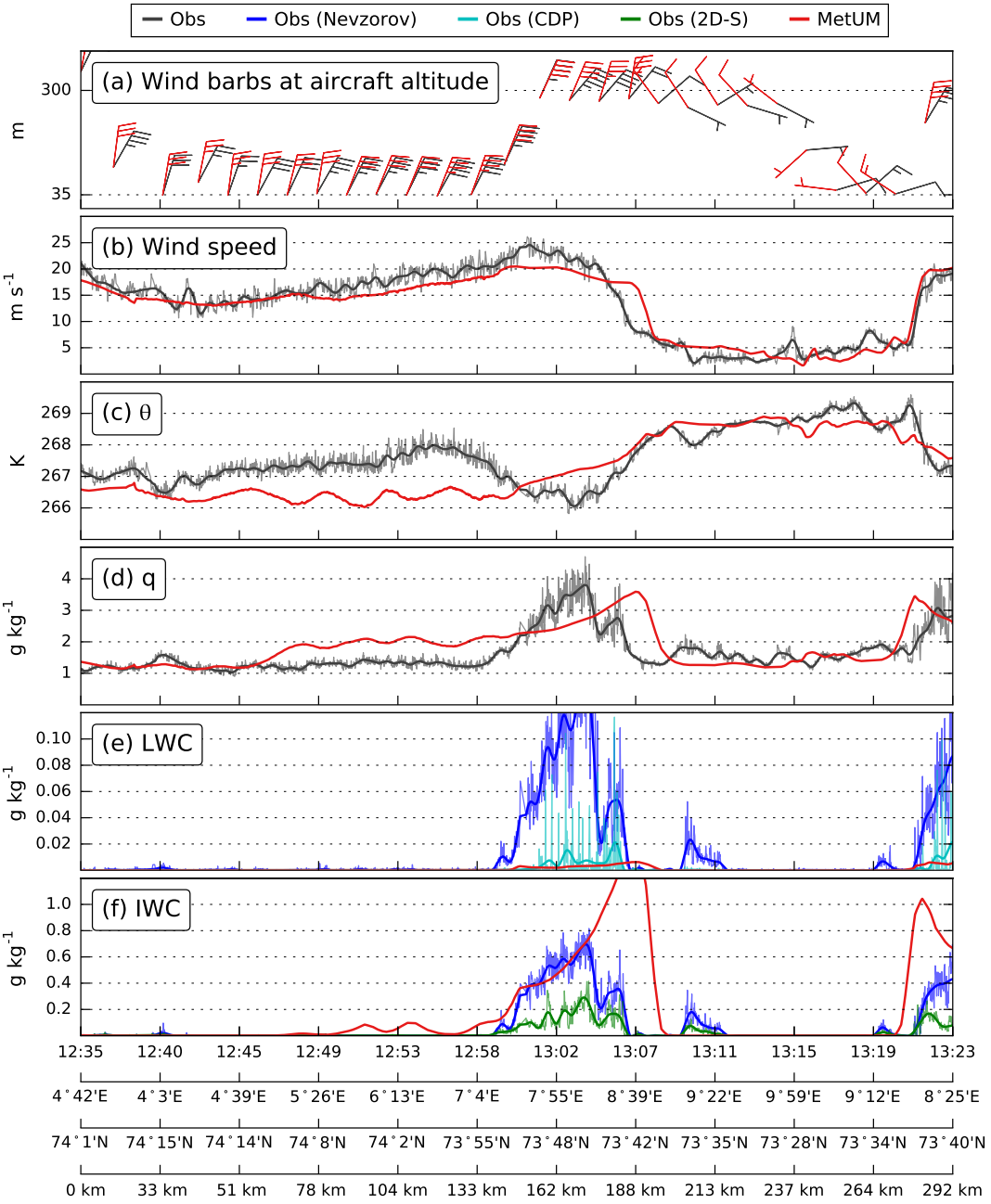

FIGURE 2.8: Time series of aircraft observations from low-level flight legs (D-A) and corresponding MetUM output. From top to bottom: wind speed and direction (barbs in standard meteorological notation) at aircraft altitude (m) measured by radar altimeter; wind speed ($m\,s^{-1}$); potential temperature (K); total specific humidity ($g\,kg^{-1}$); cloud LWC ($g\,kg^{-1}$) and cloud IWC ($g\,kg^{-1}$). Thin curves show the original measurements, while thick curves show time series smoothed by 50-second 6-order Butterworth filter.

boundary layer wind field was well-mixed and the change in altitude does not affect the representation of the shear line greatly.

Corroborating the dropsonde data from an hour earlier, the horizontal shear line

appears as a dramatic fall in wind speed over a distance of about 20–30 km. The atmospheric conditions within the shear zone are also characterised by a peak of water content. The specific humidity (Fig. 2.8d), for instance, reaches 4–5 g kg^{-1}, while the ambient values for the surrounding air mass are 1–2 g kg^{-1}. The peaks in specific humidity, as well as in liquid water and ice particles (two bottom panels, respectively), are related to the shear-line cloud wall. The cloud base resides very close to the sea surface as is evident in the peaks of cloud water content (cloud characteristics are presented in more detail in Sec. 2.6.4).

In the tranquil zone SE of the jet core (starting at 1307 UTC), wind speeds are 5 m s^{-1} or less; while the direction changes from NE to SE, a transition that is not well captured by the simulation. The near surface measurements reveal cloud-free atmospheric conditions with higher potential temperature. The low-level boundary layer stratification is close to neutral with θ =268.5 K, at least within the lowest 300 m.

After the aircraft descended, it took a U-turn to head NW in the hope of probing the shear-line again, but this time close to the sea surface. This accounts for the shear line appearing for the second time at the far right of Fig. 2.8. This second encounter with the shear zone is valuable as it confirms the observations of the dramatic wind speed gradient, concomitant temperature gradient, and the cloud wall.

It is obvious that the MetUM capably reproduces the conditions within the surface layer in and around the shear zone, particularly the wind field, where the average error is only about 2 m s^{-1}, and the match in gradients is almost perfect. The structure of the temperature field is predicted with high skill, although the horizontal gradients are slightly different. On a scale of the full low-level leg, the frontal zone in the model is steeper than in reality; while on a scale of a few kilometres, fluctuations of the temperature in the model are smoother than those observed.

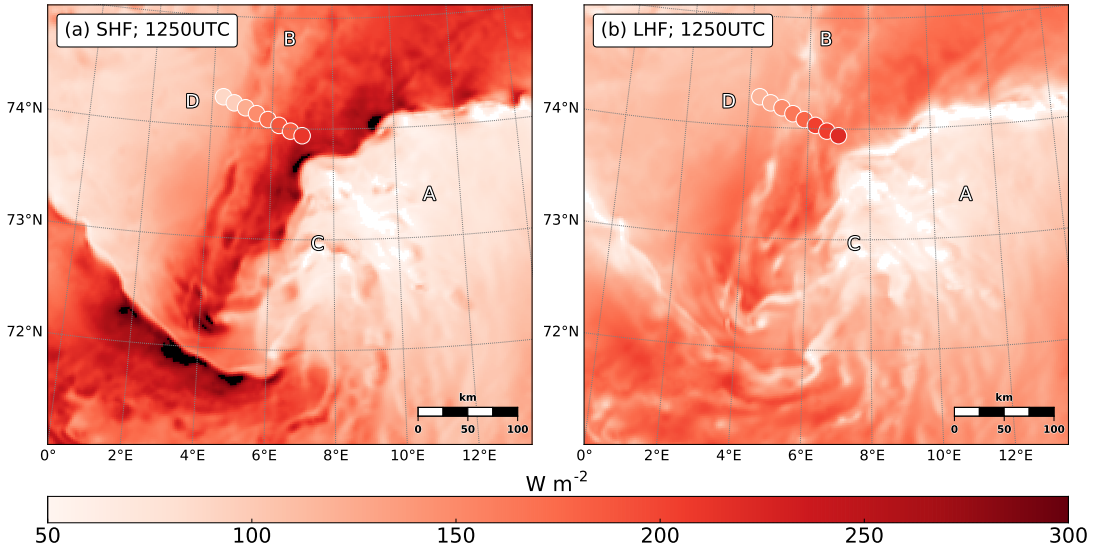

FIGURE 2.9: Surface sensible (left) and latent (right) heat flux (W m^{-2}) from the model (colour shading) and bulk flux estimates from the aircraft observations (coloured circles) at 1250 UTC.

An intensive surface heat exchange is maintained by turbulent mixing underneath the strong low-level jet. Heat transfer from the ocean to the atmosphere exceeds 500 W m^{-2} and it is most intensive within the developing PL, where the wind speed also has the largest values. On average, the sensible heat flux (SHF) topped the latent heat flux (LHF) by at least a factor of 2 and reached ≈350 W m^{-2} (Fig. 2.9). The SHF has two distinct maxima, one to the NW of the observed shear line and the other one to the S of the second shear-dominated flank of the PL. The LHF is largest to the south of the PL, where the wind velocity is smaller, though the moisture deficit is larger. Along the NE shear line, the LHF has values up to 220 W m^{-2}. Note the SHF and the LHF maxima do not always coincide, and the Bowen ratio is not necessarily equal to 2 at a given location. Furthermore, the ratio of the fluxes in Fig. 2.9 is overestimated by the model, as discussed in the next paragraph. Both the SHF and LHF patterns follow the NE shear line waves (compare to Fig. 2.5d).

The MetUM's representation of the boundary layer fluxes is supported reasonably well by in situ observations. SHF and LHF were calculated along the 35 m flight legs from measurements of wind, temperature, water vapour mixing ratio, and radiometer measurements of SST using the COARE[2] 3.0 algorithm as well as the eddy-covariance technique (methodology is described in Cook and Renfrew (2015)). Only the bulk fluxes are shown here. The circles in Fig. 2.9 show where the flux estimates were made at a flight altitude of 35 m and before the aircraft encountered the cloud wall of the shear-line. Compared to the observations, the model overestimates the SHF by ≈30 W m^{-2}, a discrepancy which can be explained by a mismatch in temperature differences. Indeed, $\theta_a - \theta_s$ is 2–3 K greater in the model than in observations. Scaled by the temperature difference factor only, the modelled values almost exactly match the observed ones. LHF, on the other hand, is underestimated by the MetUM by ≈65 W m^{-2} and this is most likely due to the overestimated values of specific humidity in the atmosphere (Fig. 2.8). The absolute values of SHF and LHF stay roughly the same throughout the PL evolution and are close to some previous observational estimates (Føre et al., 2011; Brümmer et al., 2009), but lower than others (Shapiro et al., 1987; Wagner et al., 2011).

2.6.4 Cloud structure

CloudSat measurements taken at around 1130 UTC elucidate the large-scale vertical cloud structure across the shear line and close to the PL centre. Radar reflectivity, as well as IWC and LWC are shown in Fig 2.10 and a corresponding cross-section from the MetUM simulation is given for each of these parameters. To obtain radar reflectivity we used the Cloud Feedback Model Intercomparison Project Observation Simulator Package included in the MetUM (Bodas-Salcedo et al., 2011). Note that the x-axes of Fig. 2.10 panels are reversed so the plots run NW to SE.

[2]The Coupled Ocean-Atmosphere Response Experiment

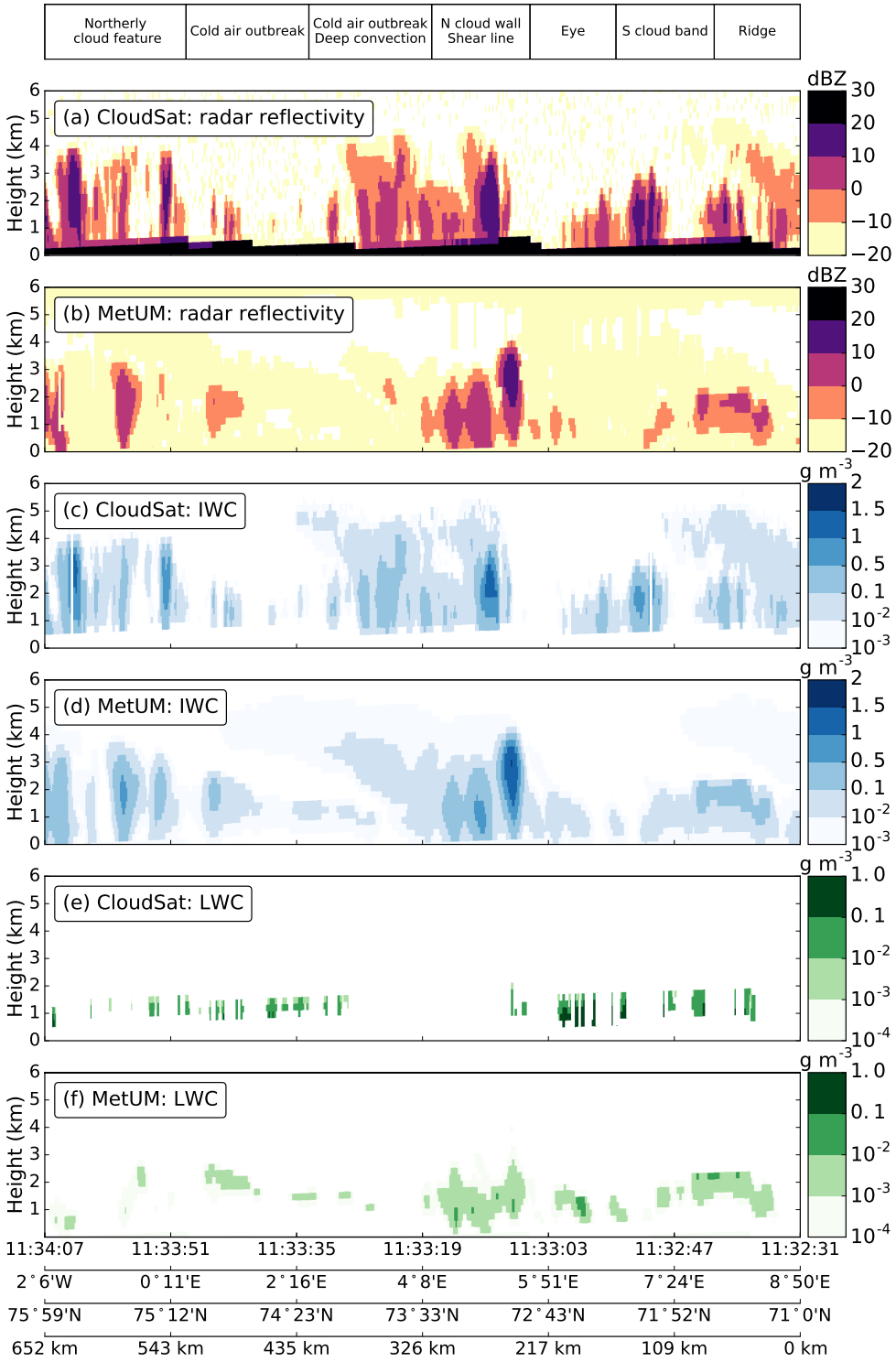

FIGURE 2.10: Cloud structure across the PL core region at 1130 UTC. From top to bottom: CloudSat radar reflectivity (dBZ); MetUM radar reflectivity (dBZ); CloudSat radar IWC density ($g\,m^{-3}$); MetUM IWC density ($g\,m^{-3}$); CloudSat radar LWC density ($g\,m^{-3}$) and MetUM LWC density ($g\,m^{-3}$).

The strongest radar echo (>20 dBZ) concurs with the shear line location, giving further evidence for the vigorous wall of clouds, which the aircraft encountered carrying out low-level measurements (Fig. 2.8). The high-reflectivity patch is identified as a cumulus-type cloud tower ≈4 km tall and ≈20 km wide, embedded in a conglomerate of shallow convective cells within the frontal part of the CAO. The calm zone to the SE, which can be labelled as a polar-low eye, is decently captured by the MetUM, although the location of individual clouds seems to be misplaced and underdeveloped. Large amounts of IWC are found within the cloud bands. In the shear-line cumuli IWC reaches 1–1.5 $g\,m^{-3}$ at roughly 3 km height. The model has similar values but places the IWC peak ≈1 km too high. Underestimating the amount of ice crystals and water droplets in the SE stratocumulus bands, the model contaminates the PL eye with low-level clouds mainly due to high IWC concentrations (Fig. 2.10d). This substantiates the mismatch between the predicted and observed in situ values of specific humidity and LWC, shown in the bottom plots of Fig. 2.8.

The CloudSat estimate of LWC is shown in Fig. 2.10e in the same units but over a different range than for IWC. The liquid water is confined to the lowest 2 km and its concentration exceeds 1 $g\,m^{-3}$. The modelled LWC is more vertically spread than CloudSat records, and generally has lower values. The integral measurement of water content — liquid water path — is drastically mismatched. Ice water path, on the other hand, displays a better agreement, particularly in the shear-line region. In the northernmost segment of the track (left part of the panel 2.10a) CloudSat detected several bands of strong convection, which are visible in the AVHRR infra-red imagery too (Fig. 2.1). The presence of the convective bands indicates another region of instability due to the bending of a vorticity filament tail (Fig. 2.4f), that grew upstream of the observed PL and wasn't well reproduced.

To further analyse the intricate structure of the cloud bands in the vicinity of the PL, we present the unique set of cloud microphysical equipment on-board the FAAM aircraft (Fig. 2.11, see Sec. 2.2.1). These measurements were taken from ≈6 km to ≈40 m ASL along the descending leg (C-D), when the aircraft was piercing the shear line in the SE-NW direction (1214–1238 UTC). A moist well-mixed subcloud layer is present up to about 600 m ASL, followed firstly by tenuous layers of frozen water and then by a peak in liquid water at 1 km. The main cloud tower extends from 1.2 km up to the wind steering level at about 4.5 km, manifested by the IWC of at least 0.2 $g\,kg^{-1}$ (Fig. 2.11e). The clouds are densest at ≈1.8–2 km, where both ice crystals and water droplets have maximum concentrations and which also contribute to the peak in total humidity (1.6 $g\,kg^{-1}$, Fig. 2.11c).

The smoothed CDP and Nevzorov data consistently show that the LWC reaches 0.05 $g\,kg^{-1}$. Within the main cloud layer, the MetUM does not reproduce the increase in liquid droplets, but reproduces the IWC peak to a better degree, especially when compared to Nevzorov estimates, albeit placing it 500 m too low. Above 2 km, the

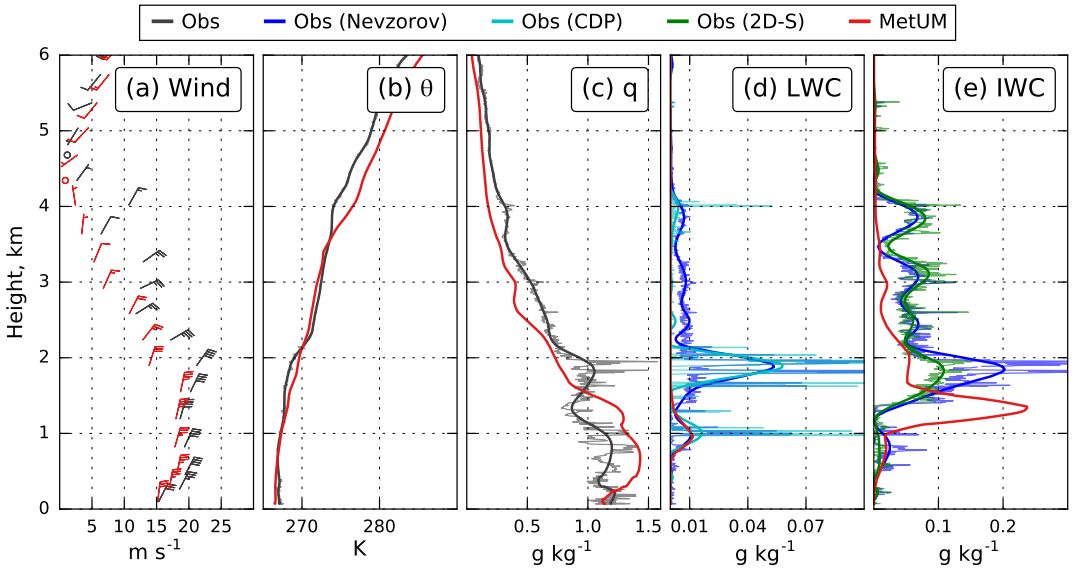

FIGURE 2.11: Profile of aircraft observations along the descending profile (C-D) and corresponding MetUM output. From left to right: wind speed and direction; potential temperature (K); total specific humidity ($g\,kg^{-1}$); cloud LWC ($g\,kg^{-1}$) and cloud IWC ($g\,kg^{-1}$).

cloud particle concentration is 2–3 times lower than the maximum, and the cloud consisted mostly of ice crystals. The LWC has a distinct 'lid' at a temperature of $\approx -20°C$, which is lower than reported in other ACCACIA flights (Lloyd et al., 2015) and model studies (Field et al., 2014). This distinct top in LWC is also seen in the CloudSat data and to an extent in the MetUM (Fig. 2.10e,f).

Overall, the clouds along the descending profile are characterized by the ratio of IWC and total water content (TWC) fluctuating near 0.8, according to the Nevzorov probe. This demonstrates that the ice phase prevails over the liquid phase, although the cloud can be still categorised as mixed-phase (Korolev et al., 2003). Meanwhile, the MetUM's IWC/TWC ratio stays around unity throughout the whole troposphere, only dropping to 0.6 within the lowest mixed-phase cloud layer at ≈1 km. It is worth noting that the CloudSat postprocessing algorithm appears to need some adjustment, because the IWC/TWC ratio is higher than that retrieved by the in situ observations.

The cloud structure of the shear-line was measured twice during the horizontal flight legs, firstly at 300 m from SE to NW (1300 UTC, 1.5 h after the CloudSat pass, see Fig. 2.8) and then at 860 m from NW to SE (2 h after CloudSat, see Fig. 2.12). Since the time gap between these legs is only ≈30 min, we can assume that the aircraft was in the same cloud band. Total specific humidity (q) exhibits a maximum of $>3\,g\,kg^{-1}$ within the shear-line cloud wall and does not change significantly between the two legs. The cloud wall is associated with an increase in LWC: smoothed CDP data give $0.02\,g\,kg^{-1}$ at 300 m and almost $0.1\,g\,kg^{-1}$ at 860 m. The spatial distribution of liquid droplets is in a good agreement between CDP and the Nevzorov probes, although

the latter tends to overestimate absolute values of LWC due to a residual effect of ice on the LWC sensor (Korolev et al., 1998). This effect is likely to be at work during the descending profile (above 2 km) and during the low-level flight (Fig. 2.8e), where CDP shows little evidence of liquid phase particles; which is also close to the MetUM results.

The MetUM shows a prominent peak of IWC that collocates with the shear line and extends throughout the boundary layer, with values exceeding 1 g kg^{-1} (Fig. 2.8, 2.12). Nevertheless, the cloud wall is characterised by mixed-phase conditions. Within the cold air mass (within the first 50 km in Fig. 2.12e,f), the clouds are weakly glaciated. There, the MetUM performs decently in representing the smoothed IWC time series. Although the 2D-S probe shows consistently lower estimates than the Nevzorov probe and the MetUM, the LWC is still substantially underestimated by the model, which also fails to accurately simulate several convective clouds to the NW of the shear line, visible as peaks and troughs in water content a few kilometres in diameter. Recent investigations of the mixed-phase cloud formation in turbulent environments suggested that changing one of the key parameters in the non-local boundary-layer scheme might be beneficial by allowing for disruption of cumulus formation through vertical wind shear (Hill et al., 2014). However, in our sensitivity runs, the MetUM generated too many ice particles in one cloud layer, and too few in another, so the 'simple fix' of adjusting the boundary-layer parameterization seemed dubious.

One of the most important findings revealed by the cloud analysis is the high intensity of convective cells in the forefront of the CAO, indicating the importance of latent heat release in fuelling the PL. The radar echo pattern resembles that reported by Forsythe and Haynes (2015). In their study the reflectivity values also reach 20 dBZ within a cloud band of a Labrador Sea PL. The same values were reported by Kawashima and Fujiyoshi (2005), who studied meso-γ-scale snow bands over the Japan Sea using two Doppler radars. When compared to a tropical cyclone, PLs have similar radar reflectivity, but with maxima confined to the lowest 5 km (Tourville et al., 2015).

2.7 Synthesis and conclusion

We examined the structure of a meso-β-scale shear-line PL that developed over the Norwegian Sea on 26 March 2013 using a combination of in situ and remote observations and convection-permitting numerical modelling.

In late March 2013, the synoptic situation was favourable for PL generation, with an intense marine CAO bringing Arctic air masses over the relatively warm Norwegian Sea in the rear sector of a large-scale low. The northerly air streams were apparently deflected by the orography of the Svalbard Archipelago, leading to convergence lines — vorticity bands — and the formation of mesoscale cyclones.

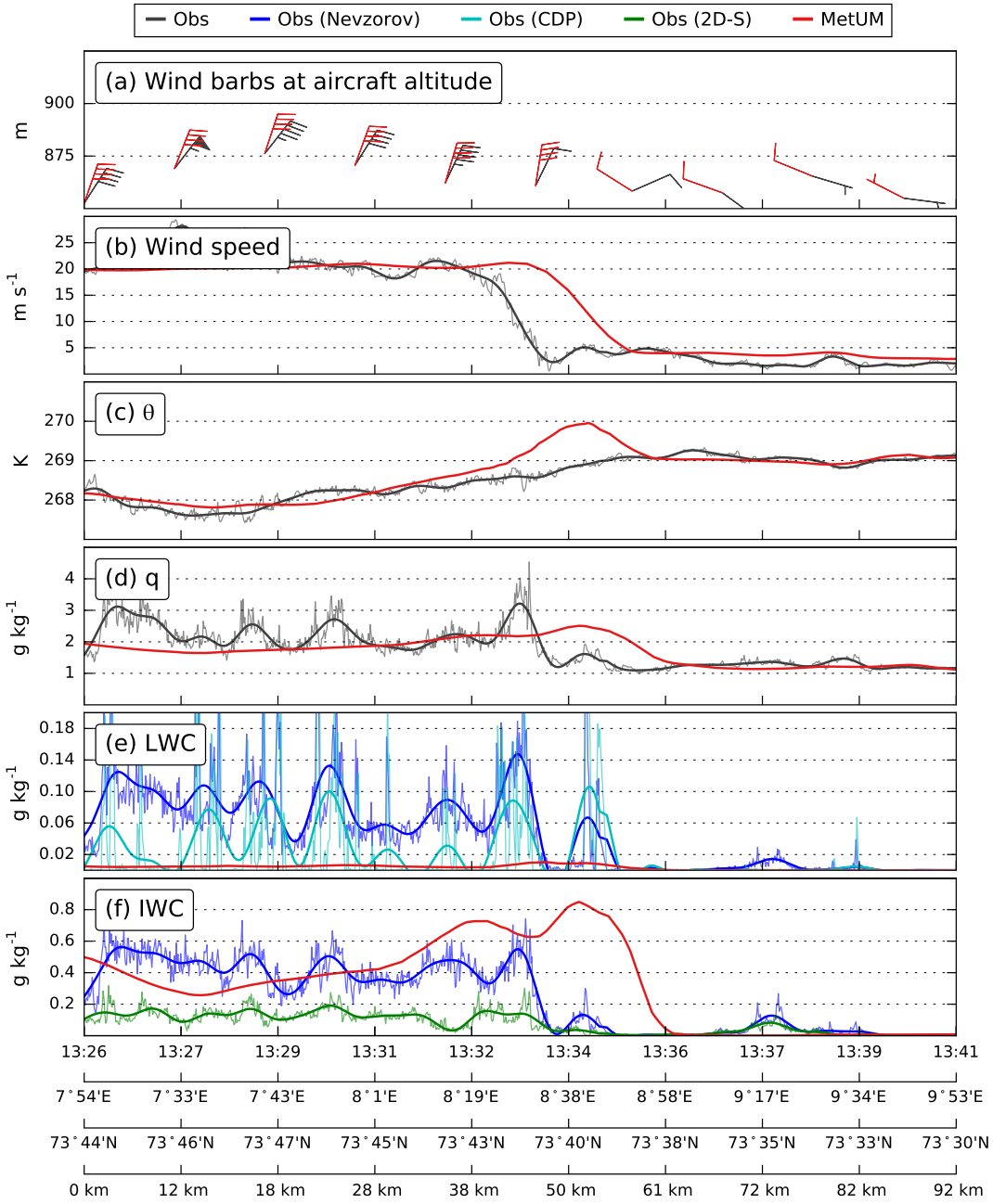

FIGURE 2.12: Time series of aircraft observations at about 860 m altitude and corresponding MetUM output, as in Fig. 2.8.

Broadly speaking, the observed PL was successfully simulated by the MetUM. The airborne observations demonstrate that the shear line shape and magnitude were successfully captured. The ASCAT's ocean wind vector estimates did not resolve the meso-γ-scale features, resulting in positive and negative wind speed biases. The dropsondes released across the shear line suggest that the horizontal shear zone was 3000 m deep and less than 50 km wide. The wind speed within the low-level jet reached 27 m s^{-1}, yielding relative vorticity of more than 10^{-3} s^{-1} along the shear line and

near the PL centre. Similar values have been found in chains of mesocyclones over the Japan Sea (Nagata, 1993; Watanabe and Niino, 2014). The vertical cross-sections demonstrate a decrease of wind speed with height that is typical for a reverse-shear PL (Terpstra et al., 2016). Representative of PL eye conditions, the cloud-free zone SE of the shear-line has relatively high temperatures ($\approx$268 K), low wind speed ($<$5 m s^{-1}) and low total specific humidity ($\approx$1.5 g kg^{-1}).

Analysis of the low-level aircraft measurements sheds light on the boundary-layer structure inside the CAO. The atmosphere near the ocean surface appears to have a neutral to slightly unstable stratification. In the model, the surface layer is insufficiently mixed, leading to a 3 K error in the vertical gradient of potential temperature, and consequently an overestimation of the SHF of roughly 30 W m^{-2}. The model also features too humid Arctic air, which results in an unduly low LHF. Within the shear zone, however, θ is close to the observed values, and we expect the total turbulent heat exchange, exceeding 500 W m^{-2}, to be close to reality.

As far as cloud structure is concerned, the shear-line is concomitant with a mixed-phase cloud band. The MetUM recreates the total humidity profiles reasonably well, but struggles to balance the ice crystal and water droplet concentrations, which is in accordance with the recent study of CAOs by Hill et al. (2014). The clouds appear over-glaciated, suggesting the model is too efficient at removing liquid water: the simulated LWC is at least 1 order of magnitude smaller than that observed.

A novel approach presenting the PL structure via CloudSat data is used. Its radar provided a cloud profile across the shear line and the PL. Supporting the airborne observations, the shear line corresponded to intense convection with vertical velocity $>$0.5 m s^{-1} and radar reflectivity exceeding 20 dBZ. Both the MetUM and CloudSat reveal that the convective clouds around the PL centre are mostly mixed-phase below 2.5 km ASL and glaciated above, where IWC reaches 1.5 g m^{-3}. The model does not fully reproduce the southern cloud wall of the PL, as well as some parts of the CAO cloud bands. Overall, the CloudSat data was corroborated by the aircraft observations and proved to be useful in model verification — a great asset for PL research.

Further research is needed to understand the evolution and dynamics of this and similar shear-line PLs and their sensitivity to the upstream orography. In particular, future studies could aim to quantify contributions of different energy sources for the PL development. This might elucidate the role of barotropic instability within the vorticity filaments, which could be as important as convection and latent heat release.

3

Modification of polar low development by orography and sea ice

This chapter is based on a publication that has been accepted for publication in the Monthly Weather Review journal with the same title. The text in the chapter is largely unchanged from the submitted manuscript apart from the model description which has been shortened to avoid repetition of Chapter 2. All references to Sergeev et al. (2017) have been changed to 'Chapter 2'. D.E. Sergeev was responsible for the work, under supervision by I.A. Renfrew and T. Spengler, who provided scientific input and helped revise the text for publication. The comments of three anonymous reviewers also helped to improve the manuscript.

3.1 Introduction

High-latitude mesoscale cyclones, and their intense sub-category polar lows (PLs) usually occur concomitantly with marine cold air outbreaks (CAOs). The Svalbard archipelago is the major orographic obstacle for these CAOs in the Norwegian and Barents seas and climatological studies (e.g., Condron et al., 2006; Michel et al., 2018) report a maximum of mesoscale cyclone activity in its vicinity. With retreating Arctic sea ice (Cavalieri and Parkinson, 2012), PL activity is predicted to move mainly northward (Zahn and Storch, 2010) and north-eastward (Romero and Emanuel, 2017); although Michel et al. (2018) suggest no significant correlation between PL activity

and sea ice extent in the North Atlantic has been observed so far. This controversy calls for more investigation of the mechanisms of cyclone interactions with the surface. In this paper, we present a high-resolution modelling study of two PL events in the Norwegian Sea and examine their sensitivity to Svalbard's orography and the sea ice distribution around it.

Orographic barriers generate flow distortions that may evolve into PLs in high latitudes (Rasmussen, 1981). In general, the potential impact of orography on the atmospheric flow is dependent on the wind speed and the stability of the atmosphere as well as the size and shape of the barrier. These parameters are encapsulated by the non-dimensional mountain height and the horizontal mountain aspect ratio (Smith, 1989a). Depending on these criteria, the flow over mountains can affect cyclogenesis via upstream blocking, flow splitting and lee vorticity stretching.

Low-level flow blocking by an elongated mountain can hold back the flow creating more favourable conditions for mesoscale cyclone growth downstream. For example, Watanabe et al. (2017) found that the mountain ridge on the northern coast of the Japan Sea blocks dry and stably stratified air from Eurasia; in simulations without these mountains, the continental CAO sweeps mesoscale cyclones closer to Japan, leaving less opportunity to gain energy over the warm sea, leading to landfall prior to full development. Although the highest peak of Svalbard is only 1717 m, the flow distortion associated with the archipelago is comparable to that of far higher mountains due to the climatologically high static stability (Skeie and Grønås, 2000).

Lee cyclogenesis has been reported to produce mesoscale lows in the North Atlantic (Petersen et al., 2003), the Japan Sea (Watanabe et al., 2018), and the Ross Sea (Gallée, 1995). Via a series of sensitivity experiments, Kristjánsson et al. (2011) show that the orography of eastern Greenland can lead to a spin-up of low-level circulation that develops into an intense PL over the Denmark Strait. The subsidence associated with vortex stretching and adiabatic warming is absent without Greenland. On a smaller scale, lee vorticity production can be invigorated by katabatic winds, as shown by Gallée (1995) for the Antarctic peninsula. Katabatic convergence in the wake of Greenland can also be conducive for the formation of mesoscale cyclones (Klein and Heinemann, 2002). Similar effects have not been investigated around Svalbard.

The flow deflection by a mountain with sufficient non-dimensional height can produce low-level jets at its flanks, referred to as 'tip jets' (Doyle and Shapiro, 1999; Renfrew et al., 2009b; Outten et al., 2009). They regularly appear near the southernmost point of Greenland (Moore and Renfrew, 2005). Tip jet formation has also been observed at the southern cape of Spitsbergen, the largest island of the Svalbard Archipelago (Reeve and Kolstad, 2011). The shear vorticity associated with such jets can create a conducive environment for barotropic instability (Skeie and Grønås, 2000), potentially leading to cyclogenesis. However, a link between the flow distortion caused by Svalbard and local PL activity remains unclear (Bracegirdle and Gray,

2008). To our knowledge, there has been scarcely any research focused on the mechanisms by which such flow responses to orography may contribute to the development of PLs. Thus the first question we address here is *to what degree does the presence of Svalbard affect PL formation and spin-up*.

PLs are also sensitive to the sea ice and sea surface temperature (SST), via their influence on low-level baroclinicity and surface heat fluxes. The sea ice edge represents a zone with sharp gradients of temperature and albedo, resulting in shallow baroclinic zones which can spawn mesoscale vortices (e.g., Harold et al., 1999b). In addition, differences in surface roughness between the open water and the ice can result in shear vorticity generation and consequently barotropic cyclogenesis (Rasmussen and Turner, 2003).

The shape of the sea ice edge is important in the formation of a downstream convergence zone that can be favourable for PL generation. This mechanism of mesoscale cyclone development was addressed by Heinemann (1997) in idealised numerical simulations of Weddell Sea vortices. Due to the differential heating in that region, pressure fell in a belt parallel to the sea ice edge, forming a meso-β-scale (about 200 km in diameter) circulation. In Albright et al. (1995) the intensity and location of a PL in Hudson Bay was found to be strongly dependent on the upstream sea-ice edge. The sea ice edge in the Svalbard region has a concave shape forming a bay of open water to the west of the archipelago, which is potentially conducive to convergence within CAOs, and this could influence mesoscale cyclone generation.

Turbulent heat fluxes over the sea ice are too small for PL intensification, whereas over the ice-free ocean they can create a favourable environment for PLs by destabilizing the atmosphere. In order to reproduce a baroclinic PL moving north-eastward, Adakudlu and Barstad (2011) modified the SST and sea ice cover over the Barents Sea. The removal of sea ice allowed the simulated PL to develop and persist for longer than in a control case. In addition, increased SST led to a strong vertical coupling between the PL and an upper-level potential vorticity (PV) anomaly. A recent study by Watanabe et al. (2017) also demonstrates that the sea ice configuration in the Sea of Japan and the Strait of Tartary is conducive to the development of mesoscale vortices. In a sensitivity experiment with increased sea ice cover and reduced SST the fluxes from the surface are limited resulting in a more stably stratified atmosphere, reducing the influence of upper-level forcing. In the context of the Nordic seas, we address the following second question: *what influence does the sea ice extent near Svalbard have on PLs?*

3.2 Data and methodology

3.2.1 Polar low cases

In order to find suitable cases, we perused the Sea Surface Temperature and Altimeter Synergy for Improved Forecasting of Polar Lows (STARS) database, which is freely available to the community[1]. It contains a total of 140 PL tracks in the north-east Atlantic for the period 2002–2011. After manual inspection of the cloud imagery and PL tracks, a dozen candidates (including the PL from Chapter 2) were chosen based on their proximity to Svalbard and general southward propagation. These criteria imply that we are interested in PLs that originate immediately downstream of the archipelago in the air streams coming from the sea ice. Following preliminary simulations of all of these cases, here we present two cases which are illustrative of the range of PL examined: from the 5–6 April 2007 (STARS-72) and from the 30-31 January 2008 (STARS-77).

These two cyclones are well-reproduced by the numerical model and have well-defined circulations that facilitate their tracking and clarify the analysis of sensitivity experiments. Both PLs developed in a classic northerly CAO (Papritz and Spengler, 2017) and spawned very close to Svalbard, raising the possibility of its importance in their development. The two cases are somewhat different in terms of dynamical forcing, as discussed later.

3.2.2 The Met Office Unified Model

We use the same configuration of the UK Met Office's Unified Model (MetUM) as in the previous chapter, where it was validated against aircraft and satellite observations of a shear-line PL.

Sea ice extent and SST are derived from the Operational Sea Surface Temperature and Sea Ice Analysis (OSTIA) at 17 km resolution and bi-linearly interpolated to the nested model resolution. The elevation is taken from the GLOBE dataset (Webster et al., 2003) with a grid spacing of 1 km.

Three-dimensional fields are analysed on isobaric surfaces (29 equally spaced levels spanning 1000–300 hPa). The code used in this study is available on GitHub[2].

3.2.3 Trajectory analysis

To investigate how the PLs form and obtain their warm cores, we calculate kinematic trajectories backward in time, applying the LAGRangian ANalysis TOol (LAGRANTO) 2.0 (Sprenger and Wernli, 2015) to the MetUM output of the 3 wind components and sea level pressure (SLP). Similar trajectory analysis of PLs over the Japan

[1] http://polarlow.met.no/stars-dat
[2] https://github.com/dennissergeev/mplosi

TABLE 3.1: MetUM settings used in the CTRL and sensitivity experiments. Note we use the same version of the model as in Chapter 2. The settings relevant to this chapter are given in the table.

Nesting suite id	`u-ae616`
Nested domain size (x, y)	600×700 grid points
Nested domain area	1320 km $\times$ 1540 km
initialisation time	
• STARS-72:	1200 UTC 04.04.2007
• STARS-77:	1200 UTC 29.01.2008
Run duration	48 h

Sea has been carried out by Watanabe and Niino (2014) and Watanabe et al. (2017), and has been proven to be useful for CAO climatology work by Papritz and Spengler (2017) as well as for the mesoscale flow interaction with topography in polar regions by Elvidge et al. (2015b). Trajectories from 5 pressure levels (950, 925, 900, 875, 850 hPa) over a 10 km $\times$ 10 km grid within the warm core of the PLs are calculated backward in time for 24 h from the time of maximum intensity (defined as the time when the PL reaches its maximum relative vorticity in the lower troposphere).

3.2.4 Experimental set-up

We start with control (CTRL) experiments for each of the two PL cases. The model domain spans most of the Norwegian and parts of the Greenland and Barents seas (Fig. 3.1). The Svalbard archipelago is near the centre of the domain. The surface temperature and sea ice cover are similar in both PL cases: namely a 'diagonally oriented' sea ice edge in Fram Strait, a bay of open water to the west of Svalbard, and sea ice to the east of the archipelago.

For each case we perform 4 additional model simulations, where we separately change the orography and sea ice edge positions. Note that *simultaneous* changes of orography and sea ice resulted in even larger differences between the CTRL and perturbed experiments. However, these results do not provide new information compared to what will be discussed for the simulations presented here and so for the sake of brevity are not discussed further.

Some additional experiments were carried out to test the MetUM's sensitivity to the initialisation time, the size of the model domain and its geographical position. In the first few hours of all experiments (CTRL and sensitivity) low-level vorticity features were indistinguishable. A few weak vorticity filaments are present at the

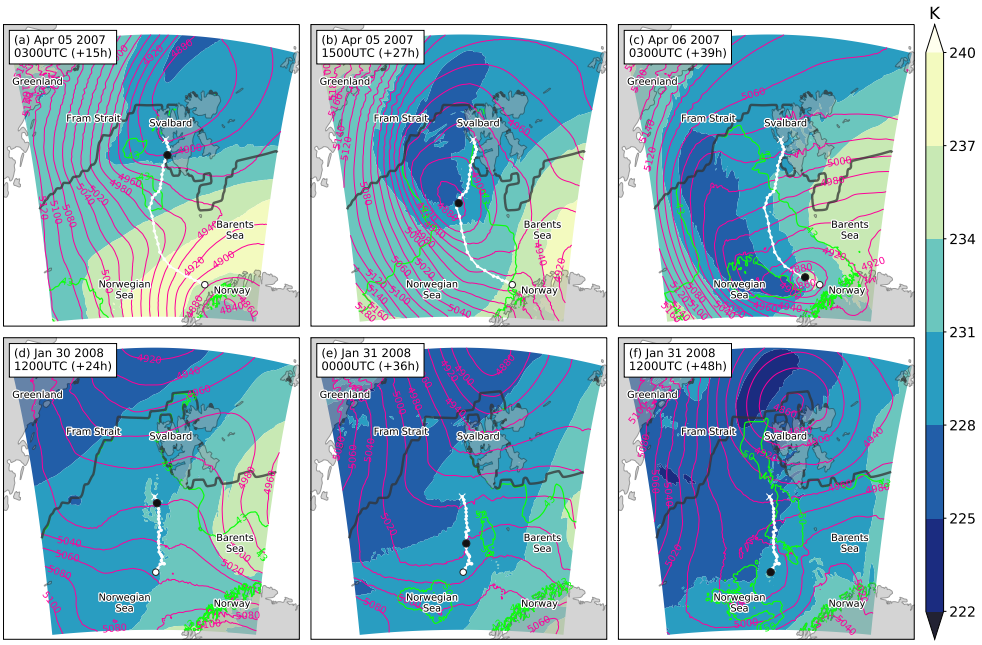

FIGURE 3.1: The model domain showing upper-level (500 hPa) conditions for the (a–c) STARS-72 case and (d–f) STARS-77 case. Shown are air temperature (colour shading, K), geopotential height (pink contours, m), $SST - T_{500}$ (selected for 43 and 50 K isotherms, green), and sea ice edge (dark grey line). The PL tracks are marked in white, a white cross showing the start, and black and white dots showing the PL location at the time of the panel and after 48 h, respectively.

beginning of the forecast, but they dissipate or are advected away from the region of future PL formation. Thus, we believe the initialisation time of the experiments is appropriate to capture the full life cycle of PLs and is not too early for the forecast to be significantly far from observations. Overall, the model produced very similar results even if the domain was twice as large or shifted by a few degrees latitude or longitude. A run with doubled grid spacing (4.0 km) generally agreed with the control runs, but did not reproduce the same amount of small convective cells. These differences in the representation of discrete convective cells do not accompany significant differences in the wind and temperature fields, as was found for a higher resolution (0.5 km grid size) simulation in Chapter 2.

3.3 Results

3.3.1 Large-scale atmospheric conditions and polar low evolution in the CTRL experiments

The surface environment prior to the PLs generation is similar in both cases. It is characterised by a quasi-zonal pressure gradient over the Norwegian Sea, between the

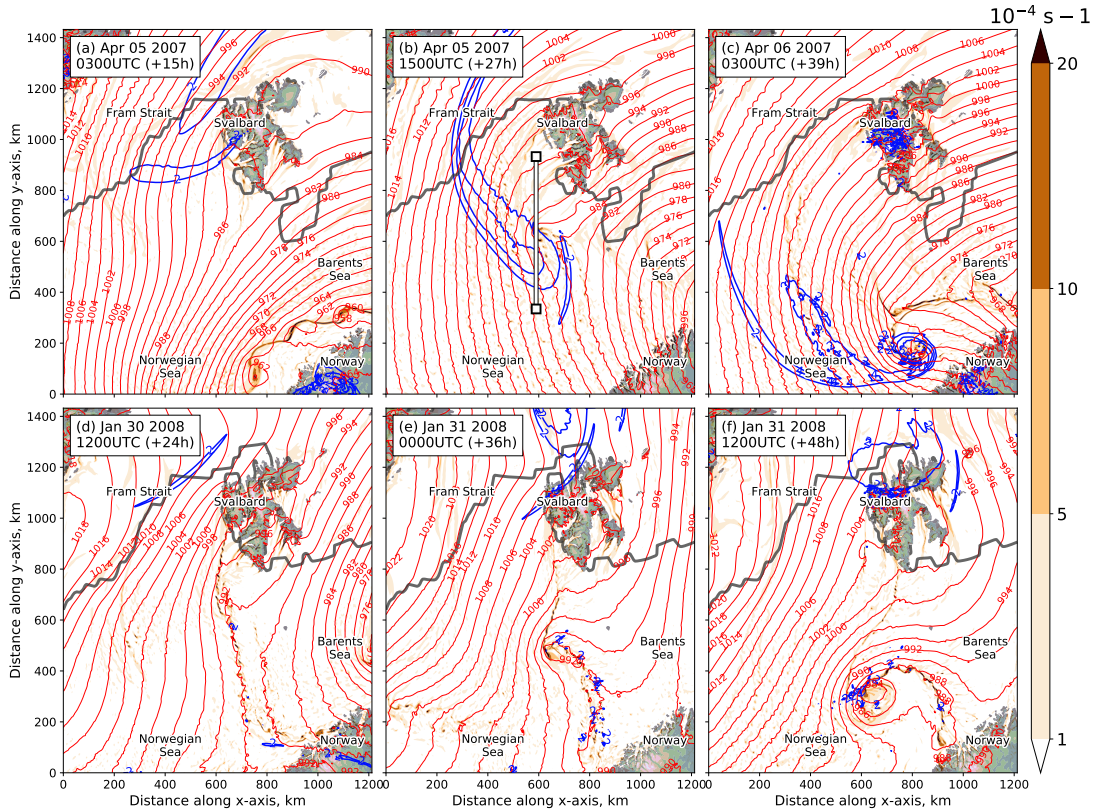

FIGURE 3.2: As in Fig. 3.1, but for potential vorticity at 500 hPa (blue contours, every 2 PVU), relative vorticity (colour shading, 10^{-4} s^{-1}) at 950 hPa, sea level pressure (red contours, every 2 hPa). The white line in (b) indicates the south-north vertical cross-section shown in Fig. 3.11. Model elevation is shown in colour shading.

western periphery of a synoptic-scale cyclone moving to the north-east and a high-pressure system over Greenland. This setting is a classic example of favourable conditions for CAOs in this area (Papritz and Spengler, 2017). Accordingly, the prevailing wind direction throughout the simulation is from the north. These synoptic conditions fall into the category of the Atlantic Ridge weather regime, which is found by Mallet et al. (2013) to be the most conducive for PL activity over the north-east Atlantic.

The upper-level conditions (Fig. 3.1) display a southward propagation of the Arctic air mass, but the geopotential height and temperature patterns differ between the STARS-72 and STARS-77 cases. In the former case, a distinct cold trough at 500 hPa forms over the Svalbard region. During the PL event, this upper-level vortex becomes more concentrated and propagates towards the Scandinavian coast, elongating the cold anomaly over the western Norwegian Sea. This is reflected in the 500 hPa PV field (Fig. 3.2a), which contains an elongated maximum that moves to the region from the north. The moment when the forefront of the PV maximum happens to pass over Svalbard (Fig. 3.2a), an embryo of the future STARS-72 PL detaches from the western coast of the archipelago (evident in low-level vorticity). As the PV filament extends southward, the SLP trough and the low-level vorticity maximum associated with the

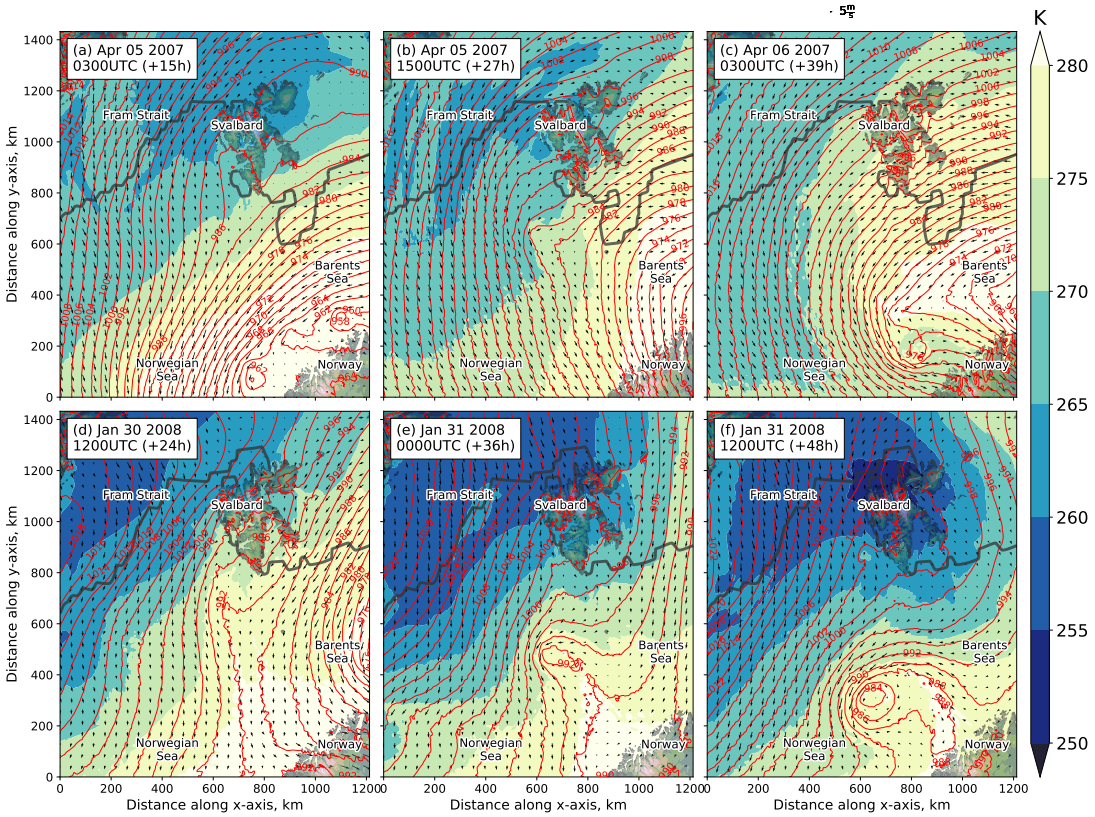

FIGURE 3.3: As in Fig. 3.2, but for equivalent potential temperature (colour shading, every 5 K) and horizontal wind (black vectors) at 850 hPa, sea level pressure (red contours, every 2 hPa).

growing PL follows it. The upper- and the lower-level PV anomalies (qualitatively similar to the low-level vorticity in Fig. 3.2) quickly become vertically aligned, with the surface PV maxima associated with convective mesoscale vortices extending up to 500 hPa (Fig. 3.1c and Fig. 3.2c). The reduction of the distance between upper- and lower-level lows, or in other words, the decrease of the baroclinic mode phase tilt in the STARS-72 case, resembles a type B cyclogenesis in the classification of Petterssen and Smebye (Deveson et al., 2002; Bracegirdle and Gray, 2009).

The STARS-77 PL's upper-level environment, on the other hand, does not possess a well-defined cold vortex, nor does it have a strong PV anomaly. The geopotential height contours at 500 hPa remain largely zonal during the life-cycle of the PL (Fig. 3.1d,e). A small upper-level trough appears above the PL at the end of the simulation due to the intensification of the surface mesoscale cyclone (Fig. 3.1f). The 500 hPa temperature field is almost as cold as in the first case, though the temperature minimum is less pronounced. The broad negative temperature anomaly in the mid-troposphere combined with slightly higher SST in the STARS-77 case indicates that the atmosphere is less stable, compared to the first case's environment, and thus more prone to convection. This difference is more pronounced in the first day of the simulations and is demonstrated by the SST and the temperature at 500 hPa difference

($SST - T_{500}$, Fig. 3.1a,d) — a proxy often used for potential PL development (Kolstad, 2011).

The low-level evolution of the STARS-77 PL begins with a series of high-vorticity banners emanating from the west coast of Spitsbergen and growing over the ice-free ocean, before coalescing into a long (up to ≈500 km) convergence line accompanied by a weak SLP trough (Fig. 3.2e and vectors in Fig. 3.3e). Due to a greater low-level convergence (not shown), stretching of the existing cyclonic vorticity intensifies the northern segment of the shear line quicker than its southern segment. Consequently, under the influence of northerly flow from Fram Strait and north-easterly flow from the Barents Sea, the vorticity line curls up into a comma-shaped PL (Fig. 3.2e,f). The barotropic nature of this wave is evident from the high horizontal gradients in the wind speed (not shown) and the characteristic scale of the vorticity waves, roughly equal to 25–30 km. Given the sharp vorticity gradient across this narrow (<20 km across) vorticity strip, Rayleigh's inflection point criterion for instability is satisfied (i.e. a maximum in vorticity is within the domain (e.g. Dritschel et al., 1991)). The barotropic wave growth is likely to be aided by latent heat release in the banded convection (Joly and Thorpe, 1990). This is related to the mechanisms examined in the idealised model experiments by Dacre and Gray (2006). This PL's high-vorticity core continues to expand, becoming more spiraliform in a similar fashion to that described by Schär and Davies (1990), while the central pressure drops below 984 hPa at the end of the simulation (Fig. 3.2f).

Both PLs develop in a similar ambient horizontal equivalent potential temperature gradient of roughly 1.5 K/100km in the lower troposphere (Fig. 3.3). The incipient mesoscale cyclones appear in the northern part of the baroclinic zone that stretches from south-west to north-east (Fig. 3.3a,d). The warm air mass and the large-scale surface low retreat to the east and are replaced by colder air brought by the CAO. The PLs develop on the eastern edge of this CAO. Towards the end of the PL life cycle, the cold air encircles warmer air, resulting in a warm seclusion in the STARS-72 case (Fig. 3.3c). The temperature stratification of the background environment is stronger in the STARS-72 case, than in the STARS-77 case. For example, the SST-500 hPa difference at the early stages of PL development exceeds 47 K in the STARS-77 case, which is 7 K larger than in the STARS-72 case Fig. 3.1. The difference in stratification is mainly due to the middle and upper levels being colder in the STARS-77 case (cf e.g. Fig. 3.1a and d). This suggests a greater role of convection and diabatic destabilisation in the STARS-77 case. The latter can represent a sufficient mechanism for PL intensification in the regions with sustained surface baroclinicity (Montgomery and Farrell, 1992). Thus the formation and growth of both PLs involves a synergy among baroclinic instability, convection, barotropic instability (for STARS-77) and upper-level forcing (for STARS-72).

The simulated top-of-atmosphere outgoing long-wave radiation plots (TOA OLR,

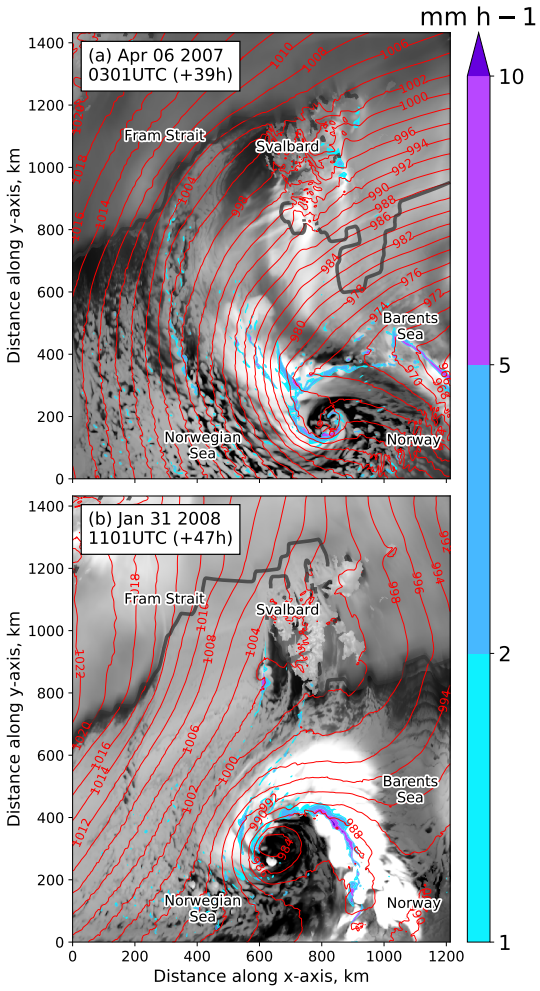

FIGURE 3.4: Simulated cloud signature (shown by TOA OLR), SLP (red contours, hPa) and precipitation rate (mm h^{-1}) at the time of maximum intensity in case (a) STARS-72 and (b) STARS-77. The sea-ice edge is shown as 15 % contour line of sea ice fraction (grey line).

see Fig. 3.4) are broadly consistent with Advanced Very High Resolution Radiometer (AVHRR) satellite images (available here: `http://polarlow.met.no`). They depict a cloud-free eye surrounded by the highest spiralling cloud bands (white shading — lowest values of TOA outgoing long-wave radiation (OLR)), with precipitation rates reaching 10 mm h^{-1}. The rest of the model domain is filled by swaths of stratocumulus clouds and convective cells or cloud streets of shallow convection typical of a CAO event.

Backward trajectory analysis shows that in both cases, more than half of the air parcels that end up in the PL centre originate from Fram Strait and to the north of Svalbard, as far as Franz Josef Land (pink lines in Fig. 3.5a,e). Their typical path goes over the ice-covered Fram Strait, bypassing Svalbard to the west, and moving in a south-eastward direction to end up in the PL. The trajectories stay below 850 hPa (in the STARS-72 case even lower) and barely change their potential temperature (θ), until

about -18 h when they enter the ice-free area. Accordingly, the air parcels' temperature and, a bit later, specific humidity begin to rise due to the strong surface heat fluxes.

The highest θ in the PL core is associated with trajectories that have the western Barents Sea as their predominant origin (yellow lines in Fig. 3.5a,e). Being already much warmer than the parcels from the north, θ along trajectories from the Barents Sea increases further due to diabatic processes (Fig. 3.5c,g, inset axes). Moisture brought by these parcels to the PL (Fig. 3.5d,h) helps to drive convection that is manifested by the upward movement at the end of the trajectories (e.g., Fig. 3.5f).

The STARS-77 case has an additional source of air that is located over the Greenland Sea and carried to the PL by westerlies at ≈600 hPa and higher (cyan lines in Fig. 3.5e). This dry air from the mid- and upper- troposphere contributes to the warm core of the PL, through the adiabatic warming during descent (cyan curve in the inset axes of Fig. 3.5g showing nearly constant θ values). The change in temperature along these trajectories is the largest of all the trajectory paths.

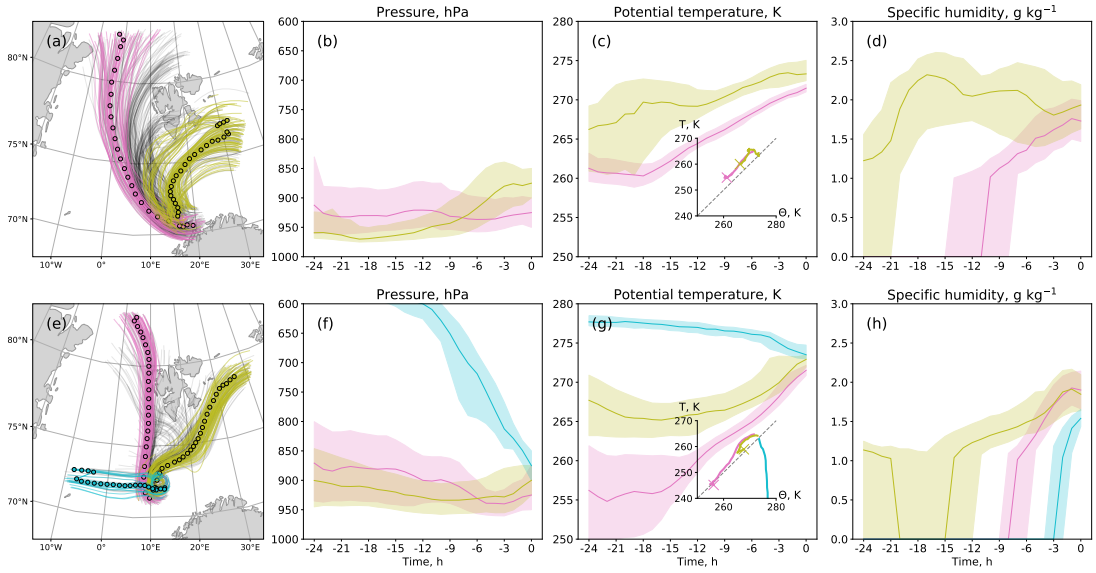

FIGURE 3.5: Backward trajectories (a, e) over 24 h and time series of (b, f) pressure, (c, g) potential temperature, and (d, h) specific humidity along the trajectories for the cases STARS-72 (top row) and STARS-77 (bottom row). Trajectories with distinct geographical origins are highlighted: north (pink), north-east (yellow), west (cyan). Grey lines depict trajectories that do not decidedly fall into any geographical category. The coloured circles show hourly positions of the air parcels along the median trajectory. The time series plots (b–d, f–h) show the median and the interquartile range by a solid line and shading, respectively. Inset axes in subplots (c, g) show the θ-T diagrams, where the first hour of the trajectory is shown by a cross. The dashed diagonal line shows 1:1 ratio of θ and T increase. Note that the geographical origins are defined by longitude-latitude boxes; even though some of the gray trajectories seem to originate in the similar area, they do not cross those boxes.

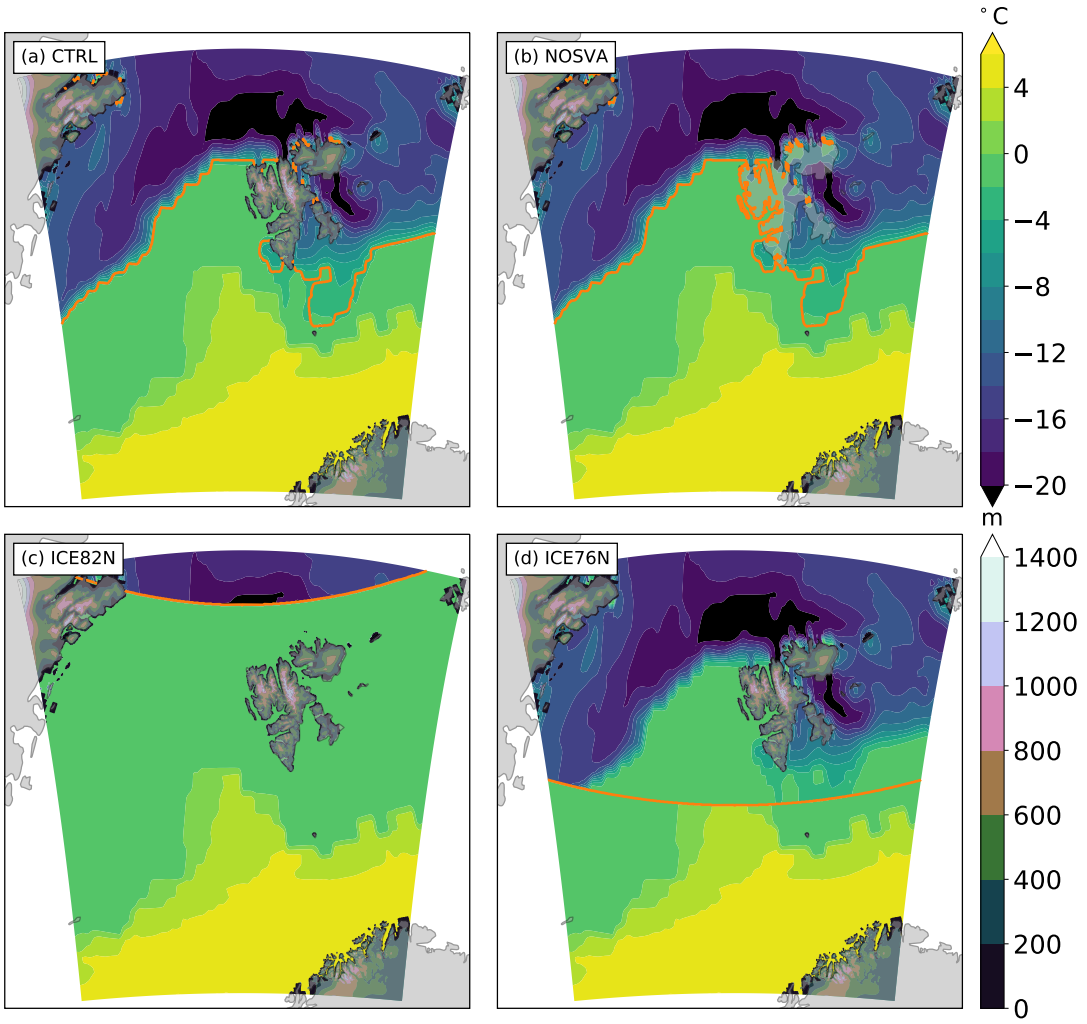

FIGURE 3.6: Surface temperature (colour shading, °C), surface elevation (colour shading, m), and sea ice edge (orange line) in (a) CTRL, (b) NOSVA, (c) ICE82N, and (d) ICE76N simulations of the STARS-72 case.

3.3.2 Sensitivity experiments

When Svalbard obstructs a CAO, it can act as a source of low-level vorticity conducive to the formation of mesoscale cyclones (e.g., Fig 3.2). In addition, the relatively warm ice-free sea surface to the west of the archipelago supplies the heat and moisture that contribute to PL development. The shape of the sea ice edge can also be vital for flow convergence (e.g., Gryschka et al., 2008). To examine the sensitivity of the PLs to these surface factors we performed a number of sensitivity experiments (Table 3.2).

The CTRL surface characteristics are illustrated in Fig. 3.6a. The NOSVA experiment has the area of Svalbard replaced by sea ice of the same coastal shape in order to elicit the influence of the archipelago's topography (Fig. 3.6b). In SVA200, Svalbard's elevation is changed by a set percentage (200 %) at each grid point. Consequently the vertical profile of Svalbard becomes steeper, but the coastal shape of Svalbard remains

the same.

TABLE 3.2: Sensitivity runs set-up.

Run	Svalbard	Sea ice
NOSVA	Replaced by sea ice	Control
SVA200	Height scaled by 200 %	Control
ICE82N	Control	Zonal ice edge at 82°N
ICE76N	Control	Zonal ice edge at 76°N

The diagonally oriented sea ice distribution in the Fram Straight and the open water next to Svalbard (see Fig. 3.6a) will lead to a diagonal pattern of heating from the surface which may supply energy to the growing convergence lines. In our sensitivity experiments, we make the sea ice edge oriented zonally and shift it to 82°N, north of Svalbard (ICE82N run, Fig. 3.6c). Then, to isolate the influence of open water west of Svalbard, we extend the sea ice cover south to 76°N (ICE76N, Fig. 3.6d). In the ICE82N experiment sea ice south of 82°N is replaced by ocean with an SST of 271.35 K (seawater freezing point). Note that changing the sea ice cover also changes the baroclinicity in the area, which is an inherent part of our experimental design. The effect of this additional factor would be better answered via idealised studies in future work.

Perturbed orography experiments

Although the PLs still develop in the perturbed orography conditions, their origin and tracks have changed (Fig. 3.7). In the NOSVA run of both PL cases, the incipient vortices still appear near the ragged western ice edge replacing Spitsbergen, but are quickly advected away from the ice edge. As a result, they are unable to join the vorticity lines produced in a merry-go-round fashion around the synoptic-scale low to the east. The initial vorticity cluster coming from Svalbard dissipates near the Scandinavian peninsula after about 21 h of existence. The primary nuclei of PLs in the NOSVA runs become the vortical disturbances generated by the north-easterly large-scale flow (compare the starting locations of the PL tracks to the ones in the CTRL runs). The NOSVA PLs develop further to the south and slightly later than CTRL PLs, likely due to the lack of vorticity reinforcement from Svalbard, illustrated in the STARS-77 case by the absence of a trailing vorticity 'tail' between the archipelago and the growing PL in Fig. 3.7e. One can notice a remnant of the vorticity filament close to the PL, but it is detached from it and is too far west. In the STARS-77 case, the NOSVA PL is weaker than in the CTRL run when assessed by such metrics as the low-level relative vorticity averaged within 150 km of the centre of the vortex (Fig. 3.8a,b). In the STARS-72 case, the intensity of the NOSVA PL takes more time to increase, but eventually matches the intensity of the CTRL PL.

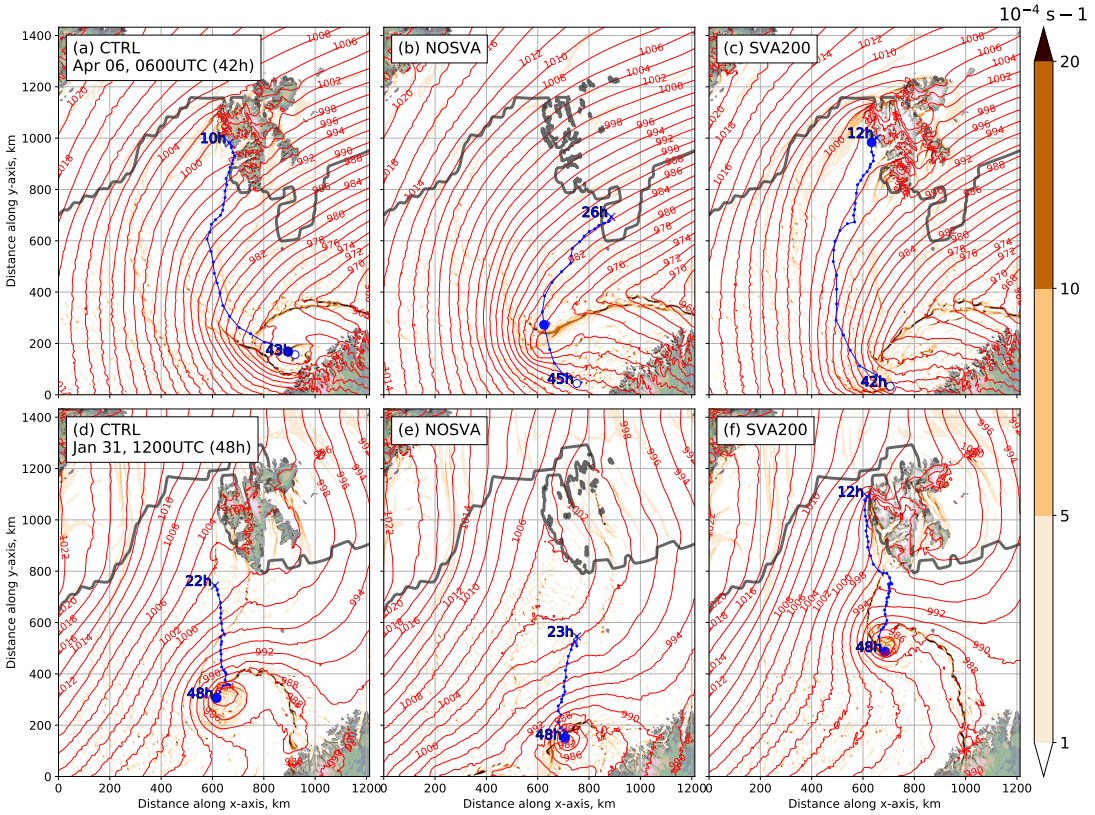

FIGURE 3.7: Results of the sensitivity experiments with changed orography at the time of maximum intensity in the control run. Relative vorticity (colour shading, $10^{-4}\,s^{-1}$) at 950 hPa and SLP (red contours, every 2 hPa) in (a, d) CTRL, (b, e) NOSVA, and (c, f) SVA200 simulations of STARS-72 (top row) and STARS-77 (bottom row). Model elevation is shown in colour shading, sea ice edge is shown by the grey line. Manually tracked PL positions are shown by blue dots. The blue filled circle shows the location of maximum intensity of the PLs. The blue cross shows the beginning of the track and the white circle shows the PL location after 48 h.

When the height of Svalbard's mountains is doubled (SVA200 runs), the fjords produce more vorticity filaments which feed the growing mesoscale cyclones. In both cases, intense tip jets are generated by the air flowing around the north-western cape (not shown), consistent with idealised experiments of Skeie and Grønås (2000) and being the major source of relative vorticity to the incipient PLs. The mesoscale cyclones are initiated closer to the archipelago, due to the topographic blocking of the CAO, i.e. Svalbard acts to divert flow around it (discussed in Sec. 3.4). They are characterised by a much higher vorticity at the beginning of their tracks, but comparable to the CTRL at the end. In fact, as shown in Fig. 3.8 the STARS-72 PL attains its vorticity maximum after about half a day of development while it is less than 200 km away from Svalbard (blue circle in Fig. 3.7c). Note this allows us to start PL tracking earlier (e.g., by 10 h in STARS-77 case), which is reflected by a longer time series of averaged vorticity (Fig. 3.8).

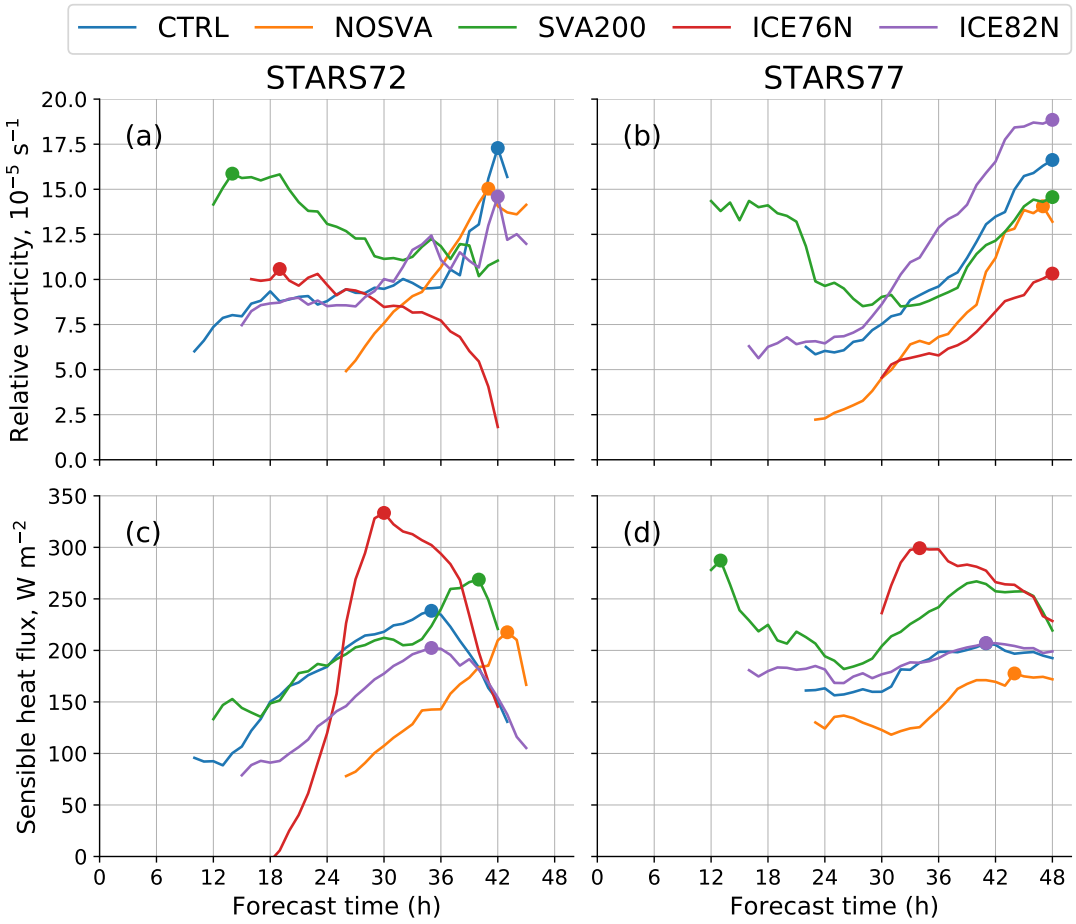

FIGURE 3.8: Time series of (a, b) average relative vorticity between 950 hPa and 850 hPa and (c, d) average sensible heat flux within 150 km radius from PL centres in (a, c) STARS-72 case and (b, d) STARS-77 case for each of the sensitivity experiments. coloured circles show maximum values of the corresponding curve.

Perturbed sea ice experiments

In the experiments with increased sea ice cover to the south (ICE76N), the vorticity maxima forming near Svalbard receive smaller flux of energy from the ice-covered surface, and so are much weaker than in the CTRL runs (Fig. 3.8, 3.9).

In the STARS-72 case, the incipient vortex gradually weakens while travelling over the sea ice. Once the cold stably-stratified air embedded within the vortex enters the ice-free area south of 76°N, the average sensible heat flux around the vortex centre spikes to almost 350 W m^{-2} (Fig. 3.8c) — comparable to other PLs with high heat fluxes (e.g. Wagner et al., 2011). However, even this boost in surface heating is not enough for the incipient vorticity maximum to evolve into a PL, and instead it disintegrates into convective disturbances which eventually make landfall in Northern Norway. The mesoscale SLP trough deepens nonetheless, and the low-level vorticity field is characterised by the strong shear line originating from the rear part of the large-scale low over the Barents Sea (Fig. 3.9b).

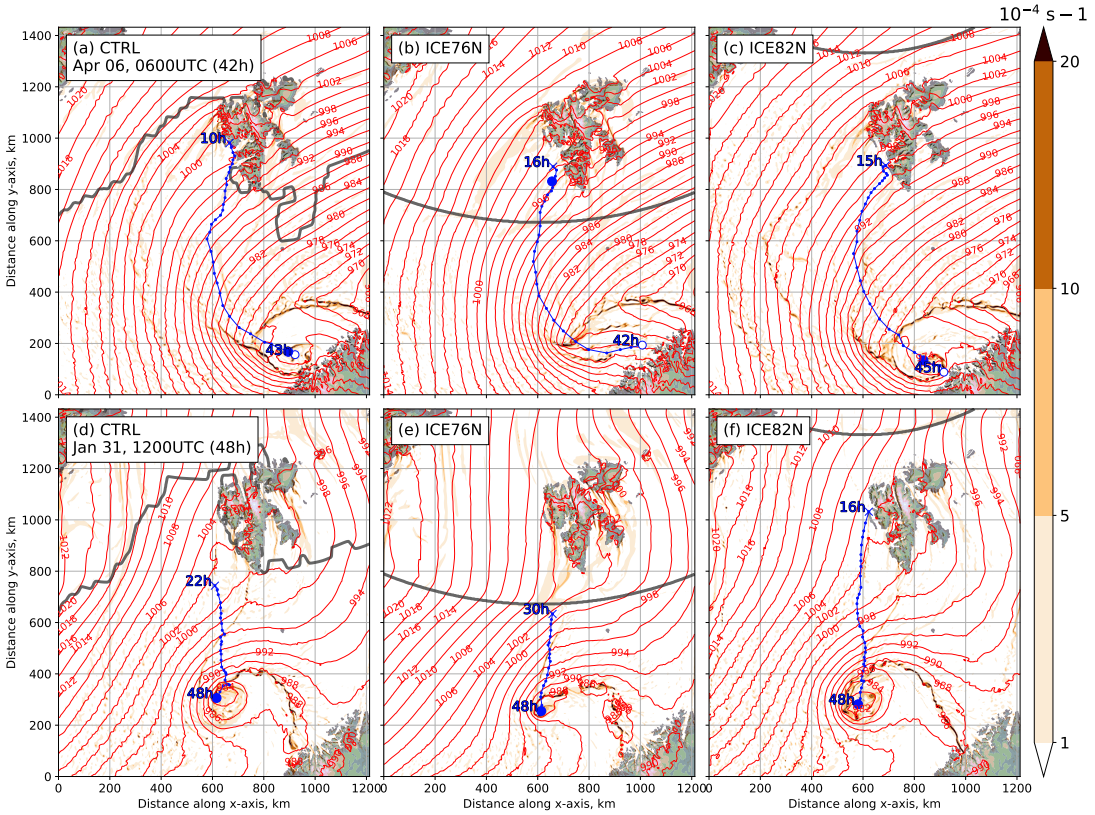

FIGURE 3.9: As in Fig. 3.7, but for (a, d) CTRL, (b, e) ICE76N, and (c, f) ICE82N sensitivity runs of the STARS-72 (top row) and the STARS-77 (bottom row) cases.

In STARS-77 (Fig. 3.9e), despite the fact that in this simulation the mesoscale vortices develop in the same spot as in the CTRL run, they appear as a series of small-scale shear waves without a dominant centre (the SLP minimum is around 4 hPa weaker than the CTRL). The growth of this mesoscale disturbance is hindered by the lack of surface heat fluxes. Similarly to the NOSVA run, the link to Svalbard is very weak, and it is only due to the vorticity source at the synoptic low periphery that the mesoscale vortices develop at all.

In the retreated sea ice conditions (ICE82N), both PLs undergo a life cycle similar to that of the CTRL run and exhibit almost the same vorticity pattern and development. In the STARS-72 case, the mesoscale cyclone is comparable to the CTRL run when expressed in vorticity (Fig. 3.8a), surface wind speed, or precipitation rate, although the maximum value of averaged vorticity is slightly smaller than in CTRL. A possible explanation is that the sensible heat flux is also lower during the early states of the PL life cycle, though not as low as in the ICE76N case. In the STARS-77 case the mesoscale cyclone is slightly stronger in the ICE82N run compared to CTRL, based on the mean low-level vorticity (Fig. 3.8b) and precipitation rate. However, even though the sensible heat flux is lower during the PL intensification in the ICE82N run (Fig. 3.8d), the resulting decrease in the vorticity is small. On the other hand, in the STARS-77 case,

the vorticity increase appears quite large, compared to the small increase in sensible heat flux early in the life cycle (Fig. 3.8d).

In short, the impact of replacing the ocean surface with sea ice in the area west of Svalbard (ICE76N) has a greater effect on the intensity of these PLs than changing the sea ice distribution to the north of it (ICE82N).

3.4 Discussion

In these two cases the primary influence of Svalbard is that it blocks the propagation of a CAO: in experiments with flattened elevation mesoscale cyclones still form but they are more readily swept away by the northerly flow, while a doubled elevation deflects the cyclone track (as in the STARS-72 case) or slows it down (STARS-77).

A useful metric for assessing the flow response to orographic obstacles is the non-dimensional mountain height, $\hat{h} = \frac{Nh}{U}$. The real atmospheric flow around complex topography is characterised by large variations in the wind speed U and the Brunt-Väisälä frequency N, making it non-trivial to calculate the average $\hat{h}$ (Ólafsson and Bougeault, 1997). Following estimates of the non-dimensional height in real cases with flow splitting (Ólafsson and Bougeault, 1997, and references therein), we obtain N and U in the layer below the mountain-top level and average them separately (rather than averaging their ratio N/U). This calculation is performed for the CTRL experiment of both PL cases using the model output linearly interpolated to 12 equally spaced height levels below 1200 m. The latter is chosen as the mountain-top level h, being roughly equal to the altitude of the highest peak of Svalbard as represented in the MetUM's surface elevation field, and similar to 916 m in a study by Skeie and Grønås (2000). The area used for horizontal averaging is located upwind of the archipelago, approximately at a distance equal to the Rossby radius of deformation (Elvidge et al., 2015b), $\lambda_R = Nh/f$ (where f is the Coriolis parameter).

The time series of U and N (Fig. 3.10) demonstrate that the upstream conditions are characterised by stable stratification, with values of N close to ones used by Skeie and Grønås (2000) in their idealised experiments. The average wind velocity is quite low in the first 12–18 h of the STARS-72 case simulation (Fig. 3.10a), resulting in $\hat{h}$ up to ≈ 5. Gradually, the wind speed in the lower troposphere increases, due to the strengthening of the large-scale pressure gradient (see e.g. Fig. 3.2b,c), while N remains constant. Consequently, $\hat{h}$ diminishes, but nevertheless remains larger than unity. In the STARS-77 case (Fig. 3.10b), even though U is relatively high, the static stability is large too, so $\hat{h}$ stays larger than ≈ 2 throughout the simulation and increases towards the end. Interestingly, several hours before the formation of the STARS-77 PL, there is a noticeable rise in $\hat{h}$, which may hint at the causality between flow splitting and mesoscale cyclone generation downstream.

These estimates of the non-dimensional mountain height indicate that in both cases the atmospheric flow is incapable of climbing the orographic barrier of Svalbard and thus a flow splitting regime is favoured. Flow splitting is somewhat visible in the wind speed vectors in Fig. 3.3, while the wake convergence is also demonstrated by the pattern of backward trajectories (Fig. 3.5e). As demonstrated theoretically by Smith (1989b) and numerically by Skeie and Grønås (2000), blocking in experiments with realistic orography is more pronounced than in experiments with an idealised mountain, and this can be attributed to the cross-flow oriented mountain ridges of North Spitsbergen. The sufficient non-dimensional height of Svalbard in our cases offers a comparison e.g. with the Sikhote-Alin mountain range, which blocks Siberian cold air masses from the Sea of Japan and creates favourable conditions for mesoscale cyclogenesis (Watanabe et al., 2017).

Under conditions of stable stratification and weak winds flow splitting leads to wake effects such as eddy shedding manifested by PV anomalies on the flanks of an orographic obstacle (Schär and Smith, 1993a; Smith, 1989a; Petersen et al., 2003). The presence of these PV anomalies renders the flow susceptible to barotropic instabilities, as was previously demonstrated by idealised experiments with a circular obstacle (e.g., Schär and Smith, 1993b). This process of low-level vorticity production is likely to be the case in the two PL cases presented here.

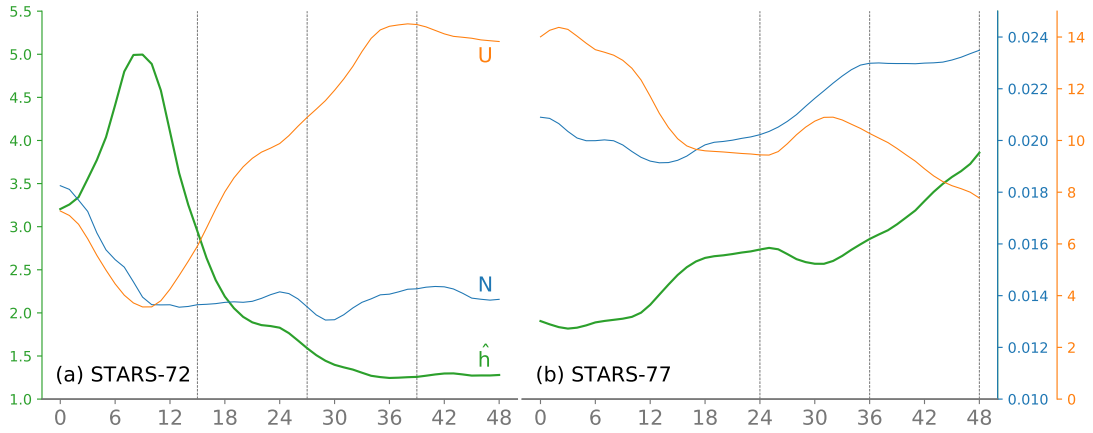

FIGURE 3.10: Time series of the non-dimensional height $\hat{h}$ (green curves), wind speed U ($\mathrm{m\,s^{-1}}$, orange curves) and the Brunt-Väisälä frequency N ($\mathrm{s^{-1}}$, blue curves) in (a) STARS-72 case and (b) STARS-77 case. Vertical lines in (a) and (b) correspond to three time slices shown in Fig. 3.1, 3.2, and 3.3.

Svalbard's isolated shape and orientation make it a source of vorticity filaments, which merge into and reinforce vortices downstream. With removed Svalbard, the STARS-72 PL instead grows on the vorticity clusters coming from the Barents Sea, and the STARS-77 PL lacks a vorticity 'tail' stretching away from Svalbard. Hence, at least for the mesoscale cyclones similar to STARS-72 and 77, Svalbard plays the role of a secondary vorticity source, and not a necessary one for PL intensification.

As for the main vorticity clusters, they form in the rear part of the large-scale cyclone independent of surface conditions near Svalbard (in both PL cases). This southern cluster of vorticity in the central Norwegian Sea emerges at about 23–26 h and intensifies into a shear line. The growth of the shear line is coincident with a high precipitation rate (not shown). This suggests that the latent heat released in the lower troposphere through condensation contributes to PL growth via strong updraughts leading to the stretching of vertical vorticity.

One phenomenological difference between STARS-72 and STARS-77 is the presence of an upper-level PV anomaly. This is illustrated in the SVA200 runs, in which even with higher Svalbard the STARS-72 PL stays on a similar course. The positive PV anomaly is indeed a salient synoptic feature of PL development in cases similar to STARS-72 and is manifested as a short-wave trough in the upper troposphere. Note the shape and magnitude of the upper-level PV filament is very similar to the PV anomaly associated with a Kara Sea PL, analysed by Verezemskaya and Stepanenko (2016). To test whether the upper-level PV anomaly is strong enough to interact with the low-level mesoscale vortices appearing in the CTRL simulation of the STARS-72 case, we calculate the Rossby penetration depth (Adakudlu and Barstad, 2011), which can be approximated by

$$\delta z \approx \frac{L\sqrt{f(f+\zeta_\theta)}}{N},$$

where L is the horizontal scale of the PV anomaly and ζ_θ is the isentropic relative vorticity. At the time of vigorous PL development (at 1500 UTC on 5 April 2007, Fig. 3.2b), PV reaches almost 5 PVU and is located close to the 285 K isentropic surface. As can be seen in Fig. 3.2b and 3.11, the horizontal scale of the anomaly is roughly 200 km. The relative vorticity ($\zeta_{\theta=285\,\mathrm{K}}$) contribution to the PV anomaly on this level is about $2.5 \times 10^{-4}\,\mathrm{s}^{-1}$, or $\approx 1.8f$, and $N = 0.0092\,\mathrm{s}^{-1}$ in the tropospheric column around the PL centre. Using these values, we obtain a Rossby penetration depth of ≈4.8 km, which exceeds the vertical distance between the low-level and upper-level PV anomalies. This suggests that one of the mechanisms of the PL development is a dynamical coupling between the low-level disturbance and the upper-level trough.

In the STARS-77 environment, even though the average Brunt-Väisälä frequency is of the same magnitude, the PV field does not have a distinct positive anomaly in the upper troposphere, nor does isentropic relative vorticity, so a dynamical coupling does not appear to be occurring.

One might expect that with a weakened temperature stratification in the ICE82N experiment of the STARS-72 case, the vertical PV coupling would be stronger and lead to a more intense PL. However, as seen from Fig. 3.8a, the mesoscale cyclone in the STARS-72 case appears slightly weaker compared to the CTRL run. A possible explanation is that in the run with reduced sea ice, the surface heat fluxes are persistently lower, because the convective boundary layer of the northerly flow is more

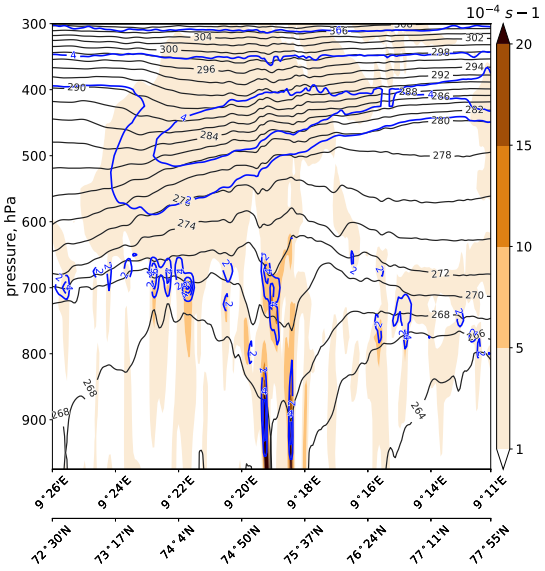

FIGURE 3.11: South-to-north vertical cross-section of relative vorticity (colour shading, $10^{-4}\,s^{-1}$), potential temperature (black contours, every 1 K), and potential vorticity (blue contours, every 2 PVU) at 1500 UTC 5 April 2007 in the CTRL simulation of the STARS-72 case. The location of the cross-section is given in Fig. 3.2b.

well-mixed, reducing the air-sea temperature difference. In ICE76N the presence of sea ice implies that vortices spawned by Svalbard's orography do not gain sufficient strength and dissipate or make landfall.

The cumulative effect of surface fluxes on both PLs is evident from the comparison of the areas under the curves in Fig. 3.8c,d. Even though the total area integrated for the CTRL and ICE76N curves is similar, the heat flux at the beginning of the PL's life cycles is significantly lower in ICE76N than in CTRL. Hence, even though the PLs' development depends on a mix of barotropic and baroclinic processes, surface heat fluxes are still important in their early stages. It appears that in the STARS-72 case, surface fluxes are more important in the very beginning of the PL development than later on.

3.5 Summary and conclusions

We have carried out numerical simulations of two Norwegian Sea PLs, in which the orography of Svalbard and the sea ice around it were modified to test their role in mesoscale cyclone formation and development. Our focus is on the Norwegian and Barents seas area, but these results have implications for PL dynamics more generally. We use a state-of-the-art convection-permitting numerical weather prediction (NWP) model that allows for a detailed examination of PL life cycles in the control experiments and how their tracks and intensity change in perturbed scenarios.

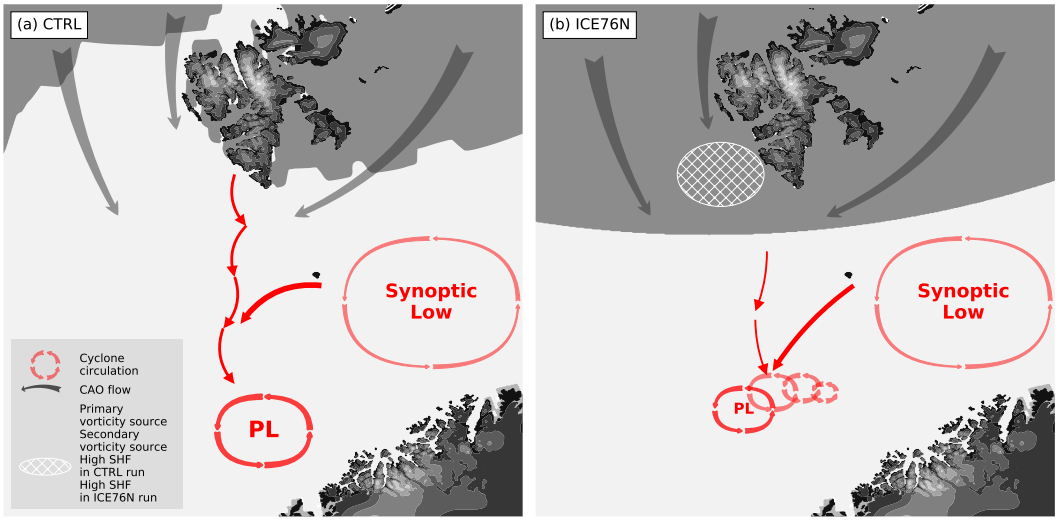

FIGURE 3.12: Schematic representation of mesoscale cyclone generation typical for cases like STARS-72 and STARS-77. Dark grey arrows depict CAO flow curving around Svalbard. The primary source of vorticity for these PLs is on the north-western periphery of a synoptic-scale cyclone, while the secondary source is located to the west of Svalbard (shown by hatching). The movement of vorticity clusters and their merger into a PL is shown by red arrows. (a) The CTRL simulation. (b) The ICE76N experiment with the sea ice extended to the south, which shows an area with strong sensible heat flux (SHF, cross-hatched), which is a (delayed) source of energy for the development of the weaker PLs (shown by smaller red circulations). The high sensible heat flux area in the CTRL experiment is shown in (b) by white cross-hatching.

Due to a large non-dimensional mountain height, Svalbard splits the northerly CAO and produces low-level vorticity filaments that grow to mesoscale cyclones with the help of surface heat fluxes. In the synoptic conditions characterised by the large-scale depression over Northern Norway and an anticyclone over Greenland, vorticity filaments emanating from Svalbard need to merge with their counterparts coming from the Barents Sea to form intense PLs, as seen here for both the STARS-72 and STARS-77 cases. In other words, the primary sources are convectively-driven convergence lines, while Svalbard's mountains provide a secondary source of vorticity (Fig. 3.12a). Increasing Svalbard's orography leads to greater vorticity production in the early stages of PL development, as well as deflection of PL tracks. In cases with a prominent upper-level PV anomaly (such as STARS-72) the PL is steered by the cold trough aloft and is less affected by the topographic forcing.

The removal of the sea ice to the east of Svalbard and in the Fram Strait results in a moderate intensification of the more convectively driven PL (STARS-77). On the other hand, extending the sea ice cover to the south (Fig. 3.12b) deprives the mesoscale vortices of a necessary heat supply, halting their intensification (STARS-72) or slowing it down (STARS-77). PL development is hindered in this situation, because weaker surface fluxes (see Fig. 3.8c,d) lead to a more stable stratification and less condensational heating.

The two cases analysed in our study exemplify that PLs in the North-East Atlantic often begin their evolution from sporadic vorticity filaments and clusters associated with convective cells. Vorticity clusters form in surges at the western part of large-scale depressions, and some of them intensify to PLs with gale-force winds. These two mesoscale cyclones withstand large perturbations to their ambient environment and still develop to sufficient intensity to be labelled as PLs. Thus we demonstrate that both Svalbard's orography and surrounding sea ice have an impact on the cyclogenesis in the Norwegian sea to the point of *modulating* it, but not being a dominant factor.

A next step would be extend our study to more PL cases and examine if these results are robust for different synoptic situations. Creating a climatology of mesoscale vortices in the vicinity of Svalbard will allow for broader conclusions about the statistically significant influence of orography and sea ice on PL genesis. A possible follow-up study on a climatological scale could involve calculating the non-dimensional height upstream of Svalbard and correlating its values with PL formation in the Norwegian Sea.

4

Climatology of polar mesoscale cyclones in the Nordic Seas

4.1 Introduction

4.1.1 Polar mesoscale cyclone climatological studies

Climatological studies of polar lows (PLs), and more generally, polar mesoscale cyclones (PMCs), are important for a comprehensive understanding of their interannual variability, geographical distribution, and the weather regimes favourable for their development.

With the advent of the satellite era, initial climatological surveys of PMCs were conducted. One of the first PMC climatologies was compiled by Wilhelmsen (1985) for the Nordic Seas region and covered the period between 1972 and 1982. For the same region, albeit for the period two decades later (2002–2011), a database of PLs based on subjective analysis of satellite observations has been developed by forecasters at the Norwegian Meteorological Institute (Noer et al., 2011). Satellite-based climatologies of PMCs have been derived for other regions such as the North Pacific (Yarnal and Henderson, 1989), the Gulf of Alaska (Businger, 1987), the Eurasian Arctic (Zabolotskikh et al., 2016), the Southern Ocean (Verezemskaya et al., 2017). With more and more different satellite products available, e.g. synthetic aperture radar (SAR) imagery (Furevik et al., 2015) and CloudSat radar (see Chapter 2), the use of satellite data for mesoscale cyclone climatologies is increasingly beneficial due to their generally higher spatial resolution, as compared to global reanalyses or climate model output (Verezemskaya et al., 2017). On the other hand, satellite data presents other challenges

such as irregular or poor time frequency of image retrievals, limited dataset duration, and inconsistencies in observations. More importantly, the subjective nature of PMC identification in satellite images makes the climatologies questionable and difficult to compare to each other.

The use of global atmospheric reanalyses circumvent the problem of observational inconsistencies and the subjectivity of satellite-derived climatologies. In a pioneering study, Condron et al. (2006) compared the 2-year satellite climatology of Harold et al. (1999a) to automatically detected PMCs in 40-year European Centre for Medium-Range Weather Forecasts (ECMWF) Re-Analysis (ERA-40). They found a large bias in the size of cyclones detected in the Northeast Atlantic. Although up to 80 % of cyclones with diameters larger than 500 km are identified in the sea level pressure (SLP) field, the detection rate drops to 20 % for 100-km-scale cyclones. This is perhaps unsurprising, since ERA-40 has a resolution of 1.25° in the horizontal and 6 h in time — quite coarse for representing mesoscale weather systems. These results were confirmed by Laffineur et al. (2014), who looked at the representation of 29 Sea Surface Temperature and Altimeter Synergy for Improved Forecasting of Polar Lows (STARS) PLs in two ECMWF reanalyses. Only 6 PLs were found in ERA-40, while the newer ERA-Interim reanalysis showed a considerable improvement: 13 out of 29 could be identified in its SLP data. Downscaling ERA-Interim with a high-resolution limited area model further improved the detection rate.

Based on objective constraints of relative vorticity, surface wind speed and static stability, Zappa et al. (2014) demonstrated that more than half (56 %, 19 out of 34) of STARS cyclones can be detected in the ERA-Interim data over a period of three years. Using the same reanalysis, but a different tracking method, Michel et al. (2018) obtained a similar detection rate (60 %), while in the study by Stoll et al. (2018) the rate is ≈79 %. Moving to higher horizontal resolution, it was found that up to 70 % of STARS PLs can be detected in the ECMWF operational analysis (Zappa et al., 2014). The recently developed Arctic System Reanalysis (ASR) based on a high-resolution non-hydrostatic model with improved data assimilation opens new opportunities for cyclone climatologies (Tilinina et al., 2014). It has already been proven advantageous in PL studies: Smirnova and Golubkin (2017) show that it allows for detection of up to ≈89 % of STARS cyclones, while the hit rate obtained by Stoll et al. (2018) is slightly lower but very close (85 %). The latter two studies indicate a significant improvement of ASR over ERA-Interim in representing mesoscale cyclones in the Arctic. Moreover, compared to ERA-Interim downscaled to the grid spacing of 12 km (Laffineur et al., 2014) and operational ECMWF reanalysis (Zappa et al., 2014), ASR still has a higher number of STARS PLs. This can be explained by different model physics and a non-hydrostatic dynamical core in Weather Research and Forecasting Model (WRF) used for ASR. However, the main disadvantages of this reanalysis are its limited spatial coverage and a relatively short time span (2000–2012).

In fact, the short time span is a common weakness of PMC statistical studies, besides the horizontal grid spacing of the atmospheric data (as well as the chronic lack of observations in the polar regions). A lot of PMC climatologies are based on just a few years worth of data: such as 2 years (e.g. Harold et al., 1999a; Blechschmidt et al., 2009), 3 winters (e.g. Laffineur et al., 2014; Zappa et al., 2014), or 6 winters (e.g. Watanabe et al., 2016); making the robustness of their results debatable.

Fortunately, a number of recent reanalysis-based climatologies span more than one decade. For example, Yanase et al. (2016) used the Japanese Re-Analysis (JRA-55) and applied the same tracking algorithm as Zappa et al. (2014) to detect PLs in the Japan Sea over the period of 1979–2015. While confirming the earlier case studies about the importance of upper-level cold troughs for PL development, they found that PLs have two dominant directions of propagation, reflecting the difference in planetary- and synoptic-scale conditions. Another long-term climatology (Mallet et al., 2013) also focused on the prevailing weather regimes during a PL formation, based on the ERA-Interim data (1979-2011) extended back in time using the NCEP/NCAR reanalysis (1948-1979). In their study, the majority of Norwegian and Barents Seas PLs were found to occur during the Atlantic Ridge regime, and slightly less during the negative phase of the North Atlantic Oscillation.

Instead of categorising mesoscale cyclones by the large-scale circulation patterns, some studies concentrate on the dynamical method of classification. Terpstra et al. (2016) looked at the atmospheric properties of forward- and reverse-shear PLs within the STARS database. They demonstrated that reverse-shear cyclones were neglected in previous PL classifications, yet they commonly occur during cold air outbreak (CAO) events in the Nordic Seas. The composite analysis in their study revealed the dependence of the criteria commonly used to define PLs on the shear conditions during their development.

With the help of MetUM simulations, Bracegirdle and Gray (2008) analysed baroclinicity and stability criteria for PL events in the North Atlantic and categorised them according to the Petterssen and Smebye (A, B, and C) types of cyclone evolution. The cyclonic features are identified mostly along fronts, the rationale being to capture incipient frontal waves. Consequently, their study includes a large number of weak features. The spatiotemporal distribution of PL occurrence was found to be broadly similar to other climatologies, except for a maximum in the Barents Sea, whose absence in previous studies is attributed to the lack of observations in the area. Bracegirdle and Gray (2008) also found that about one-third of the objectively identified PL events in the Nordic Seas have atmospheric conditions associated with the type C cyclones, namely strong latent heating and weak low-level baroclinicity. The C-type PLs were found to dominate the southern Norwegian Sea.

Several other researchers have employed global and regional model output to create mesoscale cyclone climatologies. Zahn et al. (2008) created the first multidecadal

PL statistic for the North Atlantic sector from 1948 to 2006 by downscaling the global NCEP/NCAR reanalysis with a regional climate model with horizontal grid spacing of 0.44°. Their results show little decadal variability and no significant long-term changes in PL occurrences, although in a follow up study based on a future climate simulation, Zahn and Storch (2010) predict a decrease in a PL activity and its shift to the north. Similar results have been obtained by Romero and Emanuel (2017) using Coupled Model Intercomparison Project phase 5 (CMIP5) output. One of the advantages of the climate model approach is its freedom from the time constraints of reanalyses or observations. However, it comes with the same problem of correctly identifying PMCs in the atmospheric data. For example, Zahn and Storch (2008) and Zahn and Storch (2010) required a southward propagation of PL, thereby limiting their ability to detect PLs that develop in forward-shear conditions (Terpstra et al., 2016). Rojo et al. (2015) also report that a number of PLs propagating northward in the Nordic Seas is about one fifth and cannot be ignored.

4.1.2 Criteria for polar mesoscale cyclone identification

PMCs develop over the ocean and quickly dissipate upon landfall. Thus a common requirement for their identification is that they exist (e.g. Zappa et al., 2014) or at least form (e.g. Michel et al., 2018) over open water.

Following the classic definition given by Rasmussen and Turner (2003), a threshold of 15 $\mathrm{m\,s^{-1}}$ surface wind speed is commonly used to identify PLs (e.g. Yanase et al., 2016). However, this threshold is likely to produce biased results, because the near-surface wind speed is known to be underestimated in coarse-resolution reanalyses (e.g. Moore et al., 2015b). Reanalyses with finer grid spacing, e.g. ASR, have more realistic wind speeds (Bromwich et al., 2016; Smirnova and Golubkin, 2017). Still, defining a strict threshold for only one meteorological quantity cannot take into account the full spectrum of situations associated with PL development (e.g. if it is embedded in a strong CAO).

Besides the wind speed threshold, different static stability criteria are frequently used to detect or classify PMCs, addressing the general agreement within the scientific community that marine CAOs are usually precursors of PL development. One of the most common criteria is a difference between the sea surface temperature (SST) and the air temperature at 500 hPa, SST-T_{500}, (e.g. Zahn and Storch, 2008; Zappa et al., 2014, also see Ch. 3). The threshold of this difference is usually set to 43 K, but recent studies claim that this discards a considerable number of PL, mostly those forming in the forward-shear environment (Terpstra et al., 2016; Smirnova and Golubkin, 2017). Bracegirdle and Gray (2008) were the first to objectively compare different static stability parameters and found that the difference between the wet-bulb potential temperature at 700 hPa and SST is most effective at separating PL from other cyclones.

The recent study by Stoll et al. (2018) greatly extended the investigation into the efficacy of PL identification parameters. They used the same objective tracking method as Zappa et al. (2014), and applied it both to ERA-Interim and ASR reanalyses and compared the results to the STARS database. The three most effective criteria for separating PLs from other extra-tropical cyclones were found to be 1) the difference between SLP at the centre of the low and its surroundings, 2) the difference in the potential temperature between the sea surface and the 500 hPa level, and 3) the tropopause wind speed poleward of the cyclone. It is promising that results derived from both reanalyses agree on what parameters are the most effective (Stoll et al., 2018). However, this study's major weakness is the focus on the STARS cyclones, which skews their conclusions towards relatively large and intense Nordic Sea type PLs. In other words, training the detection metrics on a small dataset of PLs in one region and applying the same precise thresholds for other regions is arguable; so the conclusions about their global climatology of PLs should be treated with caution.

In the present study, the selection of PMCs from the full subset of cyclone tracks is based on more simple metrics (Sec. 4.3.5), following e.g. Watanabe et al. (2016) and Michel et al. (2018).

4.1.3 Objective algorithms for polar mesoscale cyclone tracking

Although a lot of the climatologies discussed above were compiled from manually-tracked mesoscale cyclones (e.g. STARS), several studies utilise objective detection and tracking algorithms, which came to the PL community mostly from mid-latitude cyclone tracking research. Various methods have been used for objective PMC tracking; they can be broadly divided into two groups: those associating PMCs with local minima of SLP (e.g. Zahn and Storch, 2008; Michel et al., 2018) and those tracking PMCs by local extrema in the relative vorticity (e.g. Condron et al., 2006; Zappa et al., 2014; Watanabe et al., 2016; Stoll et al., 2018). One of the advantages of using vorticity is that it is less influenced by the background flow and allows systems to be identified much earlier in their life cycle (Hoskins and Hodges, 2002).

There is a need for a large inter-comparison project to define what meteorological field is better for PMC tracking. The first attempt at such a comparison was made by Xia et al. (2012) who found significant differences in number of tracks derived from the SLP fields filtered by two different spatial filters. Meanwhile, for extra-tropical cyclones in general, Neu et al. (2013) found little evidence for statistical difference between the algorithms based on SLP and vorticity. It should be noted, that the identification of cyclones in SLP field is biased towards large-scale features and slower moving systems, while the vorticity-based tracking is skewed towards smaller spatial scales (Rae et al., 2017). In addition, using either of these fields has drawbacks associated with different interpolation and filtering techniques.

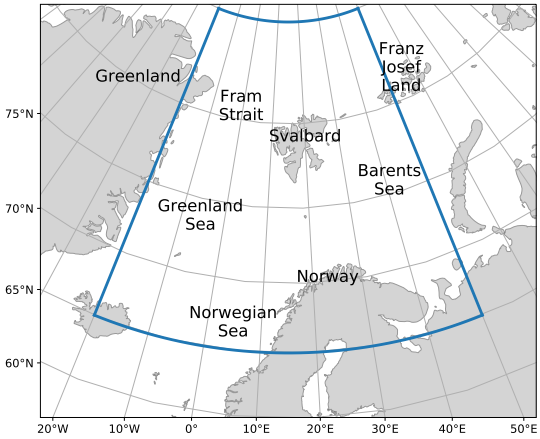

FIGURE 4.1: Domain used for objective PMC tracking.

For the present investigation, we use the low-level relative vorticity field, because the aim is to include not only the largest and most vigorous mesoscale cyclones, but also smaller and weaker vortices, often missed by earlier studies.

4.1.4 Novelties and aims of this study

Notwithstanding the number of studies mentioned above, there is still a gap in the comprehensive climatology of PMCs. Even in the region of their highest activity — the Nordic Seas (Laffineur et al., 2014), there have been only a handful of works based on objective tracking (e.g. Condron et al., 2006; Bracegirdle and Gray, 2008; Zappa et al., 2014; Michel et al., 2018; Stoll et al., 2018). Meanwhile, the Nordic Seas region and the Atlantic sector of the Arctic Ocean (Fig. 4.1) are of great interest: they are located near areas of high off-shore activity and are expected to have increased level of shipping (Melia et al., 2016). Even more importantly, PMCs and associated with them CAOs can have impact on the ocean circulation in the region with implications for the global climate (Condron and Renfrew, 2013).

The present chapter takes advantage of the latest developments made at ECMWF[1] that resulted in a new reanalysis product — ERA5[2]. We expect that it will allow us to detect more PMC and resolve their structure better than other available datasets. As such, our focus is chiefly on small meso-α-scale and large meso-β-scale cyclonic vortices over the Nordic Seas. The aim is to produce a new climatology using the objective tracking algorithm developed by Watanabe et al. (2016) and to prove that ERA5 permits for more successful tracking of these phenomena. In addition, we attempt to

[1]Disclaimer: this chapter contains modified Copernicus Climate Change Service information (2018). Neither the European Commission nor ECMWF is responsible for any use that may be made of the Copernicus Information or Data it contains.

[2]ERA5 is the fifth generation of ECMWF atmospheric reanalyses of the global climate, which started with the FGGE reanalyses produced in the 1980s, followed by ERA-15, ERA-40 and most recently ERA-Interim.

find links between the sea ice cover in the Arctic and the mesoscale cyclone activity in the region.

The remainder of this chapter is organised as follows. In Section 4.2 the reanalysis datasets are described. Section 4.3 describes the tracking algorithm. Its verification against two datasets of observed PMCs is given in Section 4.4. In Section 4.5, the main results are presented, comparing PMC climatologies based on ERA5 and ERA-Interim. Section 4.6 explores the possible linkages between the PMC distribution and Arctic sea ice extent. In Section 4.7, a brief summary of the chapter is given, and possible follow-up work is discussed.

4.2 Data

We use two of the reanalysis products generated by the ECMWF Integrated Forecast System (IFS) model: ERA5 and ERA-Interim. Both reanalyses are generated using a four-dimensional variational data assimilation (4D-Var) scheme. However, they differ substantially in terms of spatiotemporal resolution, model physics, and assimilated observations (see below). The ERA5 product is meant to replace ERA-Interim, but is still in production[3]. Thus in this study, both reanalyses are used only for 9 extended winter seasons when both products overlap: 2008–2009 to 2016–2017. Here, an extended winter season is defined as 1 October – 30 April, which covers the season of PMC activity in the Nordic Seas region (e.g. Harold et al., 1999a; Noer et al., 2011).

4.2.1 ERA5

ERA5 is a time-consistent homogeneous global atmospheric reanalysis generated in near real time. It is based on the cycle `41r2` of the IFS, with 137 hybrid sigma-pressure vertical levels, with the top level at 0.01 hPa (around 80 km). Besides the model levels, atmospheric data are interpolated to 37 pressure levels, which are used here for objective tracking: relative vorticity (`paramId=138`, s^{-1}) at 950 hPa and two horizontal components of wind (`paramId=131` and `paramId=132`, $m\,s^{-1}$) at 8 levels (1000, 975, 950, 925, 900, 850, 800, 700, hPa). One additional variable that is required by the tracking to exclude synoptic-scale systems is the mean SLP (`paramId=151`, hPa).

Temporal and spatial resolution

The ERA5 dataset contains one high resolution realisation (HRES) and a reduced resolution ten member ensemble (EDA). The ensemble output includes information about uncertainties, which is provided at slightly reduced spatiotemporal resolution. This

[3]Complete release of 1979-2008 data is planned for late 2018, and release of 1950-1978 is planned for 2019.

TABLE 4.1: Key differences between ERA5 and ERA-Interim[4]. Note only 2008–2017 years are used here.

	ERA-Interim	ERA5
Period covered	1979–present	1950–present
IFS version	Cycle 31r2 4D-Var	Cycle 41r2 4D-Var
Horizontal resolution	79 km (TL255)	31 km (TL639) for HRES, 62 km for EDA
Vertical resolution	60 levels to 0.1 hPa	137 levels to 0.01 hPa
Temporal resolution	6 h analysis fields; 3 h forecast fields	1 h analysis fields, 3 h for EDA
Uncertainty estimates	None	From a 10-member EDA
Model input	As in operations (inconsistent SST)	Appropriate for climate (CMIP5) forcing
Input observations	As in ERA-40 and from GTS	In addition, various newly reprocessed datasets and recent instruments that could not be ingested in ERA-Interim
Variational bias scheme	Satellite radiances	Also ozone, aircraft and surface pressure data
Number of parameters	≈100	≈240

will allow for a new suite of climatological studies of PMCs based on ensemble composites. In the present investigation, however, only the HRES realisation is used, and this will simply be referred to as 'ERA5' forthwith.

The ERA5 atmospheric data have a triangular truncation TL639, which corresponds to a grid spacing of 31 km (0.28125°). The time frequency of atmospheric parameters is 1 h. The sea ice concentration is updated once a day, so data at 12:00 is used for analysis here.

Advantages over ERA-Interim

Besides higher spatiotemporal resolution, ERA5 has a number of advantages over the ERA-Interim dataset (Table 4.1). For example, the representation of the troposphere has generally improved due to updates of the IFS model and data assimilation. This is manifested in better representation of tropical cyclones, as well as a better global balance of evaporation and precipitation. More importantly, ERA5 has more consistent sea surface temperature and sea ice, which is crucial for mesoscale dynamics in high

[4]Adapted from https://software.ecmwf.int/wiki/pages/viewpage.action?pageId=74764925

latitudes (Spengler et al., 2016). Whether or not it has better representation of PMCs, will be discussed in this chapter.

4.2.2 ERA-Interim

The ERA-Interim (Dee et al., 2011) is an atmospheric reanalysis starting from 1979 and extending up to the present. It is based on the IFS cycle `31r2` run with 60 vertical levels and TL255 spectral resolution, which corresponds to a global grid spacing of about 79 km.

Temporal and spatial resolution

The analysis data are retrieved from ECMWF on a Cartesian grid with $0.5^\circ \times 0.5^\circ$ spacing and 6 h time step. To increase the time resolution to a frequency more appropriate for the short-lived nature of PMCs, data from 3- and 9-hourly forecasts starting at 00:00 and 12:00 UTC are used (Zappa et al., 2014; Stoll et al., 2018).

4.3 Objective tracking algorithm

The objective algorithm of PMC detection and tracking used here was developed by Watanabe et al. (2016) and is implemented following a few technical improvements. The automatic tracking method comprises three parts: identification of vortices at each time step, connection of vortices in consecutive time steps, and exclusion of synoptic-scale disturbances. Originally, the algorithm was based on a method for the detection of convective cells in radar reflectivity scans. One of the major advantages of this algorithm is that it is suitable for identifying PMCs clustered together or embedded in larger synoptic-scale systems.

Parameters used for identification and linking vortices are almost the same as in Watanabe et al. (2017), apart from some minor modifications. First, the running-mean vorticity smoothing function is switched off, because ERA5 and especially ERA-Interim vorticity fields are rather smooth already and have lower spatial resolution than data used in the original study for the Japan Sea ($0.1^\circ \times 0.125^\circ$). Second, a halo of 30 km is applied to the land-sea mask to reduce the number of stationary orographically-produced vorticity maxima. Third, the size threshold for synoptic cyclone exclusion is raised to 90 000 km^2. Fourth, the connection of vortices is made using the size of a vortex rather than its distance. The key steps of the algorithm are briefly described below.

4.3.1 Identification of vortices

The tracking algorithm begins by finding vorticity maxima in the domain along with continuous areas of high vorticity ($\geq \zeta_{min0}$) surrounding them (Fig. 4.2a). This process

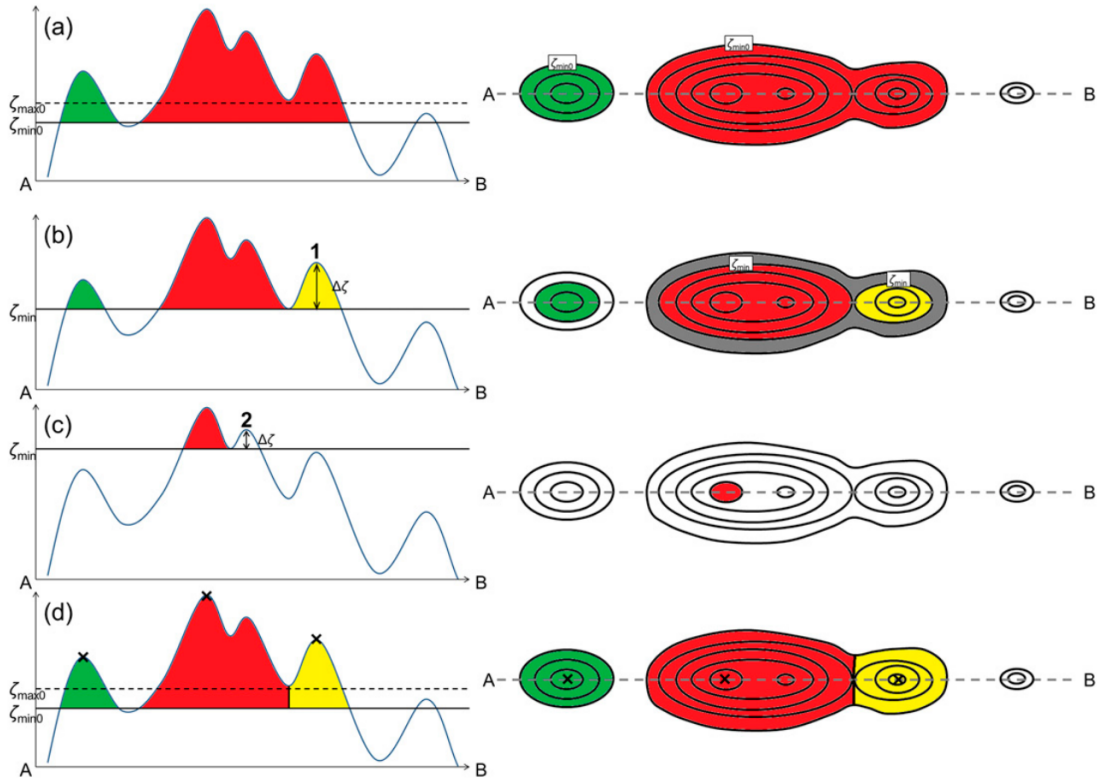

FIGURE 4.2: Steps of the vortex identification algorithm from Watanabe et al. (2016). Panels on the left show the vorticity along the horizontal line A–B, which transects the vorticity field as shown in panels on the right. (a) Original vortex field split into the two areas by ζ_{min0} parameter. (b) An example of a vorticity peak (yellow area, 1) identified as a cyclone. The grey area shows the region where vorticity is lower than ζ_{min} and is distributed to either the yellow and red areas at the last step. (c) An example of the peak (2), identified as a part of the neighbouring vortex. (d) The final step of the identification process. The colours (green, red, yellow) attribute vorticity areas to separate cyclones, whose centres are marked by black crosses.

is continued until all peaks having vorticity $\geq \zeta_{max0}$ are detected, The vortex area is referred to as the 'original vortex area', and it can have one peak ('isolated vortex area', green area in Fig. 4.2a) or several peaks ('multiple vortex area', red area in Fig. 4.2a).

A threshold ζ_{min} is then used to separate vortices in a multiple vortex area by increasing this threshold until the highest peak remains (Figs 4.2b and c). Depending on the difference ($\Delta\zeta$) between the vorticity of the peak ζ_{max} and the threshold ζ_{min}, this part of a vortex area is identified as a separate vortex (yellow area in Fig. 4.2b), or as a part of a neighbouring vortex (second peak in red area in Fig. 4.2b). The threshold for this is defined as $\Delta\zeta_{min} = \gamma \times \zeta_{max}$, where γ is a scale factor, here set to 0.25 (Table 4.2). Finally, the multiple vortex area (shown in grey in Fig. 4.2b) is redistributed to those separate vortex areas whose edge is closest to it. The resulting vortex areas are shown in Fig. 4.2d.

4.3.2 Vortex linking

To connect vortices at consecutive time steps, a first guess of the vortex movement is made based on the steering wind. The steering wind is defined as the horizontal wind averaged within a radius of $r_{steer} = 200$ km between 1000 and 700 hPa (Table 4.2).

The algorithm estimates the next position by assuming that the vortex is advected by the steering wind. The vortex at the next time step must be located within a certain radius ($r_{link} = 120$ km) from this estimated position. If there is more than one vortex in the estimated area, the vortex closest to the estimated position is connected to the previous vortex. If there are no vortices within r_{link}, a second option is considered, namely, if a part of an isolated vortex area overlaps with the estimated area. Again, if there are more than one overlapping regions, the vortex at the previous time step is linked to the vortex having the largest overlap.

If a vortex still does not appear in the vorticity field at the next time step, it is deemed to have dissipated. The track is then terminated at the previous time. In a situation when two or more vortices are connected to the same vortex at the next time step, they are considered to have merged. If a vortex area splits into two, one of them is connected to the original area, while the other becomes a new vortex.

TABLE 4.2: Tracking algorithm configuration used in the CTRL tracking experiment. In the sensitivity tests (Sec. 4.4), one of the parameters is altered while the rest are equal to CTRL values. For explanation, see Sec. 4.3.1–4.3.3.

Parameter	Value
Domain boundaries	65°–85°N, 20°W–50°E
Vorticity peak threshold, ζ_{max0}	2×10^{-4} s^{-1}
Vorticity area threshold, ζ_{min0}	1.5×10^{-4} s^{-1}
Smoothing radius, r_{smooth}	not used
Scale factor, γ	0.25
Steering wind radius, r_{steer}	200 km
Steering wind height	1000–700 hPa
Radius for linking vortices, r_{link}	120 km
Exclusion of synoptic lows	• Vortex area >90 000 km^2, • within 300 km from an SLP minimum
Cold front identification	• Length >400 km, • Bearing angle between $-20°$ and 60°, • Average curvature < 0.1, • Coefficient of determination > 0.8

4.3.3 Exclusion of synoptic-scale disturbances

Unlike a number of cyclone tracking methods (e.g. Hoskins and Hodges, 2002; Neu et al., 2013), the present algorithm does not apply a spatial filter to the vorticity field prior to tracking. Consequently, it must discriminate synoptic-scale cyclones and cold fronts from PMCs based on their size and shape.

A cyclone is classified as synoptic-scale at every time step if the following conditions are satisfied. First, the method checks, if an SLP minimum, which is at least 0.5 hPa lower than the surroundings, is present. Second, if within 300 km from the SLP minimum there is a vortex area larger than 90 000 km^2, the vortex is considered to be a synoptic-scale cyclone. Note that this method is capable of identifying a synoptic-scale low and a PMC embedded within it (Watanabe et al., 2016), as is often observed over the Japan Sea as well as the Nordic Seas.

The shape of the vortex area is used to check for cold fronts. This is done by detecting southern and northern edges of the original vortex area, calculating a distance between them, and the bearing angle between the line connecting them and the north. If certain thresholds of the angle and the distance are exceeded (Table 4.2), the area is further examined for its curvature using quadratic fitting. Upon satisfying the condition of curvature, the vortices in the original vortex area are classified as part of a cold front.

4.3.4 Technical details and latest improvements

The tracking algorithm code is written in the FORTRAN-90 programming language. The code has been upgraded by the author in the following major aspects: time dimension loading, data input, user interface, and version control system.

In order to adapt the code for ECMWF datasets with larger spatial coverage and higher time frequency than the data used by Watanabe et al. (2016), the code has been rewritten so that only one time slice is processed at each iteration, instead of loading all time slices at once. This consumes less memory and permits for longer tracking runs. On the other hand, it has become impractical to check in real time if a cyclone track has duration greater than a given threshold. This is now done at a postprocessing stage (see Sec. 4.3.5).

An input interface based on the netCDF library[5] has been introduced, allowing the algorithm to read data in a common geoscience data format, as well as automatically handle metadata (e.g. dates, domain boundaries, variable names, etc).

The user interface has been improved so that the code does not need to be recompiled every time a user changes a configuration parameter, e.g. the value of vorticity threshold. In addition, the code now depends on the `datetime` FORTRAN library, which makes selecting start and end times significantly more convenient.

[5] https://www.unidata.ucar.edu/software/netcdf/

Besides the changes mentioned above, the code has been refactored and cleared from a few bugs. Options for different FORTRAN compilers (e.g. Intel, GNU, Cray) and HPC platforms (e.g., MONSooN, ARCHER, JASMIN) have been added to the installation script. The code is freely available on GitHub under the MIT license [6].

To accompany the tracking algorithm itself, a software package for postprocessing and analysis has been written in the Python programming language. This package is called `octant`[7] and is available on GitHub[8]. It is used for cyclone track analysis in the subsequent sections. All the code used to create figures for this chapter is also publicly available[9].

4.3.5 Cyclone selection criteria

The statistics presented here are calculated for ERA5 (Fig. 4.3). As mentioned in Sec. 4.1, using strict criteria to select PLs from a set of objectively tracked cyclones has its caveats. To avoid an a priori bias in our results, we keep the criteria to the minimum and thus retain a dataset of not only PLs, but more generally PMCs.

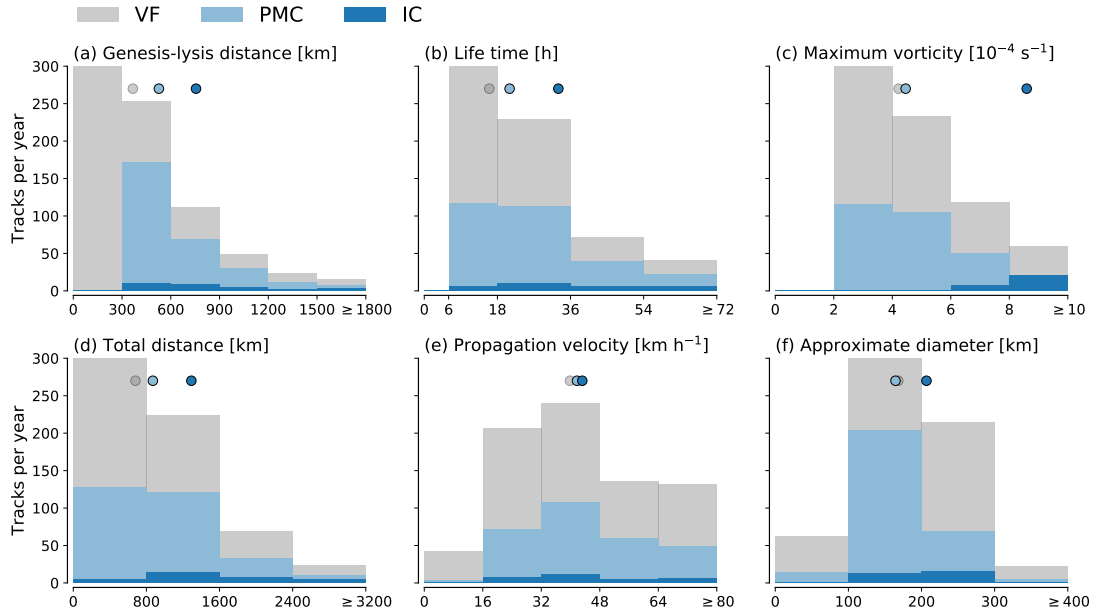

FIGURE 4.3: Histograms of characteristics of vortices grouped by three categories: vorticity features (VF, grey), PMCs (light blue), and ICs (blue). The characteristics shown are: (a) genesis-lysis distance (km), (b) lifetime (h), (c) maximum vorticity ($10^{-4}\,s^{-1}$), (d) total track distance (km), (e) propagation velocity ($km\,h^{-1}$), and (f) approximate diameter (km). Median values of each parameter are shown by circles at the top of the panels with corresponding colours.

[6] https://github.com/dennissergeev/pmctrack
[7] **O**bjective **C**yclone **T**racking **AN**alysis **T**ools
[8] https://github.com/dennissergeev/octant
[9] https://github.com/dennissergeev/pmc_clim

Over the period of 9 extended winters, the tracking method, with the settings listed in Table 4.2, identified 39,936 peaks in the ERA5 vorticity field. Most of them, however, appear for a period of time that is too short, or stay too close to the coastline, in a form of stationary orographic phenomena such as tip jets. Addressing these bogus features, 6,788 vorticity features satisfy the lifetime threshold of >6 h, and spent at least 50 % of their lifetime at least 70 km away from land or domain boundaries. These vorticity features can then be classified as potential PMCs.

To be categorised as PMCs, these vortices must be also flagged as 'mesoscale' by the tracking algorithm (see Sec. 4.3.3 for details) for at least 80 % of their lifetime. In addition, the distance between genesis and lysis (calculated along a great circle) must be greater than 300 km. These conditions are satisfied for 2,610 vorticity maxima. Finally, the top 10 % of PMCs are labelled as intense cyclones (ICs, 261 in total), as inferred from their maximum vorticity. The rest of this chapter is focused on PMCs and its subset, ICs.

The distribution of the features for key track parameters is quite similar for both categories, except for the maximum vorticity distribution, which itself was used to define ICs. The typical distance between the points of formation and dissipation (Fig 4.3a) is close to 500 km for PMCs and almost 800 km for ICs, but can reach 2000 km and more; about half of the vortices that do reach such distances are ICs. In fact, moving to the tails of almost all distributions in Fig 4.3, the ratio of the intense category to all PMCs increases.

The total track distance (Fig 4.3d) distribution is very similar to that of the genesis-lysis distance, but shifted to twice as large numbers. The median distance travelled by PMCs and ICs is roughly 900 km and 1400 km, respectively. Smirnova et al. (2015) report lower values of the total track distance (100–300 km). This discrepancy can be attributed to the irregular time resolution of the satellite data used in their study, as well as the ability of the tracking method used here to identify PMCs for longer time periods.

On average, the lifespan of PMCs is 21 h, and more than half of them last for less than 1 day, in agreement with previous studies (e.g. Rojo et al., 2015). In rare cases ($\approx$10 %) PMC events can have a duration of more than 2 days, and in about 3 % of case, more than 3 days. The intense mesoscale cyclones tend to live 60 % longer than average (Fig 4.3b), and about one tenth of them have lifetimes exceeding 72 h. Note that even though some of PMCs appear to have such longevity, they can undergo changes from e.g. a cold front at the beginning to a mesoscale cyclone to a synoptic-scale low, as long as these changes last for less than one-fifth of their total lifespan, as mentioned above.

The total track distance and the lifetime are used to calculate the average speed of cyclone propagation. These values are very close for both categories (Fig 4.3e), the median values are roughly equal to 40 km h^{-1} (or $\approx$11 m s^{-1}) — similar to the values

reported by Rojo et al. (2015).

An approximate estimation of PMCs's average diameter (Fig 4.3f) demonstrates that these vortices are typically 100–300 km in size, with the intense class being 25 % larger. This estimate is lower than in other PMC climatologies (e.g. Laffineur et al., 2014; Rojo et al., 2015; Smirnova and Golubkin, 2017), but this is likely due to the fact that they report diameters only at mature stage and our data has higher horizontal resolution. More importantly, this is explained by the cut-off we use to exclude synoptic-scale features.

Typically, PMCs attain a maximum of relative vorticity of $4.5 \times 10^{-4}\,\mathrm{s}^{-1}$, which agrees well with Watanabe et al. (2016), who used a different reanalysis for a different region. Recall that ICs are defined by the 90th percentile of this metric, which is equal to $7.54 \times 10^{-4}\,\mathrm{s}^{-1}$. Consequently, the tail of the vorticity distribution is saturated with ICs (Fig 4.3c).

4.4 Verification of the tracking algorithm

The tracking algorithm has been substantially validated by Watanabe et al. (2016) using a list of mesoscale cyclones detected over 6 cold seasons over the Japan Sea and comparing them to subjectively drawn tracks based on the relative vorticity and SLP from the input data, as well as satellite infrared images.

In the present study, we perform an additional verification by counting how many PMCs from the ACCACIA and STARS datasets are identified by the tracking method (for details about the datasets, see the next subsection). The procedure of finding matches between collections of tracks follows the approach of Blender and Schubert (2000). They proposed a non-dimensional distance metric D_{12}, a brief explanation of which is given below. D_{12} fulfils the conditions for a metric by being positive for any different pair and equal to 0 for identical tracks. It is an objective measure of the deviation between two tracks, and it is applicable for cyclone databases defined on different grids and at different temporal resolutions.

Suppose we have two cyclone track datasets (e.g., from satellite imagery and objective tracking output). First, the spatiotemporal distances between all cyclone tracks are estimated. The track of a cyclone in the first dataset is defined as $[x_1(a_1), y_1(a_1), t_1(a_1)]$ with the positions x, y and times t for the time steps $a = 0, ..., A_1$ during the total lifetime A_1. A cyclone track in the second dataset is given by $[x_2(a_2), y_2(a_2), t_2(a_2)]$ and has the lifetime A_2. The spatiotemporal variance spanned by the two tracks is then defined as

$$\sigma_{12}^2 = \frac{1}{A_1 A_2} \int_0^{A_1} \int_0^{A_2} \Big(\alpha \left[(x_1(a_1) - x_2(a_2))^2 + (y_1(a_1) - y_2(a_2))^2 \right] + \beta \left[(t_1(a_1) - t_2(a_2))^2 \right] \Big) da_1 da_2. \tag{4.1}$$

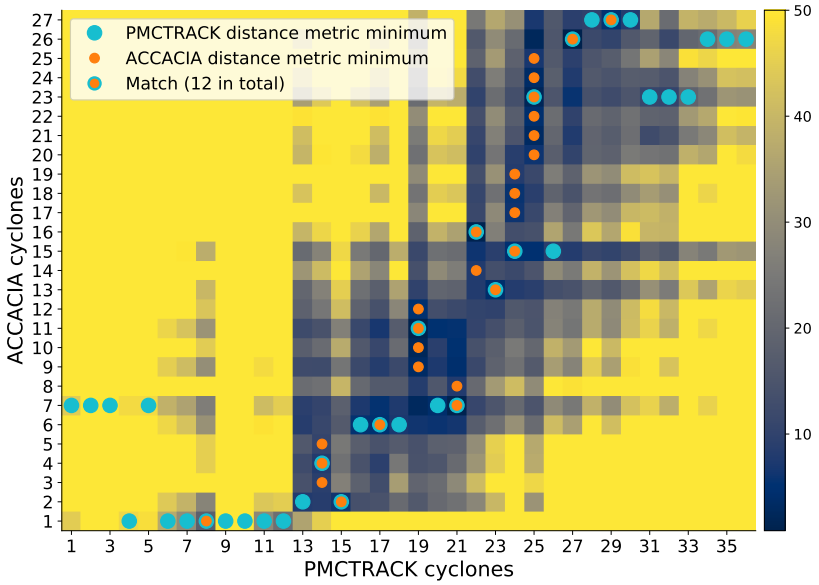

FIGURE 4.4: Example of applying the method of Blender and Schubert (2000) to identify how many ACCACIA tracks are identified by the tracking algorithm. After computing the distance metric D_{12} for every pair of tracks (shown by background colour), minimum values are found for each track in both datasets. Smaller orange circles show minima for ACCACIA tracks (along y-axis), bigger cyan circles show minima for objective tracking results (along x-axis). If they occupy the same grid point, the two tracks are considered a unique pair. In this example, the tracking algorithm is able to find 12 Aerosol-Cloud Coupling And Climate Interactions in the Arctic (ACCACIA) tracks.

The factors α and β are the weights for the spatial and temporal distances. Physically equivalent weights can be obtained by considering typical scales for the distance Δx and time Δt. Assuming a balance between the two sums in Eq. 4.1, we can write

$$\alpha \Delta x^2 = \beta \Delta t^2. \tag{4.2}$$

Their ratio is then equal to the typical speed U squared:

$$\beta / \alpha = U^2. \tag{4.3}$$

In the calculations, we use $U \approx 7\,\mathrm{m\,s^{-1}}$, or $\alpha = 1$ and $\beta = 50$.

The variance σ_{12}^2 does not vanish for two identical tracks, i.e. $\sigma_{11}^2 \neq 0$. Hence, the distance metric is defined as

$$D_{12} = \sqrt{\frac{1}{A_1 A_2}\left[\sigma_{12}^2 - \frac{1}{2}\left(\sigma_{11}^2 + \sigma_{22}^2\right)\right]}, \tag{4.4}$$

where the internal variances are subtracted (σ_{11}^2 and σ_{22}^2 are calculated in the same way, but with identical tracks). The spatial distances are calculated along great circles.

This spatiotemporal distance is then employed to assess the agreement between

sets of tracks. First, for every track i_1 in set 1, the track i_2 with the minimum distance D_{12} is found in set 2. Then, vice versa, the set 2 is scanned and for every track i_2, the nearest track in set 1, i_1 is found. This generates two tables with minimal distances and allows a search for those pairs of tracks that form unique neighbours (Fig. 4.4).

D_{12} has essentially only one free parameter, which controls the importance of spatial proximity versus time overlap between a pair of tracks, and thus is more objective, compared to metrics that have more arbitrary thresholds. This method has been successful in several studies, including in a cyclone tracking algorithm inter-comparison project (Neu et al., 2013).

Another approach for identifying cyclone track pairs is to assume a match if said cyclones stay within a certain radius close to each other for more than half of their lifetime. This has more commonly been used in PMC studies, albeit with slightly different thresholds (e.g. Zappa et al., 2014; Watanabe et al., 2016; Stoll et al., 2018). Even though this method seems more straightforward, it comes with some drawbacks, such as the problem of interpolating tracks to one time resolution. In addition, it includes a number of thresholds, each of which can be a source of bias or subjectivity. After comparing matching rates of the two methods in cases of ACCACIA and STARS datasets (not shown), we conclude that the second method does not bring any obvious advantages over the method of Blender and Schubert (2000).

4.4.1 Verification against the ACCACIA dataset

During the ACCACIA period (≈2 weeks, March–April 2013, see Chapter 2) thermal infrared satellite imagery was subjectively analysed by the author for PMCs. From the cloud patterns, 38 mesoscale cyclones were identified over the Norwegian Sea. After discarding the cyclonic cloud features lasting for less than 6 h, 27 tracks are retained to test the performance of the tracking algorithm.

Vorticity thresholds

First, the tracking is performed with different values of ζ_{max0} (Fig. 4.5a). These test ζ_{max0} thresholds are chosen slightly differently for ERA5 and ERA-Interim: from 1×10^{-4} to $10 \times 10^{-4}\,s^{-1}$ and from 0.2×10^{-4} to $5 \times 10^{-4}\,s^{-1}$, respectively (they overlap for 5 threshold values).

In ERA5, the highest number of ACCACIA PMCs found by the tracking algorithm is 12, three of which are in the IC class. This hit rate is reached when $\zeta_{max0} = 2 \times 10^{-4}\,s^{-1}$, which is the configuration used in the CTRL experiment (Table 4.2). The tracks of all 27 ACCACIA vortices are shown in Fig. 4.5b with the ones successfully identified by the algorithm highlighted. Overall there is no obvious tendency towards longer or shorter tracks, but almost all relatively longer tracks among the 12 found are not categorised as intense cyclones.

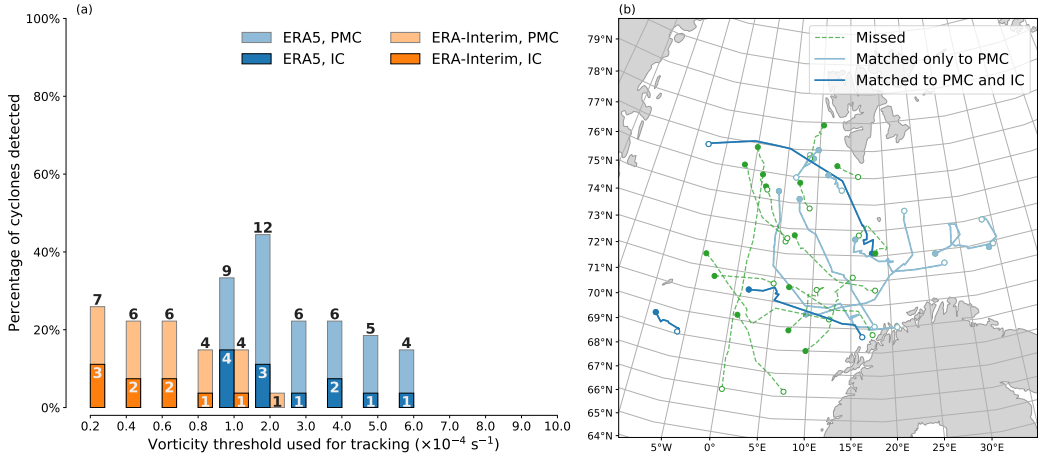

FIGURE 4.5: Verification of the tracking algorithm against the ACCACIA dataset. (a) number of matched PMC and IC pairs in experiments with different vorticity thresholds for ERA5 and ERA-Interim, (b) map of ACCACIA PMC tracks showing which of them are identified or missed in the ERA5 CTRL run.

The higher the vorticity threshold, the fewer ACCACIA tracks have matches in the tracking dataset, with the hit rate dropping to zero at $\zeta_{max0} > 6 \times 10^{-4}\,\mathrm{s}^{-1}$. Interestingly, when the threshold is lower than the CTRL one, the hit rate for ERA5 goes down too. A possible explanation is that with vorticity thresholds too low, several cyclones are treated as one large area of high relative vorticity.

In ERA-Interim, the objective tracking yields consistently lower match rates, reaching 7 at the lowest vorticity threshold and decreasing to 1 at the CTRL threshold ($\zeta_{max0} = 2 \times 10^{-4}\,\mathrm{s}^{-1}$). Up to a third of them are classified as ICs.

Other tracking parameters

Apart from the vorticity threshold, the tracking algorithm's performance has been assessed for runs with other parameters altered within a reasonable range. When compared to the ACCACIA dataset, the tracking results appear to be less sensitive to the settings such as the steering wind radius, the threshold for linking vortices, or the coastal 'halo' (Fig. 4.6). The vertical level of the vorticity field is set to 950 hPa by default (see Sec. 4.3), and appears to be better than the 900 hPa level or, as used in a few other studies (e.g. Zappa et al., 2014), the 850 hPa level.

In this set of experiments, the hit rate is most sensitive to the smoothing: switching it on and setting the smoothing radius to 40–60 km results in about half the number of cyclones being detected compared to in the CTRL set-up.

The relatively poor performance of ERA5 and especially ERA-Interim is due to the fact that cyclonic features comprising the ACCACIA dataset are generally weak and short-lived systems. Another issue is that they have been identified subjectively based

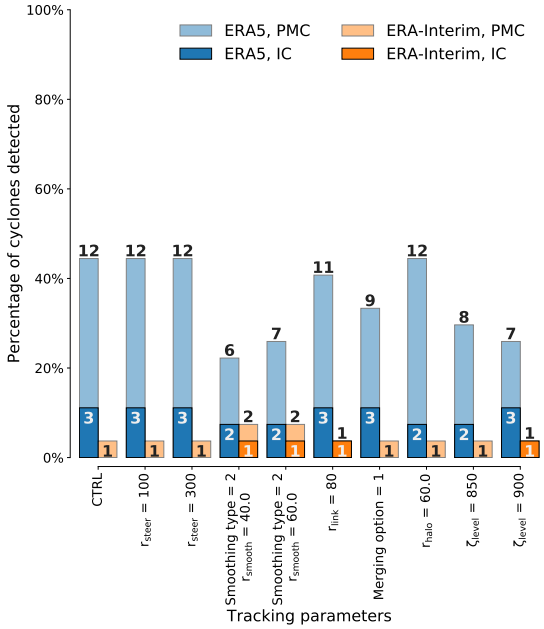

FIGURE 4.6: As in Fig. 4.5a, but for different tracking parameter settings.

on one channel of satellite imagery, so some of them might not be associated with low-level vorticity. Nevertheless, the CTRL configuration of the tracking algorithm is the best even for these small-scale PMCs.

4.4.2 Verification against STARS dataset

The 10-year STARS database (Noer et al., 2011) is the most frequently used record of manually-tracked PLs and is freely available to the community[10]. It provides a list of 185 PL tracks over the Nordic Seas over the period of 2002–2011. The PLs were subjectively identified by forecasters at the Norwegian Meteorological Institute by inspection of satellite infrared data, scatterometer winds and an operational weather forecasting model with convective-permitting resolution.

The STARS dataset has served as a basis for investigation of PL characteristics (e.g. Terpstra et al., 2016) as well as for the evaluation of objective cyclone tracking methods (e.g. Michel et al., 2018). It is important to remember that STARS contains PLs, i.e. the most intense vortices: only the strongest PL is reported when several of them form within the same CAO (Mallet et al., 2013). Thus this dataset is not representative with respect to smaller and weaker mesoscale systems.

In this section, we focus on the PLs that developed over the Norwegian and Barents Seas during three extended winters: October–April of 2008–2009, 2009–2010, and 2010–2011 — the period of overlap between STARS and the current ERA5 release. In total, 52 PL are listed in the database for this period, and 40 of them have the lifetime greater or equal than 6 h.

[10] http://polarlow.met.no/stars-dat

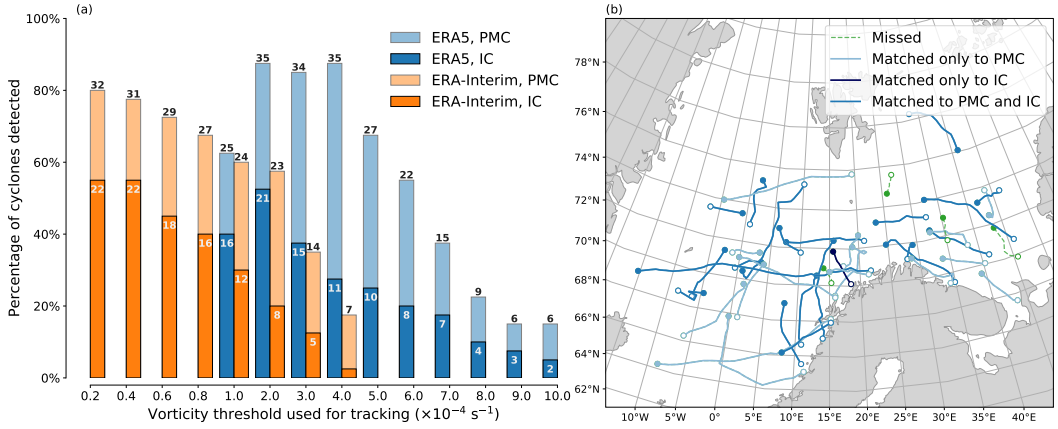

FIGURE 4.7: As in Fig. 4.5, but for the STARS period.

Results of the CTRL experiment (Fig. 4.7) demonstrate that in ERA5 the algorithm is able to pick up to 35 out of 40 STARS PMCs (87.5 %). Two thirds of them reached sufficient intensity to be classified as ICs. As in the previous section, the hit rate decreases substantially with increasing vorticity threshold, dropping below 50 % at $\zeta_{max0} = 7 \times 10^{-4}\,\mathrm{s}^{-1}$. Surprisingly, the proportion of ICs within the PMC subset also falls below 50 % (Fig. 4.7a). Comparing paths of 'hits' and 'misses' (Fig. 4.7b), it becomes evident that lifetime of all of the STARS cyclones missed by the tracking algorithm is at the shorter end of the spectrum. In other words, the tracking algorithm in the CTRL configuration might still miss short-lived PMCs.

The performance of ERA-Interim-based tracking is worse than that of ERA5 (Fig. 4.7a), similarly to the performance for the ACCACIA dataset. The hit rate is 23 out of 40 in the CTRL run, but increases up to 32 out of 40 (80 %) at the lowest ζ_{max0}. The majority of the matched cyclones are categorised as ICs, and the ratio is generally higher than that for ERA5, implying STARS cyclones are associated with high vorticity, but not as high as the top 10 % of the ERA5 vorticity maxima.

The success rate of ERA-Interim tracking is within the range of those obtained in earlier studies. For instance, Zappa et al. (2014) and Stoll et al. (2018) use the vorticity threshold of $2 \times 10^{-5}\,\mathrm{s}^{-1}$ (i.e. the same as the lowest here) and report that 70 % and 79 % of STARS cyclones are matched with objective tracking results, respectively.

Other tracking parameters

Verification against STARS confirms, the sensitivity of our tracking method to other parameters is much lower than the sensitivity to the vorticity threshold (Fig. 4.8).

Even with smoothing of the input vorticity field turned on, the hit rate remains roughly the same both for ERA-Interim and ERA5-based tracking. This is likely because the STARS list is biased towards the strongest PLs, and even with smoothed vorticity field they are detectable at the CTRL value of ζ_{max0}. Proclivity towards more

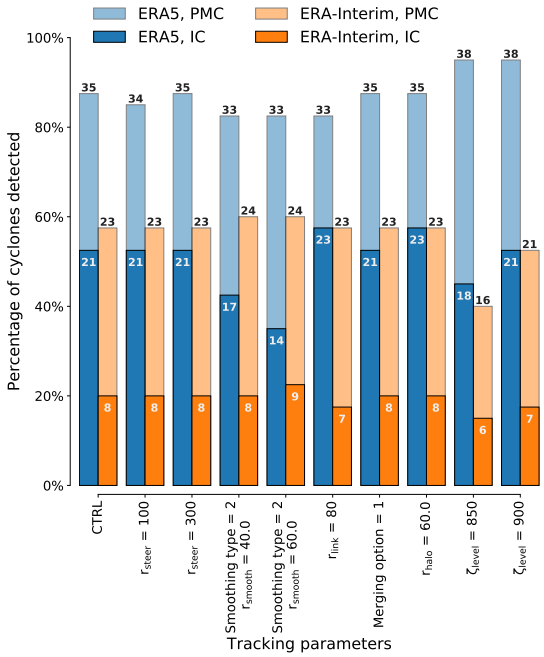

FIGURE 4.8: As in Fig. 4.6, but for the STARS period.

intense (and thus vertically developed) PMCs can also be the reason why selecting a lower pressure for tracking (the last two columns in Fig. 4.8) yields a slightly higher hit rate than average.

Judging from the verification demonstrated in this and the previous subsection, we conclude that the CTRL configuration is suitable for both weak PMCs (like those in the ACCACIA dataset) and intense PL (like those in the STARS dataset). Moreover, the configuration similar to CTRL was used by Watanabe et al. (2016), Watanabe et al. (2017), and Watanabe et al. (2018), allowing for a better comparison of PMC climatologies between the Nordic Seas and the Japan Sea. It will be used in the following sections for both reanalyses, while for ERA-Interim we also detect using a *low vorticity threshold (LVT)* configuration with ζ_{max0} set to $2 \times 10^{-5}\,\mathrm{s}^{-1}$.

4.5 Climatology of PMC in ERA5 and ERA-Interim

4.5.1 Case study

Differences in how ERA5 and ERA-Interim reproduce mesoscale cyclones can be demonstrated using the ACCACIA case, which is analysed in depth in Chapter 2. Note that the dropsonde measurements of the shear line associated with that event were sent to the Global Telecommunication System (GTS) and assimilated by the ECMWF operational model, so the representation of this particular PMC in the reanalysis products is probably better than of other cyclones.

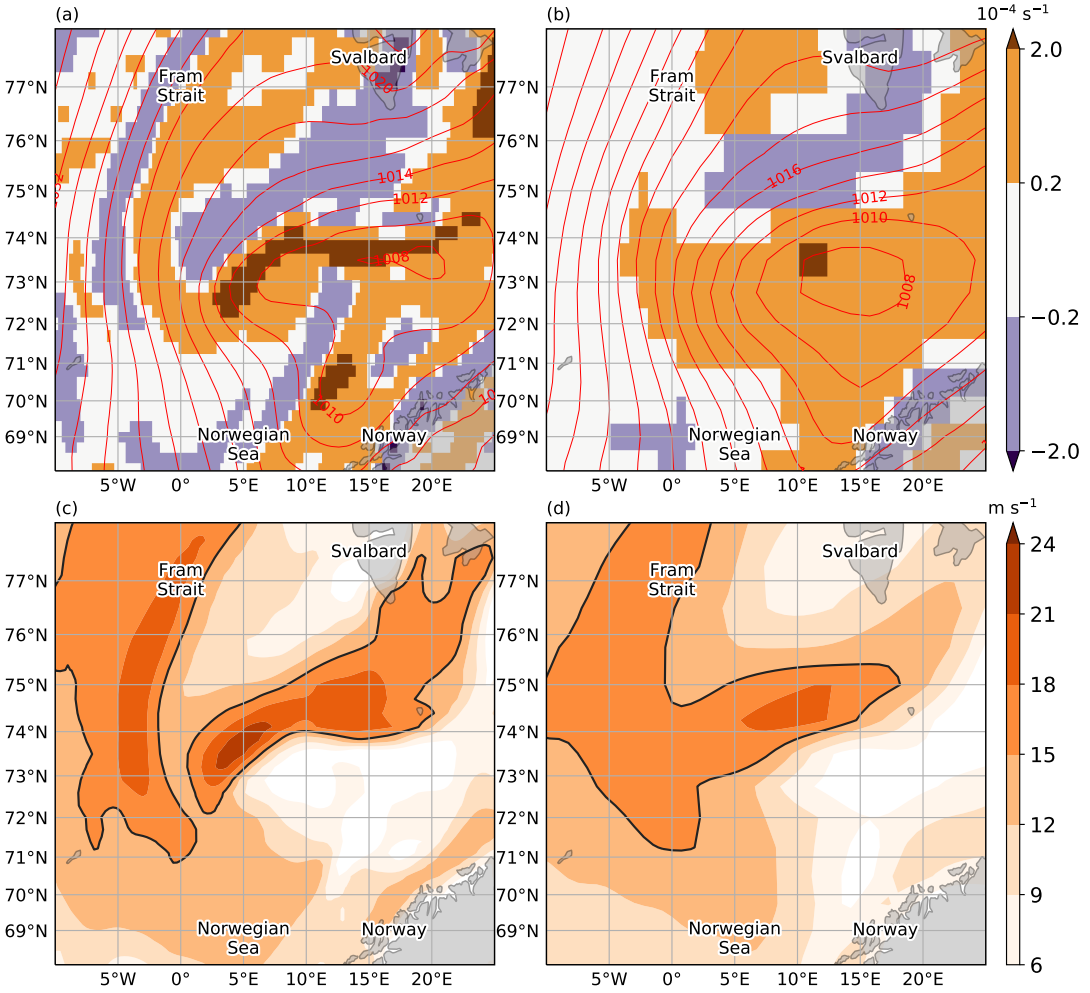

FIGURE 4.9: ACCACIA PMC case as represented in (a, c) ERA5 and (b, d) ERA-Interim at 1200UTC 26 March 2013: (a, b) relative vorticity (shading, $10^{-4}\,s^{-1}$) at 950 hPa level and SLP (red contours, every 2 hPa), (c, d) horizontal wind speed (shading, $m\,s^{-1}$) at 975 hPa level. The $15\,m\,s^{-1}$ isotach is marked by a black contour.

The pattern of ERA5 relative vorticity at 950 hPa, while still having lower values than that simulated by MetUM ($\approx 3.5 \times 10^{-4}\,s^{-1}$ in ERA5 versus $>10 \times 10^{-4}\,s^{-1}$ in MetUM, cf. Fig. 4.9a and Fig. 2.4f), resembles the asymmetric structure of the cyclone, as well as the filaments of vorticity, extending to north east of it. By comparison, in the ERA-Interim the vorticity field has much lower values (Fig. 4.9b), which demonstrates the need for lower vorticity thresholds in the tracking method. It is also hard to distinguish the shear-line PL from the large-scale synoptic flow (Fig. 4.9b). The latter can be inferred from the SLP contours, which have a single minimum in the centre of a large scale cyclone. While the absolute values of pressure minimum is the same, ERA5 resolves much better the 'merry-go-round' pattern of the mesoscale vortices observed during the ACCACIA case (Fig. 4.9a).

The structure of the wind field in the lower troposphere is also reproduced better

in ERA5 than in ERA-Interim (Fig. 4.9c,d). The 'double-winged' structure of the ACCACIA PMC can be seen in more detail in the ERA5 data, including the gap between NW and NE shear lines (see Sec. 2.6.1 for details); ERA-Interim's wind pattern is too smoothed out. In terms of absolute values, the ERA5 horizontal wind speed at 975 hPa (≈300 m) underestimates those observed during the field campaign and simulated by the MetUM model only by about 3–6 m s^{-1} (cf. Fig. 4.9c and Fig. 2.5).

Overall, the structure of this PMC is much more similar to the observed one in ERA5 than in ERA-Interim.

4.5.2 Track-to-track comparison

As mentioned in Sec. 4.3.5, ERA5-based tracking results in 2,610 PMCs in the CTRL run. Since the vorticity fields may differ substantially (see Sec. 4.5.1), the objective tracking yields rather different counts for the ERA-Interim reanalysis, as is already hinted at when verified against STARS and ACCACIA cyclone datasets.

It is important to compare the two reanalysis products in terms of track-to-track agreement, i.e. in a Lagrangian framework (Hoskins and Hodges, 2002). The comparison between ERA5 and ERA-Interim from a Eulerian perspective is presented later using track density maps (Sec. 4.5.4).

Using the same method as in Sec. 4.4, we obtain the number of matching cyclone pairs (N_p) between the ERA5 CTRL run (as a reference set) and ERA-Interim CTRL and LVT runs (test sets). This number N_p, together with the total number of PMC tracks in ERA5 (N_1) and in each of the two ERA-Interim runs (N_2), allows for the calculation of two normalised parameters (Blender and Schubert, 2000).

- The first parameter, a *probability of coincidence*, reveals how many ERA-Interim tracks agree with ERA5 tracks and is given by the ratio of the number of pairs N_p and the number of tracks in ERA-Interim N_2:

$$p_c = N_p / N_2. \tag{4.5}$$

  This probability of coincidence changes from $p_c = 0$ if all tracks in the test set are completely wrong to $p_c = 1$ if all of the test tracks match the reference tracks.

- The second parameter, the *ratio of the missing tracks* r_m, is defined as

$$r_m = \frac{N_1 - N_p}{N_2} \tag{4.6}$$

and answers the question of how many reference cyclones are not detected in the test set. This additional parameter is necessary because for a small N_2 all of the test tracks can be matched to a track in the reference set ($p_c = 1$), but a large portion of the reference tracks can be still missing. r_m is equal to 0 if no track from set 1 is missing in

TABLE 4.3: Probability of coincidence p_c and ratio of missing tracks r_m for the two ERA-Interim tracking experiments (CTRL and LVT) compared with the ERA5 CTRL experiment.

	Experiment	PMC	IC
p_c	CTRL	0.87	0.97
	LVT	0.37	0.42
r_m	CTRL	7.52	7.45
	LVT	0.49	0.44

set 2, while any value $r_m > 0$ means some of the reference tracks are not present in the test set. Note that r_m has no upper limit.

According to Table 4.3, most of the PMC tracks identified in ERA-Interim CTRL run are present in ERA5. When IC are considered, p_c increases to 97 %. However, since the total number of ERA-Interim CTRL tracks is almost an order of magnitude smaller than ERA5 set, the ratio of missing tracks is quite high: 7.52 for the PMC category. The missing score is marginally lower for ICs (7.45), meaning that there is a slightly better chance for ERA-Interim to identify a strong mesoscale cyclone.

When the vorticity threshold is relaxed (LVT run), r_m drops dramatically to values below 0.50, while the ratio of PMC to IC scores stays the same. However, the percentage of correctly identified tracks decreases as well: only 37 % of ERA-Interim tracks are the same as ERA5 tracks (42 % of ICs).

These results show that lowering the tracking threshold leads to less than a half of reference tracks missing, but it also decreases the chances of tracking correct vorticity centres. This is likely due to the great increase in the number of tracks in the LVT run. Compared to p_c and r_m values presented by Blender and Schubert (2000) for synoptic-scale cyclones in a climate model, the discrepancies between ERA5 and ERA-Interim are considerably higher than expected if the only difference was the spatiotemporal resolution. This can be explained by the improvements in model physics and data assimilation in ERA5 as compared to ERA-Interim, but further tracking tests with different horizontal spacing and time steps are needed to investigate this further.

4.5.3 Temporal variability

On average, there are about 290 PMCs per extended winter season (Oct–Apr) detected in the ERA5 reanalysis, 29 of which are classified as intense. For the ERA-Interim, the mean counts are 35 and 4, respectively, if the CTRL thresholds of vorticity are used. In the LVT configuration, the number of PMCs rises to 338. The ERA5 CTRL and ERA-Interim LVT tracking produces 9.6–11.2 PMCs week^{-1} per average extended winter, which is consistent with numbers obtained by Michel et al. (2018). Comparing to earlier studies, based on completely different cyclone identification methods

and selection criteria, our results are both higher (compared e.g. to 1.8 PMCs week^{-1} in Bracegirdle and Gray (2009)) and lower (compared e.g. to 15.2 PMCs week^{-1} in Harold et al. (1999a)) than previous findings.

FIGURE 4.10: Number of PMCs in ERA5 and ERA-Interim datasets for each extended winter.

Interannual variability

The PMC counts exhibit noticeable winter-to-winter variability (Fig. 4.10), including the intense subcategory of vortices in ERA5. Interannual variations have been reported in other studies based both on satellite and modelling data (e.g. Zahn and Storch, 2008; Rojo et al., 2015; Stoll et al., 2018). Our results are also qualitatively in agreement with these studies about the absence of any significant trend in PMC activity over the North-East Atlantic, although the period is too short to make definitive conclusions.

The tracking based on ERA-Interim has relative changes that are similar to the variability in ERA5, even though the absolute values are very different. The LVT setting yields a couple of dozen of PMCs more than the ERA5 CTRL (and almost 10 times more than ERA-Interim CTRL), but winter-to-winter fluctuations are also generally the same.

Seasonal cycle

The monthly distribution of PMC is obtained by binning tracks to each of the 7 months of an extended winter, averaging the numbers over 9 seasons, and normalising the frequency by 30 days (Fig. 4.11). Note that the period covered in this study is short, and the seasonal distribution may be affected by interannual variability, as mentioned in previous studies (e.g. Stoll et al., 2018) and represented here by large error bars in Fig. 4.11.

However, we find that our results agree with previous studies that used larger time samples or different data sources (e.g. Bracegirdle and Gray, 2008; Rojo et al., 2015; Michel et al., 2018). The seasonal cycle of both PMC and ICs in the ERA5 dataset displays a steady increase in numbers from October to December, followed by a decrease in January and a local minimum in February. The February nadir is consistent with one of the earliest PMC climatologies compiled by Wilhelmsen (1985), as well as with more modern ones (e.g. Noer et al., 2011; Smirnova et al., 2015; Michel et al., 2018). The February minimum is followed by a prominent maximum in March, which has been known to occur in the Nordic Seas and shows up in several climatologies (e.g. Rojo et al., 2015; Smirnova et al., 2015; Michel et al., 2018). On the other hand, monthly mean counts in other climatological studies (e.g. Stoll et al., 2018) do not have a minimum in February and maximum in March, documenting instead a symmetrical distribution. Finally, in April the number of PMCs falls roughly to October levels. This PMC seasonal cycle is evident in all configurations.

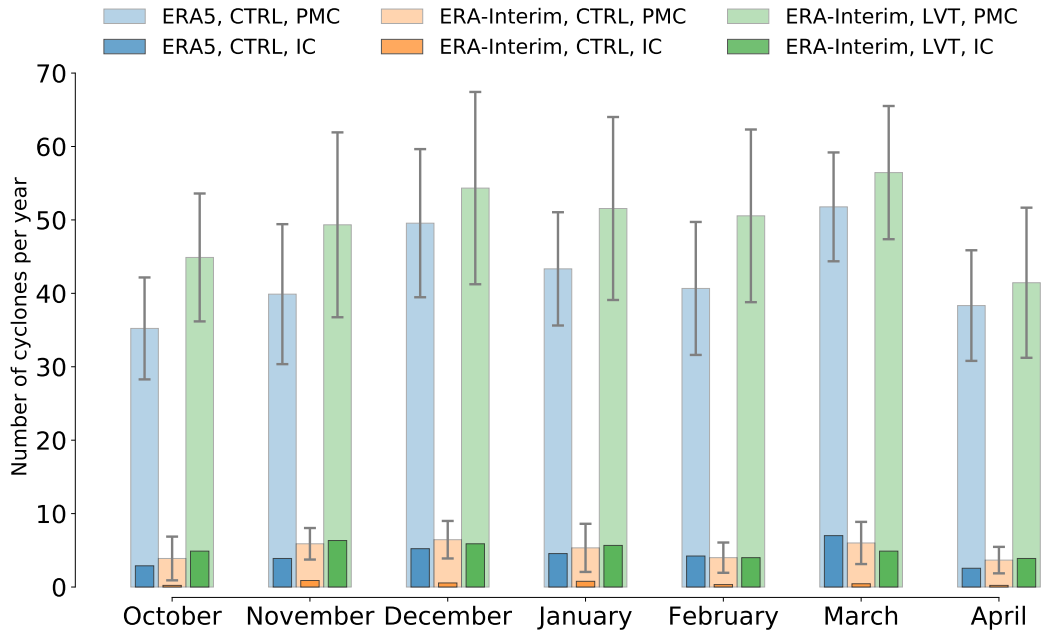

FIGURE 4.11: Number of PMCs in ERA5 and ERA-Interim reanalyses, normalised for a 30-day month. Error bars represent standard deviations on the multi-annual means for each month.

The average number per normalised month is 43 in ERA5, 5 in ERA-Interim, and

50 in ERA-Interim LVT run. The number of IC cyclones as detected in ERA5 stays approximately at 10 % of the total number of PMCs every month, although April sees a particularly low fraction of intense vortices (6.7 %), while in March this ratio rises to 13.5 % (blue bars in Fig 4.11). In the ERA-Interim LVT experiment, the IC share is similar, but has a minimum in March and a maximum in November. The November maximum is even more prominent in the ERA-Interim CTRL run, which has the largest fluctuations of the IC ratio.

4.5.4 Spatial distribution

The geographical distribution of the mesoscale vortices is presented in this section using several Eulerian statistics: track, cyclone, genesis and lysis densities. The track density is essentially the number of cyclones per unit area, computed using a single point from each track and thus is not affected by the propagation speed (Zolina and Gulev, 2002). Cyclone density, on the other hand, is defined as the number of vorticity centres per unit area during a chosen time interval (e.g. winter), and is equivalent to what is sometimes labelled as cyclone frequency (e.g. Tilinina et al., 2013) or feature density (e.g. Hoskins and Hodges, 2002). It is computed using all points along a track so that slow moving vortices contribute more to the density due to a higher number of points in an area. Cyclone density is a measure of PMC activity in a given region, and if multiplied by the time resolution of the dataset, it can be termed 'PMC duration' (Stoll et al., 2018). The genesis density, the frequency of where PMC originate, is computed as density of track starting positions excluding any tracks that start at the first time step of the tracking (1 October). The lysis density, the frequency of where PMC disintegrate, is calculated in the same way, but for ending positions and excluding tracks that are cut off by the last time step.

Following Sinclair (1994) and Condron et al. (2006), we calculate cyclone densities on a longitude-latitude grid with equal spacing and counting features within a radius of 111.3 km; consequently, the units are tracks or cyclones per 38 917 km^2. When larger radii (e.g. 222.6 km) are used in density calculations, the resulting field contains broadly the same patterns, albeit smoothed out (not shown). The densities are then divided by the number of winters (i.e. 9).

Using a simple Cartesian grid may introduce a systematic bias (Hoskins and Hodges, 2002; Zolina and Gulev, 2002) due to the tightening of the grid towards the pole. However, the area of interest in this study is relatively small, so we do not apply any area normalisation to PMC densities. Another problem that usually leads to an underestimation of cyclone density is the temporal resolution of cyclone tracks. Zolina and Gulev (2002) suggest that it is possible to reduce this bias by linearly interpolating track points to a higher resolution (e.g. 10 min). In this study, the spatiotemporal resolution is much higher than that examined by Zolina and Gulev (2002), especially in

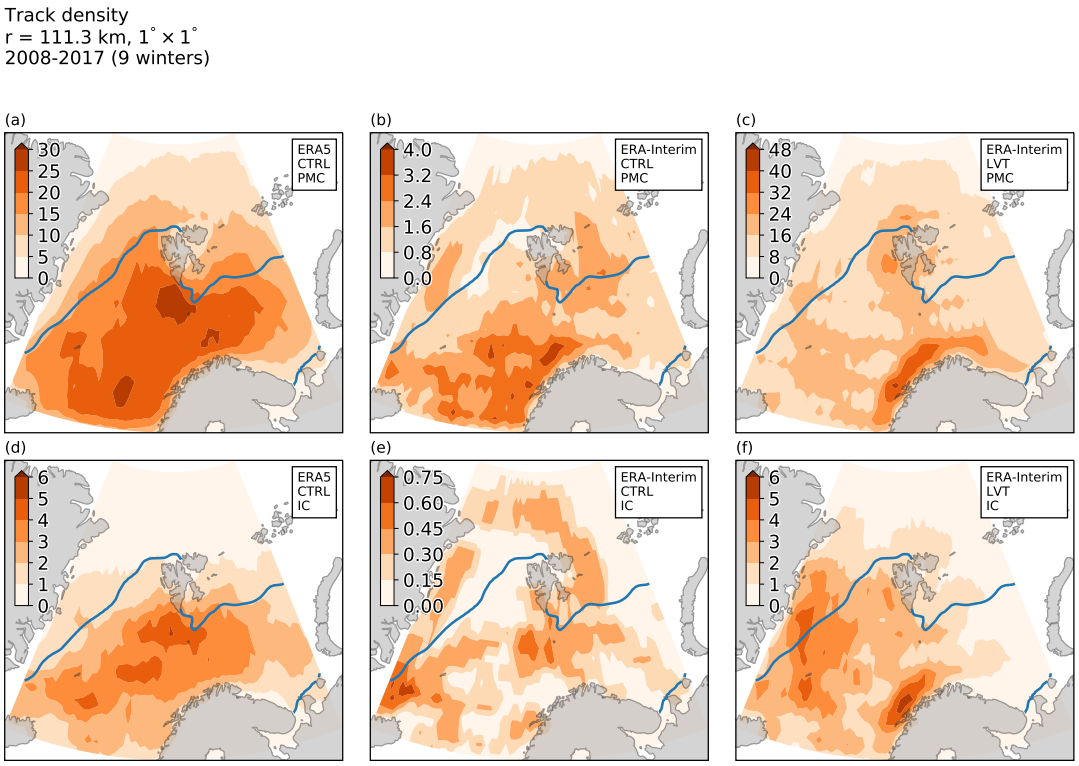

FIGURE 4.12: Cyclone track density maps comparing ERA5 and ERA-Interim. Averaged over 9 extended winters. The units are track per circle with 111.3 km radius. Note the different limits of the colour scales. The blue line denotes the average wintertime position of the sea ice edge (15 % sea ice concentration).

the case of ERA5 reanalysis, so we believe interpolation will not change the overall picture and is not used here.

Track density

PMC track density derived from ERA5 (Fig. 4.12a) has a maximum to the south and south-west of Svalbard, and secondary maxima smaller in size: one in the south of the domain, and one close to the northern Scandinavian coast. The latter 'hot spot', located roughly at 72°N 20°E, is known by Norwegian forecasters as 'Tromsø Flake' (Noer et al., 2011) and emerges in studies e.g. by Bracegirdle and Gray (2008) and (in ASR data) by Stoll et al. (2018). The main track density maximum agrees well with the climatology of Michel et al. (2018) in terms of its location near Svalbard (although in our study it is further south) as well as in absolute values, exceeding 7 PMCs per 10^4 km^2 per extended winter (Fig. 4.12a). ICs (Fig. 4.12d) have a track density maximum in the same area, but do not have secondary maxima near Norway. This is in contrast to the density maps presented by Bracegirdle and Gray (2008), in which the density maximum shifts towards Norway with increasing vorticity threshold.

Both density fields manifest an imprint of the the sea ice cover, whose average wintertime extent is shown in Figs. 4.12–4.15 as calculated from the ERA5 data. Spatial patterns in PMC distribution are generally similar to the probability of CAOs, reported by Papritz and Spengler (2017) and Fletcher et al. (2016) for the Nordic Seas. The Svalbard maximum in PMC density can be attributed to the most intense CAOs and high surface heat fluxes, while the secondary maxima are located in areas with weak CAOs.

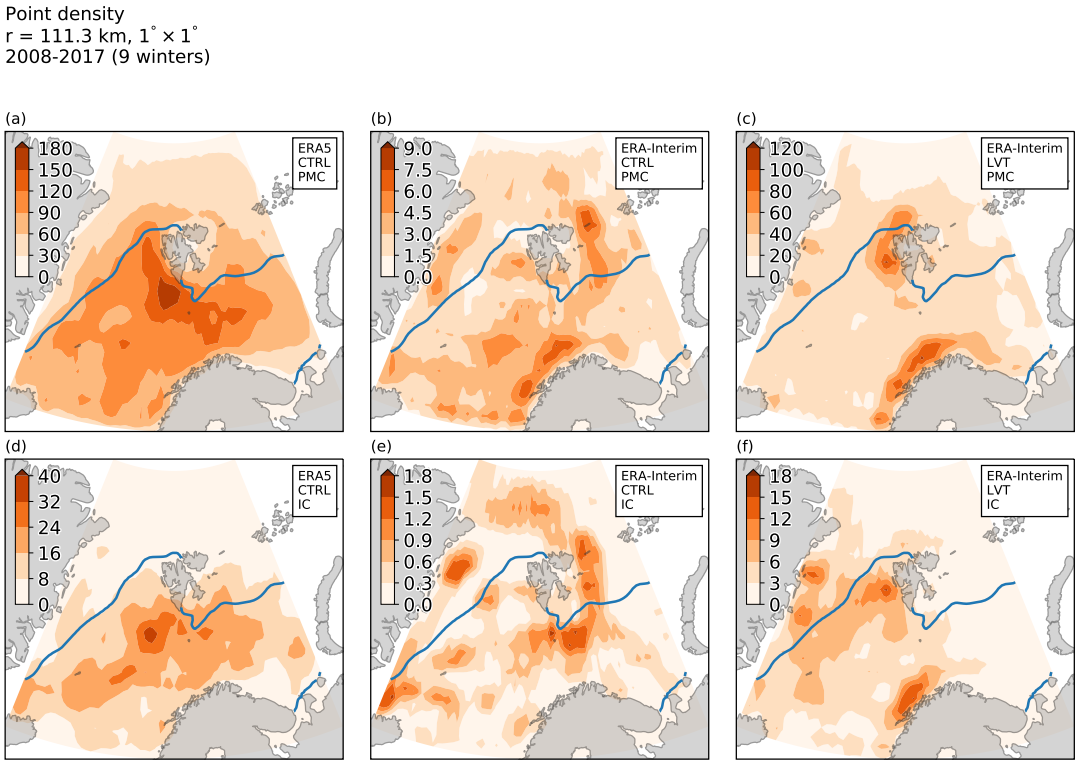

FIGURE 4.13: As in Fig. 4.12, but for cyclone density.

For ERA-Interim, the maximum in PMC density is shifted south, towards the coast and the eastern Norwegian Sea, in both CTRL and LVT runs (Fig. 4.12b,c). A local peak in density to the west of Svalbard becomes visible only in the LVT experiment. In the latter, the chief area of track density is still close to the Scandinavian coast, and is probably related to orographically-produced vorticity in the reanalysis (Fig. 4.12c).

The density maps derived from IC tracks in ERA-Interim have a distinct maximum emerging over the Greenland Sea (Fig. 4.12e,f). Thus the strongest ERA-Interim PMCs seem to form over the Irminger Sea and Denmark Strait and propagate to the north. Similar maxima of PMC activity have been also found by Harold et al. (1999b), Bracegirdle and Gray (2008), Condron and Renfrew (2013), and Stoll et al. (2018).

Cyclone density

The cyclone density (or cyclone frequency), shown in Fig. 4.13 overall has similar patterns as the track density discussed above, but is more concentrated in focal points. The maximum near Svalbard is the sole maximum in the ERA5 runs, without its counterparts in the south. This implies that vortices near Svalbard tend to be slow, while over the Norwegian Sea they move quickly and do not leave an imprint in the cyclone density.

The ERA-Interim CTRL experiment has a local peak in cyclone frequency to the east of Svalbard (Fig. 4.13b,e), meaning that there is some kind of stagnation region in that area. It does not, however appear in the LVT run (Fig. 4.13c,f).

Genesis and lysis densities

A significant number of PMCs enter the tracking domain from its southern boundary, as both reanalyses demonstrate in Fig. 4.14. Nevertheless, another peak in the cyclogenesis density emerges near Svalbard: in ERA5 experiments (Fig. 4.14a,d) and somewhat in ERA-Interim experiments for the IC category (Fig. 4.14e). The PMC genesis close to Svalbard has been confirmed by earlier climatological studies (e.g. Michel et al., 2018) and corresponds to high CAO occurrence (Papritz and Spengler, 2017). ERA-Interim tracking runs are different in that they have high cyclogenesis density spread over the Greenland and Norwegian Seas (Fig. 4.14b,f), as well as a local maximum to the north of Svalbard archipelago (e.g. Fig. 4.14c). The shift of PMC formation area to the Greenland Sea could be due to the prevalence of forward-shear cyclones (Terpstra et al., 2016; Michel et al., 2018).

The graveyard of PMCs is located at the coast of Norway (Fig. 4.15). This is the case for all 3 configurations. Besides this peak in cyclone lysis density, there are two interesting maxima emerging for the IC category: near the south-western coast of Svalbard in ERA5 CTRL experiment (Fig. 4.15d) and along the coast of Greenland in ERA-Interim LVT experiment (Fig. 4.15f). In addition, just as in the cyclogenesis densities, there is a maximum along the domain boundary (e.g. Fig. 4.15a), which in this case corresponds to PMCs exiting the domain.

The distribution of cyclolysis in the present study is quite different to results obtained by Michel et al. (2018), in which the lysis density is rather even in the domain. However, our results seem tenable because PMCs are known to often make landfall in Scandinavia (e.g. Wilhelmsen, 1985; Businger, 1985; Noer et al., 2011), as for example illustrated by the ACCACIA event (Chapter 2) as well as the two events discussed in Chapter 3.

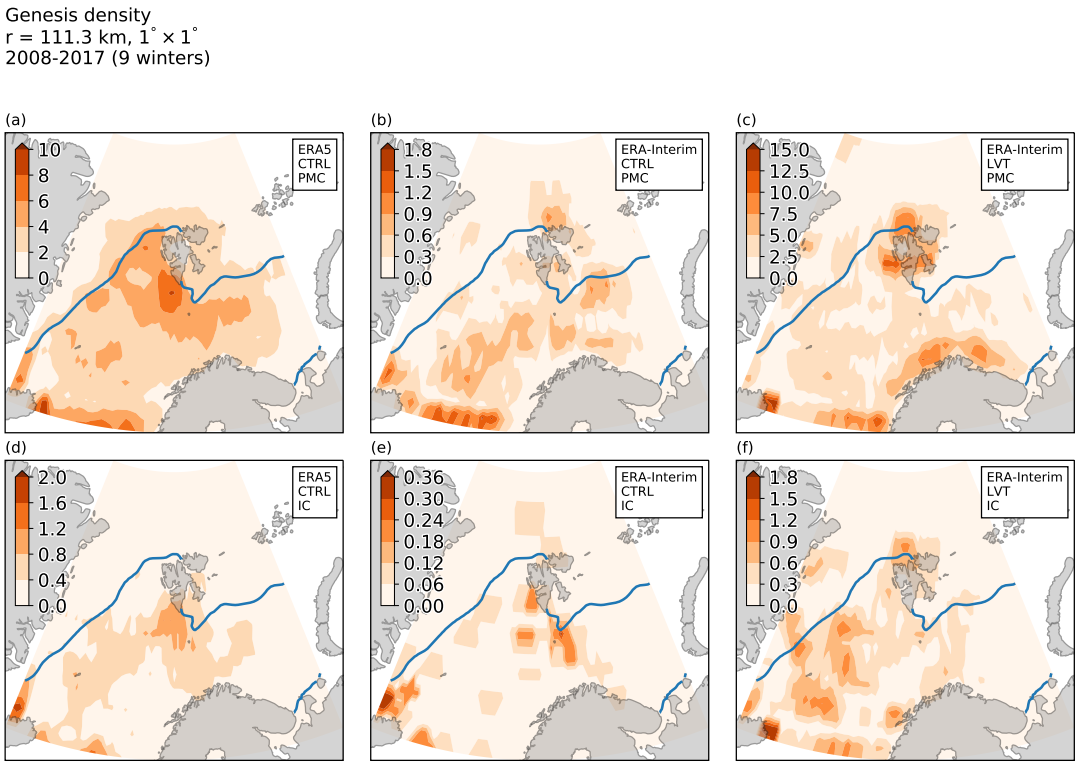

FIGURE 4.14: As in Fig. 4.12, but for genesis density.

Summary

A significant number of PMCs form in the vicinity of Svalbard according to the ERA5 reanalysis. ERA5 represents this local maximum in a better agreement with observational studies (e.g. Rojo et al., 2015; Smirnova et al., 2015). ERA-Interim, on the other hand, appears to have a few questionable genesis maxima, for instance, along the Norwegian coast and north of Svalbard.

When the whole track is taken into account, ERA5 correctly produces a PMCs activity peak in the northern Norwegian Sea, which aligns well with satellite climatology of Harold et al. (1999a), but does not clearly emerge in our tracking based on ERA-Interim. In terms of PMC dissipation, ERA5 and ERA-Interim agree better with each other by having a cyclolysis maximum near the coast of Scandinavian peninsula, confirming the track pattern reported by Businger (1985).

4.6 Arctic sea ice and PMC activity

For almost four decades the annual mean sea ice extent in the Arctic has been diminishing at an average rate of 3.5–4.1 % decade^{-1} (Vaughan et al., 2013). In the Atlantic sector of the Arctic, the sea ice decline is one of the most rapid on the planet. Cavalieri and Parkinson (2012) report that the largest negative trends are in fact in

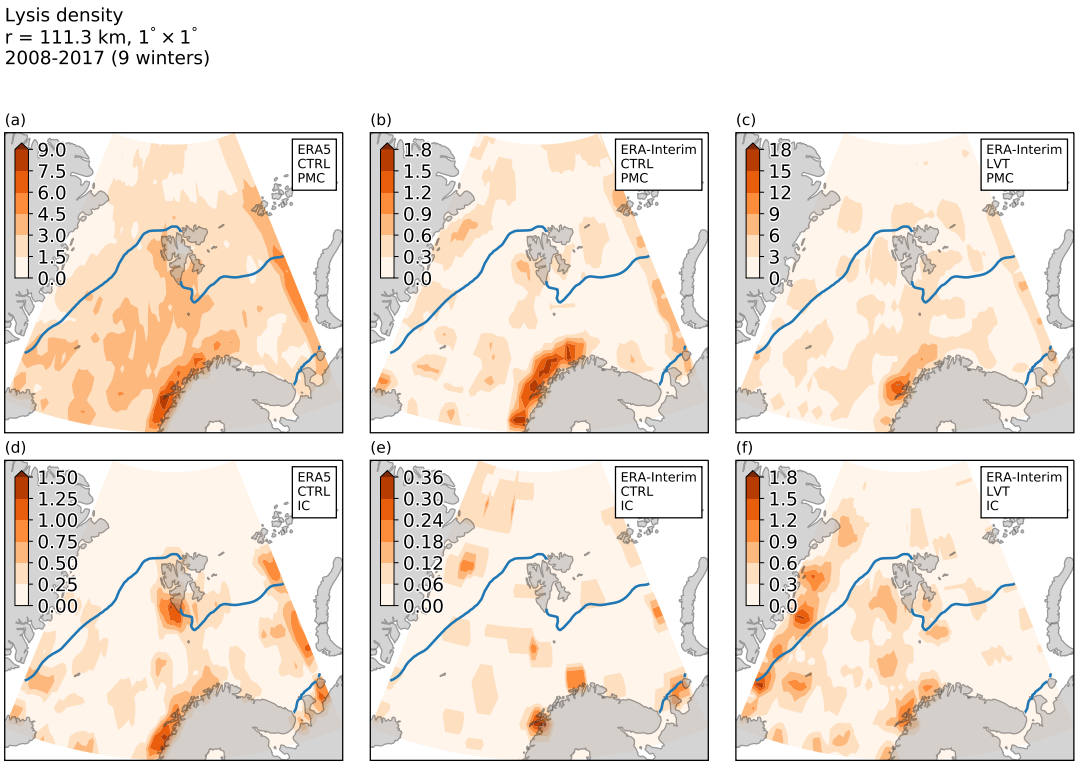

FIGURE 4.15: As in Fig. 4.12, but for lysis density.

the Greenland Sea and the Kara and Barents Sea regions: $-8.6 \pm 1.5\,\%\,\text{decade}^{-1}$ and $-9.2 \pm 1.6\,\%\,\text{decade}^{-1}$, respectively. However, there is considerable interannual variability, with the recent extreme minima observed in 2007 and 2012. While the cyclonic activity is one of the factors contributing to the the record minima (e.g. Zhang et al., 2013), the life cycle of CAOs, and thus PMC activity is likely to depend on the sea ice extent. This section attempts to analyse how the PMC distribution in ERA5 changes throughout the period of the sea ice decline.

The sea ice concentration is one of the parameters available in the ERA5 dataset (`paramId=31`, %). In the present study, it has been retrieved for the same region as the tracking domain (Fig. 4.1), and multiplied by the grid cell area to obtain the *sea ice area*. In the grid cells with sea ice concentration less than 15 %, the sea ice area is zero. Note that it is different to the *sea ice extent*, which is always slightly larger[11].

Integrated over the domain and averaged over extended winters, the total sea ice area during 2008-2017 is about $0.8 \times 10^6\,\text{km}^2$. Although the period of interest is short and the sea ice area exhibits large interannual variability, the downward linear trend is clear in Fig. 4.16. The average sea ice decrease is $-0.025 \times 10^6\,\text{km}^2\,\text{yr}^{-1}$, or $\approx 30\,\%\,\text{decade}^{-1}$. To assess the statistical significance of this domain-integrated trend, we apply a simple two-sided non-parametric test, namely random resampling

[11] http://nsidc.org/arcticseaicenews/faq

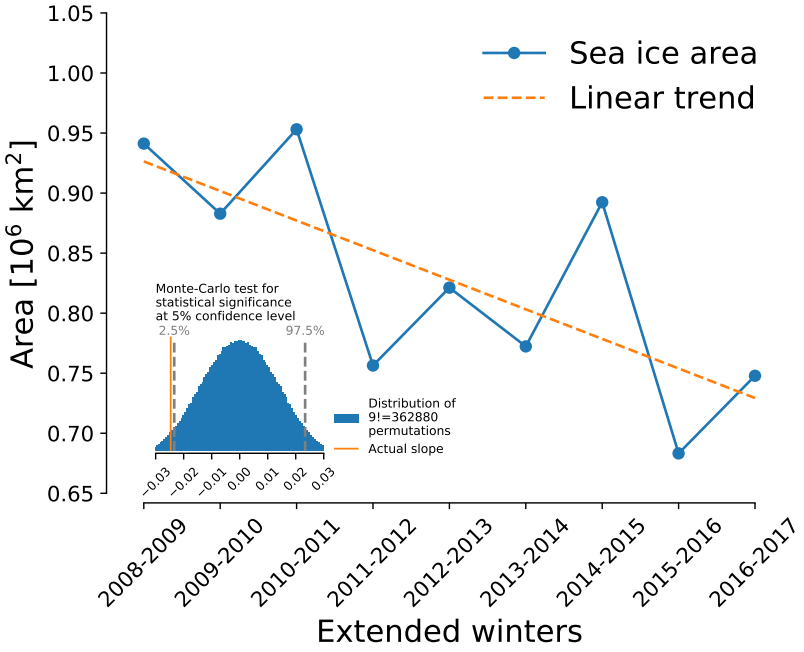

FIGURE 4.16: Sea ice area trend and linear trend over 9 extended winters.

(e.g. Matthews and Kiladis, 1999; Reeve and Kolstad, 2011). Since it was computationally inexpensive, we use all possible permutations of sea ice area time series, i.e. $9! = 362,880$ in total (although the result does not change when only 1000 is used). For each of these Monte Carlo simulations a linear regression is calculated, giving the null distribution against which the actual realisation is tested for statistical significance. As the inset in Fig. 4.16 demonstrates, the actual slope of the sea ice area regression falls outside the interval formed by 0.025 and 0.975 quantiles, and hence is statistically significant at the 5 % level.

Such a clear trend does not, however, emerge in the annual numbers of mesoscale cyclones (Fig. 4.10). Nevertheless, we attempt to investigate whether the Arctic sea ice loss is associated with local trends in PMC track density.

First, a map of sea ice concentration trends is obtained by calculating the linear regression coefficient (slope) in each grid cell (Fig. 4.17a). The statistical significance of these trends is assessed using the same method as above. Evidently, the sea ice retreat is happening mostly in the Barents Sea, to the east and north-east of Svalbard. Other regions of sea ice loss appear in the Greenland Sea, as well as in the south of the Barents Sea, corroborating the study of earlier years by Cavalieri and Parkinson (2012).

The spatial pattern of 9-winter trends in PMC track density is rather patchy (Fig. 4.17b). In the region of the most rapid sea ice retreat in the Barents Sea, the trend in track density is mostly positive, but only statistically significant at the domain boundaries. Locally significant, negative trends in track density over the Greenland-Norwegian

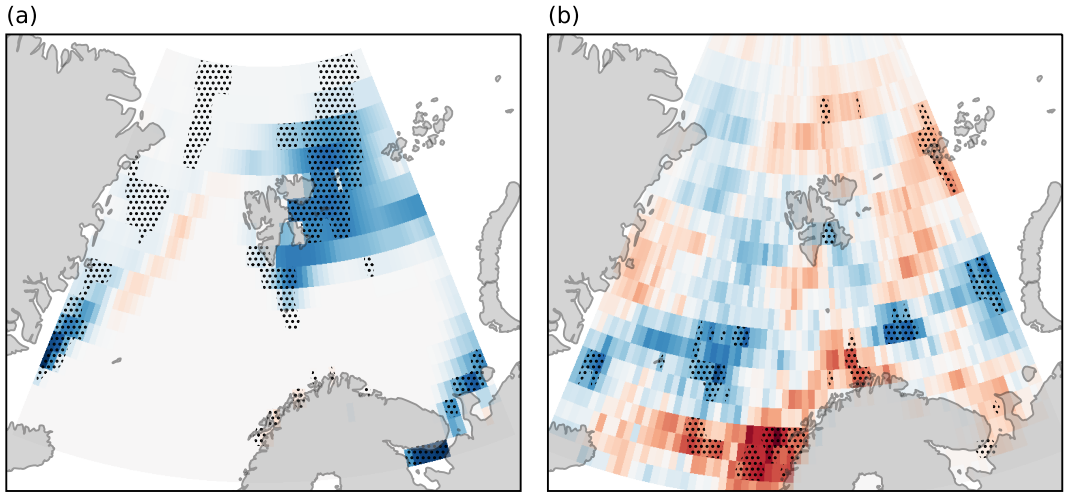

FIGURE 4.17: Linear trends in (a) sea ice and (b) ERA5 PMC track density over 9 extended winters. Blue (red) colours indicate negative (positive) slope of the linear regression. Stippling indicates local statistical significance at 10 % confidence level.

basin, and positive trends close to the coast of Norway suggest that PMCs occur more frequently close to Scandinavia during winters with reduced sea ice concentration. This is qualitatively in agreement with Michel et al. (2018), who found the same tendency in PMC occurrence.

Because of the high interannual variability of cyclone densities these trends have to be regarded with caution. The map of local (at each grid point) statistical significance (Fig. 4.17b) has been tested for field significance using a Monte Carlo method (Matthews and Kiladis, 1999). Due to spatial correlations in the data as well as the finiteness of the sample size, the resulting null distribution exhibits considerable spread, and the actual realisation shown in Fig. 4.17b fails the test at 5 % level. Thus to quantify the response of PMCs to the sea ice extent, one needs a longer time series than that presented here, or preferably a coupled climate simulation (H. Bresson, 2018, personal communication). Furthermore, great care should be taken when interpreting correlations between the sea ice extent and cyclone activity, as they have been found sensitive to various aspects of the climate model, as well as variables used for tracking (Rae et al., 2017).

4.7 Summary

A new climatology of PMCs based on objective tracking and the new ERA5 reanalysis has confirmed that the their occurrence has local maxima in the Nordic Seas, one of which is situated south of Svalbard. This area is associated with a high frequency of marine CAOs leading to the genesis of PMC which often make landfall in Norway. In

addition, a significant amount of PMCs start to develop over the North Atlantic and enter the region of interest from the south.

In agreement with earlier studies, the PMC climatology presented here exhibits some interannual variability, but no significant trend is observed for the 9 winter seasons. On average, there are 290 PMCs detected in ERA5 data from October to April. The seasonal cycle has a prominent maximum in March and a minimum in February.

The representation of PMCs has been investigated in two ECMWF reanalyses: ERA5 and ERA-Interim. A short look at the ACCACIA event illustrates that ERA5 is more capable of reproducing a strong wind shear and vorticity in the lower troposphere and thus allows for more accurate PMC tracking. Lowering the vorticity thresholds in ERA-Interim does not automatically result in better tracking results, and there are still significant disagreements between individual tracks in ERA5 and ERA-Interim. Consequently, the patterns found in spatial distribution of PMCs differ between ERA5 and ERA-Interim, even when the latter is used with lower vorticity threshold for tracking.

This chapter has showed that ERA5 clearly has great potential for studies of mesoscale cyclones from a climatological perspective. We anticipate continuing the research presented here once the reanalysis is released for the whole period (starting from 1950). The key areas that need further investigation are as follows (more are given in Chapter 5).

The sensitivity of the tracking algorithm to the temporal resolution has to be examined by running the tracking experiments with larger time steps (e.g. 3, 6 h) for ERA5. This will make the comparison with ERA-Interim reanalysis fairer. In addition, tracks derived from both datasets can be 'artificially' interpolated to a higher time resolution to improve cyclone density maps.

The link between the Arctic sea ice extent and PMC activity need to be investigated more thoroughly by expanding our analysis both in time and to a larger region to find a robust response, if it exists, in cyclone development to the sea ice loss.

5

Conclusions

Despite substantial improvements in numerical weather prediction (NWP) models, an ever increasing amount of satellite observations, and numerous of theoretical studies, PLs are still not fully understood. Their small scale and rapid development continues to be challenging for modern weather forecasting centres. The Nordic Seas, as well as other sectors of the Arctic Ocean, have seen a decline of sea ice cover and are expected to have increased level of shipping in the twenty-first century (Melia et al., 2016). PLs are one of the weather hazards most likely to affect the safe navigability of these routes.

In the present thesis, we have looked at the characteristics of PLs in the Nordic Seas from a few different angles: a case study based on unique data gathered during a field campaign; sensitivity experiments with artifically modified orography and sea ice cover; and a climatology based on objective tracking and two state-of-the-art reanalyses.

5.1 ACCACIA case study

Among mesoscale vortices occurring in the Nordic Seas, many are associated with shear lines. Given the lack of routine and targeted observations, shear-line PL cases are underrepresented in the literature; while the processes responsible for their development are not well understood.

Fortunately, one such cyclone was probed during the ACCACIA field campaign on 26 March 2013. Its structure and evolution has been thoroughly investigated using

direct aircraft and dropsonde measurements, as well as satellite radar and scatterometer data. To complement the observational data, we ran the UK Met Office Unified Model (MetUM) with a convection-permitting resolution.

The ACCACIA PL formed during an intense marine CAO, which converged into vorticity filaments near the Svalbard archipelago. The analysis revealed a mesoscale cyclone with gale force near-surface wind speed and relative vorticity of an order of magnitude larger than the Coriolis parameter. In the vertical, it was characterised by the reverse-shear conditions, that are typical for CAOs triggered by a synoptic-scale low in the Barents Sea. Due to high wind velocity and a neutral-to-unstable boundary layer stratification, the turbulent heat flux from the surface exceeded $500\,\mathrm{W\,m^{-2}}$ with the sensible heat flux (SHF) almost twice a large as the latent heat flux (LHF) (though the model tends to overestimate this ratio — see the next paragraph). Consequently, the shear line was concomitant with vigorous convection, hinting at the importance of latent heat release in the intensification of the PL. The convective cloud bands appeared to be predominantly mixed-phase below 2.5 km and glaciated above, as was revealed by in situ observations and CloudSat radar reflectivity scans, and corroborated by the numerical simulation.

The MetUM greatly helped to reconstruct the full life cycle of the PL and filled the gaps in observations. Another outcome of this study is the successful validation of the model in its 'ENDGame' configuration. The model captures the structure of the wind field very well, compared to aircraft observations and ASCAT scatterometer wind retrievals. However, it tends to make the surface layer within the CAO too stable and too humid, which leads to an overestimation of SHF and underestimation of the LHF. Among the MetUM's largest biases is the balance between the ice crystal and water droplet concentrations within the PL cloud bands, although the total humidity profiles are reproduced reasonably well. Namely, the clouds appear over-glaciated, suggesting MetUM is too efficient at removing liquid water: the simulated liquid water content is at least one order of magnitude smaller than that measured by the aircraft and CloudSat's radar.

It is worth noting that our case study presents the first detailed microphysics measurements inside a PL. We showed that this PL's cloud environment is similar to that of typical CAOs, but being on the edge of a CAO, the PL had higher cloud tops and a more developed convection. The representation of PL clouds suffers from the same over-glaciation bias as was found in MetUM before (Field et al., 2014), as well as in other numerical models (Klein et al., 2009).

For the first time, a PL was simulated using a horizontal grid size of 0.5 km. This resolution produces an even better resemblance between simulated convective cloud patterns and the infrared satellite images. However, a comparison of wind speed and surface pressure to aircraft observations revealed that this reduction in grid spacing does not give a remarkable improvement in model performance.

The structure of this shear-line PL suggests that it was driven by a synergy of dynamical mechanisms, including e.g. barotropic instability within the narrow vorticity bands, as well as convective processes manifested by the cloud bands. Our study provides a useful combination of datasets to quantify contributions of different energy sources for the PL development. However, this is merely a single case of shear-line PLs, and more observations are required to create a composite picture of such weather systems. Another limitation of this study is that the PL was probed by remote and in situ observations within a relatively short time window, and the flight pattern did not capture all of its parts.

5.2 Sensitivity to orography and sea ice

Prompted by the fact that the ACCACIA PL developed immediately downstream of Svalbard, we conducted sensitivity experiments to determine the role of Svalbard's mountains as well as the sea ice around it in creating favourable conditions for mesoscale cyclogenesis. A few previous studies have investigated the influence of orography on PL development (e.g. Gallée, 1995; Klein and Heinemann, 2002; Kristjánsson et al., 2011), but none of them focused on Svalbard. Sea ice was reported to be important for mesoscale cyclogenesis in various subpolar regions, e.g. in Hudson Bay (Albright et al., 1995) and the Japan Sea (Watanabe et al., 2017). As for the Nordic Seas, only one real-case numerical study tested the sensitivity of a PL to the sea ice distribution (Adakudlu and Barstad, 2011). In the present study, our goal was to progress further in this topic.

We used the same model configuration as in the first part of this work, but concentrated our attention on two more illustrative PLs: No. 72 and No. 77 from the STARS catalogue. The large-scale atmospheric conditions were similar to the ACCACIA case and were characterised by the large-scale depression centred over northern Norway and an anticyclone centred over Greenland. This typically leads to northerly CAOs and is a favourable weather regime for the PL activity (Kolstad et al., 2009; Mallet et al., 2017).

Due to the sufficiently high static stability and weak wind upstream, Svalbard split the northerly flow and produced vorticity filaments at its corners. They eventually contributed to the growth of mesoscale cyclones downstream, supplied by heat and moisture from the surface. The importance of air-sea interaction was illustrated by kinematic backward trajectory calculations. Trajectories entering the warm core of the PLs demonstrated that the air parcels coming from the north were heated diabatically. The trajectory analysis showed that an important source of air parcels for both PLs is the Barents Sea. This was also seen in the low-level relative vorticity field: vorticity filaments emanating from Svalbard typically merge with vorticity clusters on the periphery of the synoptic-scale depression over the Barents Sea.

These vorticity clusters appeared to be the *primary* source for the PL initiation, while Svalbard's mountains provide a *secondary* source. We proved this by replacing the islands of Svalbard with sea ice in a pair of sensitivity experiments, which showed that the PLs developed nonetheless, mostly growing on convectively-driven vorticity clusters from the Barents sea. Doubling the height of Svalbard, on the other hand, increased the vorticity production at its flanks and deflected the PL tracks. However, a PL can be less affected by the orography, if its development is aided by an upper-level potential vorticity (PV) anomaly (such as the STARS-72 PL).

A decrease in sea ice cover west of Svalbard resulted in a moderate intensification of the PLs, particularly for the more convectively-driven case, while increased sea ice cover significantly hindered their development, because weaker surface fluxes led to a more stable stratification and less condensational heating. The decrease of PL intensity happened despite a higher surge in the heat fluxes at the ice edge when it was moved south, because in the early stages of its life cycle, the PLs were deprived of this energy source.

While a comparison with Adakudlu and Barstad (2011) is not straightforward because of the different synoptic situation in our cases and the inability of their model to reproduce a PL in the control simulation, our results confirm one of their finding. Namely, the removal of the sea ice near Svalbard does not dramatically affect the strength of a PL. To test the sensitivity of the two PLs presented here to the changes in SST and confirm the results of Adakudlu and Barstad (2011), more numerical simulations are required.

Our numerical experiments exemplified that mesoscale cyclones in the North-East Atlantic can withstand large perturbations in the surface conditions (such as the removal of Svalbard) and still develop to sufficient intensity to be labelled as polar lows. However, there is a sensitivity to Svalbard's orography and surrounding sea ice cover, illustrated by a clear modulation of PL genesis and development.

A caveat is that our investigation relies only on two events. Thus the generality of our results is uncertain, and more multi-event studies are required to pinpoint the influence of Svalbard and sea ice around it in different synoptic situations.

5.3 Climatology and reanalyses comparison

By compiling a new climatology of mesoscale vortices in the Nordic Seas, we revised the interannual and interseasonal, as well as geographical characteristics of PMC activity in the Nordic Seas. Moreover, we have made a first step towards drawing conclusions about the statistical significance of the impact of sea ice on PMCs.

The climatology was derived using two ECMWF reanalysis products: ERA5 and ERA-Interim. The former is used for PL analysis for the first time. ERA5 is produced by one of the latest versions of ECMWF's IFS model and has a number of advantages

over ERA-Interim, including much higher spatiotemporal resolution and improved data assimilation. One of the motivations for our study was to test what improvements in PMC tracking the new reanalysis brings compared to its predecessor.

Addressing the issue of subjectivity in many statistical studies of PMC, we apply an automatic vorticity-based tracking method introduced by Watanabe et al. (2016). To justify the use of this method, we tested it against two mesoscale cyclone datasets, totalling 67 cyclone tracks.The objective tracking algorithm was proven to be sufficiently effective in PMC tracking and was then applied to the full available period when ERA5 and ERA-Interim overlap (9 extended winters of 2008–2017).

Overall, ERA5 reproduced the spatial distribution of PMC occurrence closer to satellite-based climatologies, compared to the results from ERA-Interim. For example, the track density maximum to the south of Svalbard found by Harold et al. (e.g. 1999a) was confirmed by ERA5, but not ERA-Interim. Nevertheless, both reanalyses tend to agree with each other about a cyclolysis maximum near the coast of Scandinavian peninsula.

One of the reasons for ERA5's better performance is its capability of resolving wind speed maxima and gradients in the lower troposphere with higher fidelity than that of ERA-Interim. This was highlighted by a brief examination of how the ACCACIA PL is represented in the two reanalyses compared to the observations presented in the first part of this work. In addition, we demonstrated that simply changing the vorticity threshold used by the tracking algorithm does not necessarily result in better identification. Indeed, individual PMC paths can differ between ERA5 and ERA-Interim.

Having confirmed most of the earlier reported temporal and spatial patterns of PMC activity in the Nordic Seas and encouraged by the ERA5 performance, we extended our analysis to answer the question of whether any changes in mesoscale track density can be connected to the recent decline in Arctic sea ice observed in recent years. In terms of the total number of PMCs, there was no distinct trend over the years of 2008–2017. On the other hand, we obtained a locally significant increase of PMC occurrence near the coast of Norway, which is qualitatively in line with Michel et al. (2018).

The limitation of our climatology is the relatively short period of 9 extended winters spanned by ERA5 as of now. The implication is that the features of PMC activity reported here may be subject to a large interannual variability. A longer dataset is required for a robust assessment of trends in PMC track density and its correlation with retreating sea ice. ERA5 has opened new prospects for PMC studies, and once the full dataset is released we anticipate that extending the research presented here will be straightforward.

5.4 Suggested future work

This thesis progresses the knowledge of PMCs in a number of aspects, but still leaves open questions that may serve as a basis of future work.

5.4.1 MetUM simulations

As was shown by the ACCACIA case study, the limited-area configuration of the MetUM with 2.2 km grid spacing is capable of simulating the structure and life cycle of mesoscale cyclones with high veracity, which makes it a powerful tool for future investigations and sensitivity experiments. However, additional model validation would be beneficial not only for forecasting skill improvements but also for better understanding of the physical processes within mesoscale cyclones. These can include a systematic comparison between different microphysics schemes as well as boundary layer parameterizations in the MetUM model. To the best of our knowledge, the latter has not been addressed in previous studies.

5.4.2 Combining satellite observations

We demonstrated that spaceborne radar observations from CloudSat provide an insight into the cloud structure of PMCs. This is especially valuable when no in situ measurements are available. A possible follow-up investigation would be to conduct a composite analysis of PMC cloud bands based on CloudSat data and combine it with the growing volume of other satellite observations, e.g. from scatterometers or SARs.

5.4.3 Extension of sensitivity experiments

The sensitivity experiments with altered orography and sea ice need to be continued to improve the generality of our two-case study analysis. Specifically, the sample size of PMCs should be increased to include events developing in different synoptic situations and sea ice conditions in the Nordic Seas (or in other high-latitude regions). This work has been started by performing preliminary sensitivity runs for a dozen of STARS cyclones.

The sensitivity experiment set-up should address various sea ice configurations, in addition to those presented here. Such a multi-event study can be corroborated by a backward trajectory analysis, which proved to be useful in our research.

5.4.4 Exploiting the ERA5 reanalysis

To make conclusions about a large-scale impact of sea ice cover on the mesoscale cyclogenesis in the Nordic Seas, future work can rely on the objective climatology derived here for 9 winter seasons (and soon to be extended for the 1950–2018 period).

The PMC occurrence in the Norwegian Sea can be correlated with the atmospheric conditions (such as static stability and wind speed) upstream of the Svalbard archipelago, which would complement individual case studies and help to understand the role of orography on a climatological scale.

Similarly, the impact of Arctic sea ice extent on PMCs needs to be analysed based on longer time series and concentrated on subregions of the North Atlantic separately. Earlier studies show that one of the regions with the most rapid sea ice decline is the Barents Sea. Our results, however, do not show a statistically significant trend in PMC density in that area. This should be investigated further.

Finally, the objective tracking dataset can be used to compile composite fields from ERA5 not only to investigate the typical structure of a PMC but also to examine the large-scale conditions and weather regimes during different stages of PMC development.

5.4.5 Algorithms for PMC tracking

There is a need for a wide intercomparison project to define what meteorological field (e.g. vorticity or pressure) is more suitable for automatic PMC tracking. A starting point can be the study by Neu et al. (2013), who compared the statistics of synoptic-scale cyclones using several tracking algorithms. One of the outcomes of such project could be an objective global dataset of PMC tracks, based e.g. on ERA5 data. This would reduce the uncertainty due to the subjective nature of some previous PMC climatologies.

Bibliography

Abel, S. J. and I. A. Boutle (2012). "An improved representation of the raindrop size distribution for single-moment microphysics schemes". In: *Quarterly Journal of the Royal Meteorological Society* 138.669, pp. 2151–2162.

Adakudlu, M. (2012). "Impact of different initial conditions on the growth of polar lows: idealised baroclinic channel simulations". In: *Quarterly Journal of the Royal Meteorological Society* 138.666, pp. 1297–1307.

Adakudlu, M. and I. Barstad (2011). "Impacts of the ice-cover and sea-surface temperature on a polar low over the Nordic seas: a numerical case study". In: *Quarterly Journal of the Royal Meteorological Society* 137.660, pp. 1716–1730.

Albright, M. D., R. J. Reed, and D. W. Ovens (1995). "Origin and structure of a numerically simulated polar low over Hudson Bay". In: *Tellus A* 47.5, pp. 834–848.

Blechschmidt, A.-M. (2008). "A 2-year climatology of polar low events over the Nordic Seas from satellite remote sensing". In: *Geophysical Research Letters* 35.9, p. L09815.

Blechschmidt, A.-M., S. Bakan, and H. Graßl (2009). "Large-scale atmospheric circulation patterns during polar low events over the Nordic seas". In: *Journal of Geophysical Research* 114.D6, p. D06115.

Blender, R. and M. Schubert (2000). "Cyclone Tracking in Different Spatial and Temporal Resolutions". In: *Monthly Weather Review* 128.2, p. 377.

Bodas-Salcedo, A. et al. (2011). "COSP: Satellite simulation software for model assessment". In: *Bulletin of the American Meteorological Society* 92.8, pp. 1023–1043.

Bracegirdle, T. J. and S. L. Gray (2008). "An objective climatology of the dynamical forcing of polar lows in the Nordic seas". In: *International Journal of Climatology* 28.14, pp. 1903–1919.

— (2009). "The dynamics of a polar low assessed using potential vorticity inversion". In: *Quarterly Journal of the Royal Meteorological Society* 135.641, pp. 880–893.

Bracegirdle, T. J. and E. W. Kolstad (2010). "Climatology and variability of Southern Hemisphere marine cold-air outbreaks". In: *Tellus A: Dynamic Meteorology and Oceanography* 62.2, pp. 202–208.

Bromwich, D. H. et al. (2016). "A comparison of the regional Arctic System Reanalysis and the global ERA-Interim Reanalysis for the Arctic". In: *Quarterly Journal of the Royal Meteorological Society* 142.695, pp. 644–658.

Brown, A. R. et al. (2008). "Upgrades to the Boundary-Layer Scheme in the Met Office Numerical Weather Prediction Model". In: *Boundary-Layer Meteorology* 128.1, pp. 117–132.

Brümmer, B., G. Müller, and G. Noer (2009). "A Polar Low Pair over the Norwegian Sea". In: *Monthly Weather Review* 137.8, pp. 2559–2575.

Businger, S. (1987). "The synoptic climatology of polar-low outbreaks over the Gulf of Alaska and the Bering Sea". In: *Tellus A*, pp. 307–325.

Businger, S. (1985). "The synoptic climatology of polar low outbreaks". In: *Tellus A* 37A.5, pp. 419–432.

Carleton, A. M. and D. A. Carpenter (1990). "Satellite climatology of 'polar lows' and broadscale climatic associations for the Southern Hemisphere". In: *International Journal of Climatology* 10.3, pp. 219–246.

Cavalieri, D. J. and C. L. Parkinson (2012). "Arctic sea ice variability and trends, 1979-2010". In: *The Cryosphere* 6.4, pp. 881–889.

Chelton, D. B. et al. (2006). "On the Use of QuikSCAT Scatterometer Measurements of Surface Winds for Marine Weather Prediction". In: *Monthly Weather Review* 134.8, pp. 2055–2071.

Chen, F. and H. von Storch (2013). "Trends and Variability of North Pacific Polar Lows". In: *Advances in Meteorology* 2013, pp. 1–11.

Claud, C. et al. (2004). "Polar low le Cygne: Satellite observations and numerical simulations". In: *Quarterly Journal of the Royal Meteorological Society* 130.598, pp. 1075–1102.

Condron, A., G. R. Bigg, and I. A. Renfrew (2006). "Polar Mesoscale Cyclones in the Northeast Atlantic: Comparing Climatologies from ERA-40 and Satellite Imagery". In: *Monthly Weather Review* 134.5, pp. 1518–1533.

Condron, A. and I. A. Renfrew (2013). "The impact of polar mesoscale storms on northeast Atlantic Ocean circulation". In: *Nature Geoscience* 6.1, pp. 34–37.

Cook, P. A. and I. A. Renfrew (2015). "Aircraft-based observations of air-sea turbulent fluxes around the British Isles". In: *Quarterly Journal of the Royal Meteorological Society* 141.686, pp. 139–152.

Craig, G. C. (1995). "Radiation and polar lows". In: *Quarterly Journal of the Royal Meteorological Society* 121.521, pp. 79–94.

Craig, G. C. and S. L. Gray (1996). "CISK or WISHE as the Mechanism for Tropical Cyclone Intensification". In: *Journal of the Atmospheric Sciences* 53.23, pp. 3528–3540.

Craig, G. and H.-R. Cho (1988). "Cumulus Heating and CISK in the Extratropical Atmosphere. Part I: Polar Lows and Comma Clouds". In: *Journal of the Atmospheric Sciences* 45.19, pp. 2622–2640.

Dacre, H. F. and S. L. Gray (2006). "Life-cycle simulations of shallow frontal waves and the impact of deformation strain". In: *Quarterly Journal of the Royal Meteorological Society* 132.620, pp. 2171–2190.

Davies, T. et al. (2005). "A new dynamical core for the Met Office's global and regional modelling of the atmosphere". In: *Quarterly Journal of the Royal Meteorological Society* 131.608, pp. 1759–1782.

Dee, D. P. et al. (2011). "The ERA-Interim reanalysis: Configuration and performance of the data assimilation system". In: *Quarterly Journal of the Royal Meteorological Society* 137.656, pp. 553–597.

Deveson, A. C. L., K. A. Browning, and T. D. Hewson (2002). "A classification of FASTEX cyclones using a height-attributable quasi-geostrophic vertical-motion diagnostic". In: *Quarterly Journal of the Royal Meteorological Society* 128.579, pp. 93–117.

Dierer, S. and K. H. Schluenzen (2005). "In fluence parameters for a polar mesocyclone development". In: *Meteorologische Zeitschrift* 14.6, pp. 781–792.

Douglas, M. W., L. S. Fedor, and M. A. Shapiro (1991). "Polar Low Structure over the Northern Gulf of Alaska Based on Research Aircraft Observations". In: *Monthly Weather Review* 119.1, pp. 32–54.

Douglas, M. W. et al. (1995). "Research Aircraft Observations of a Polar Low at the East Greenland Ice Edge". In: *Monthly Weather Review* 123.1, pp. 5–15.

Doyle, J. D. and M. A. Shapiro (1999). "Flow response to large-scale topography: the Greenland tip jet". In: *Tellus A: Dynamic Meteorology and Oceanography* 51.5, pp. 728–748.

Dritschel, D. G. et al. (1991). "The stability of a two-dimensional vorticity filament under uniform strain". In: *Journal of Fluid Mechanics* 230.-1, p. 647.

Duncan, C. N. (1977). "A numerical investigation of polar lows". In: *Quarterly Journal of the Royal Meteorological Society* 103.436, pp. 255–267.

Egger, J. and T. Spengler (2018). "Nonuniqueness of Attribution in Piecewise Potential Vorticity Inversion". In: *Journal of the Atmospheric Sciences* 75.3, pp. 875–883.

Elvidge, A. D. et al. (2015a). "Observations of surface momentum exchange over the marginal-ice-zone and recommendations for its parameterization". In: *Atmospheric Chemistry and Physics Discussions* 15.19, pp. 26609–26660.

Elvidge, A. D. et al. (2015b). "Foehn jets over the Larsen C Ice Shelf, Antarctica". en. In: *Quarterly Journal of the Royal Meteorological Society* 141.688, pp. 698–713.

Emanuel, K. A. (1986). "An Air-Sea Interaction Theory for Tropical Cyclones. Part I: Steady-State Maintenance". In: *Journal of the Atmospheric Sciences* 43.6, pp. 585–605.

Emanuel, K. A. and R. Rotunno (1989). "Polar lows as arctic hurricanes". In: *Tellus A* 41A.1, pp. 1–17.

Field, P. R., A. Bodas-Salcedo, and M. E. Brooks (2011). "Using model analysis and satellite data to assess cloud and precipitation in midlatitude cyclones". In: *Quarterly Journal of the Royal Meteorological Society* 137.659, pp. 1501–1515.

Field, P. R. et al. (2014). "Improving a convection-permitting model simulation of a cold air outbreak". In: *Quarterly Journal of the Royal Meteorological Society* 140.678, pp. 124–138.

Fletcher, J., S. Mason, and C. Jakob (2016). "The Climatology, Meteorology, and Boundary Layer Structure of Marine Cold Air Outbreaks in Both Hemispheres*". In: *Journal of Climate* 29.6, pp. 1999–2014.

Forbes, G. S. and W. D. Lottes (1985). "Classification of mesoscale vortices in polar airstreams and the influence of the large-scale environment on their evolutions". In: *Tellus A* 37A.2, pp. 132–155.

Føre, I. et al. (2011). "The full life cycle of a polar low over the Norwegian Sea observed by three research aircraft flights". In: *Quarterly Journal of the Royal Meteorological Society* 137.660, pp. 1659–1673.

Føre, I. et al. (2012). "A 'hurricane-like' polar low fuelled by sensible heat flux: high-resolution numerical simulations". In: *Quarterly Journal of the Royal Meteorological Society* 138.666, pp. 1308–1324.

Forsythe, J. M. and J. M. Haynes (2015). "CloudSat Observes a Labrador Sea Polar Low". In: *Bulletin of the American Meteorological Society* 96.8, pp. 1229–1231.

Furevik, B. R. et al. (2015). "ASAR and ASCAT in Polar Low Situations". In: *Journal of Atmospheric and Oceanic Technology* 32, pp. 783–792.

Gallée, H. (1995). "Simulation of the Mesocyclonic Activity in the Ross Sea, Antarctica". In: *Monthly Weather Review* 123.7, pp. 2051–2069.

Gryschka, M. et al. (2008). "On the influence of sea-ice inhomogeneities onto roll convection in cold-air outbreaks". In: *Geophysical Research Letters* 35.23, p. L23804.

Hamilton, L. (2004). "The polar low phenomenon". In: *GEO Quaterly* 1, pp. 10–12.

Harold, J. M., G. R. Bigg, and J. Turner (1999a). "Mesocyclone activity over the North-East Atlantic. Part 1: Vortex distribution and variability". In: *International Journal of Climatology* 19.11, pp. 1187–1204.

— (1999b). "Mesocyclone activity over the Northeast Atlantic. Part 2: An investigation of causal mechanisms". In: *International Journal of Climatology* 19.12, pp. 1283–1299.

Heinemann, G. (1996). "A wintertime polar low over the eastern Weddell Sea (Antarctica): A study with AVHRR, TOVS, SSM/I and conventional data". In: *Meteorology and Atmospheric Physics* 58.1-4, pp. 83–102.

— (1997). "Idealized simulations of the Antarctic katabatic wind system with a three-dimensional mesoscale model". In: *Journal of Geophysical Research: Atmospheres* 102, pp. 825–834.

Hill, A. A. et al. (2014). "Mixed-phase clouds in a turbulent environment. Part 1: Large-eddy simulation experiments". In: *Quarterly Journal of the Royal Meteorological Society* 140.680, pp. 855–869.

Hoskins, B. J., M. E. McIntyre, and A. W. Robertson (1985). "On the use and significance of isentropic potential vorticity maps". In: *Quarterly Journal of the Royal Meteorological Society* 111.470, pp. 877–946.

Hoskins, B. J. and K. I. Hodges (2002). "New Perspectives on the Northern Hemisphere Winter Storm Tracks". In: *Journal of the Atmospheric Sciences* 59.6, pp. 1041–1061.

Hunter, J. D. (2007). "Matplotlib: A 2D Graphics Environment". In: *Computing in Science & Engineering* 9.3, pp. 90–95.

Irvine, E. A., S. L. Gray, and J. Methven (2011). "Targeted observations of a polar low in the Norwegian Sea". In: *Quarterly Journal of the Royal Meteorological Society* 137.660, pp. 1688–1699.

Joly, A. and A. J. Thorpe (1990). "Frontal instability generated by tropospheric potential vorticity anomalies". In: *Quarterly Journal of the Royal Meteorological Society* 116.493, pp. 525–560.

Kawashima, M. and Y. Fujiyoshi (2005). "Shear Instability Wave along a Snowband: Instability Structure, Evolution, and Energetics Derived from Dual-Doppler Radar Data". In: *Journal of the Atmospheric Sciences* 62, pp. 351–370.

Klein, S. A. et al. (2009). "Intercomparison of model simulations of mixed-phase clouds observed during the ARM Mixed-Phase Arctic Cloud Experiment. I: single-layer cloud". In: *Quarterly Journal of the Royal Meteorological Society* 135.641, pp. 979–1002.

Klein, T. and G. Heinemann (2002). "Interaction of katabatic winds and mesocyclones near the eastern coast of Greenland". In: *Meteorological Applications* 9.4, pp. 407–422.

Kolstad, E. W. and T. J. Bracegirdle (2017). "Sensitivity of an apparently hurricane-like polar low to sea-surface temperature". In: *Quarterly Journal of the Royal Meteorological Society* 143.703, pp. 966–973.

Kolstad, E. W. (2011). "A global climatology of favourable conditions for polar lows". In: *Quarterly Journal of the Royal Meteorological Society* 137.660, pp. 1749–1761.

Kolstad, E. W. and T. J. Bracegirdle (2008). "Marine cold-air outbreaks in the future: an assessment of IPCC AR4 model results for the Northern Hemisphere". In: *Climate Dynamics* 30.7-8, pp. 871–885.

Kolstad, E. W., T. J. Bracegirdle, and I. A. Seierstad (2009). "Marine cold-air outbreaks in the North Atlantic: temporal distribution and associations with large-scale atmospheric circulation". In: *Climate Dynamics* 33.2-3, pp. 187–197.

Korolev, A. V. et al. (1998). "The Nevzorov Airborne Hot-Wire LWC–TWC Probe: Principle of Operation and Performance Characteristics". In: *Journal of Atmospheric and Oceanic Technology* 15.6, pp. 1495–1510.

Korolev, A. V. et al. (2003). "Microphysical characterization of mixed-phase clouds". In: *Quarterly Journal of the Royal Meteorological Society* 129.587, pp. 39–65.

Kristiansen, J. et al. (2011). "High-resolution ensemble prediction of a polar low development". In: *Tellus A: Dynamic Meteorology and Oceanography* 63.3, pp. 585–604.

Kristjánsson, J. E., S. Thorsteinsson, and B. Røsting (2009). "Phase-locking of a rapidly developing extratropical cyclone by Greenland's orography". en. In: *Quarterly Journal of the Royal Meteorological Society* 135.645, pp. 1986–1998.

Kristjánsson, J. E. et al. (2011). "Orographic influence of east Greenland on a polar low over the Denmark Strait". In: *Quarterly Journal of the Royal Meteorological Society* 137.660, pp. 1773–1789.

Laffineur, T. et al. (2014). "Polar Lows over the Nordic Seas: Improved Representation in ERA-Interim Compared to ERA-40 and the Impact on Downscaled Simulations". In: *Monthly Weather Review* 142.6, pp. 2271–2289.

Linders, T. and Ø. Saetra (2010). "Can CAPE Maintain Polar Lows?" In: *Journal of the Atmospheric Sciences* 67.8, pp. 2559–2571.

Lloyd, G. et al. (2015). "Observations and comparisons of cloud microphysical properties in spring and summertime Arctic stratocumulus clouds during the ACCACIA campaign". In: *Atmospheric Chemistry and Physics* 15.7, pp. 3719–3737.

Mallet, P.-E., C. Claud, and M. Vicomte (2017). "North Atlantic polar lows and weather regimes: do current links persist in a warmer climate?" In: *Atmospheric Science Letters* 18.8, pp. 349–355.

Mallet, P.-E. et al. (2013). "Polar lows over the Nordic and Labrador Seas: Synoptic circulation patterns and associations with North Atlantic-Europe wintertime weather regimes". In: *Journal of Geophysical Research: Atmospheres* 118.6, pp. 2455–2472.

Mansfield, D. A. (1974). "Polar lows: The development of baroclinic disturbances in cold air outbreaks". In: *Quarterly Journal of the Royal Meteorological Society* 100.426, pp. 541–554.

Marshall, J. and F. Schott (1999). "Open-ocean convection: Observations, theory, and models". In: *Reviews of Geophysics* 37.1, pp. 1–64.

Matthews, A. J. and G. N. Kiladis (1999). "Interactions between ENSO, Transient Circulation, and Tropical Convectionover the Pacific". In: *Journal of Climate* 12.10, pp. 3062–3086.

McInnes, H. et al. (2011). "The role of horizontal resolution for polar low simulations". In: *Quarterly Journal of the Royal Meteorological Society* 137.660, pp. 1674–1687.

Melia, N., K. Haines, and E. Hawkins (2016). "Sea ice decline and 21st century trans-Arctic shipping routes". In: *Geophysical Research Letters* 43.18, pp. 9720–9728.

Met Office (2016). *Iris: A Python library for analysing and visualising meteorological and oceanographic data sets*.

Michel, C., A. Terpstra, and T. Spengler (2018). "Polar Mesoscale Cyclone Climatology for the Nordic Seas Based on ERA-Interim". In: *Journal of Climate* 31.6, pp. 2511–2532.

Montgomery, M. T., J. Persing, and R. K. Smith (2015). "Putting to rest WISHE-ful misconceptions for tropical cyclone intensification". In: *Journal of Advances in Modeling Earth Systems* 7.1, pp. 92–109.

Montgomery, M. T. and R. K. Smith (2014). "Paradigms for tropical cyclone intensification". In: *Australian Meteorological and Oceanographic Journal* 64, pp. 37–66.

Montgomery, M. and B. Farrell (1992). "Polar low dynamics". In: *Journal of the Atmospheric Sciences*.

Moore, G. W. K. and I. A. Renfrew (2005). "Tip Jets and Barrier Winds: A QuikSCAT Climatology of High Wind Speed Events around Greenland". In: *Journal of Climate* 18.18, pp. 3713–3725.

Moore, G. W. K. and P. W. Vachon (2002). "A polar low over The Labrador Sea: Interactions with topography and an upper-level potential vorticity anomaly, and an observation by RADARSAT-1 SAR". In: *Geophysical Research Letters* 29.16, pp. 20–1.

Moore, G. W. K. et al. (2015a). "Decreasing intensity of open-ocean convection in the Greenland and Iceland seas". In: *Nature Climate Change* 5.9, pp. 877–882.

Moore, G. W. K. et al. (2015b). "The impact of resolution on the representation of southeast Greenland barrier winds and katabatic flows". In: *Geophysical Research Letters* 42.8, pp. 3011–3018.

Moore, R. W. and M. T. Montgomery (2005). "Analysis of an Idealized, Three-Dimensional Diabatic Rossby Vortex: A Coherent Structure of the Moist Baroclinic Atmosphere". In: *Journal of the Atmospheric Sciences* 62.8, pp. 2703–2725.

Nagata, M. (1993). "Meso-β-scale Vortices Developing along the Japan-Sea Polar-Airmass Convergence Zone (JPCZ)Cloud Band : Numerical Simulation". In: *Journal of the Meteorological Society of Japan. Ser. II* 71.1, pp. 43–57.

Neu, U. et al. (2013). "Imilast: A community effort to intercompare extratropical cyclone detection and tracking algorithms". In: *Bulletin of the American Meteorological Society* 94.4, pp. 529–547.

Nielsen, N. W. (1997). "An early-autumn polar low formation over the Norwegian Sea". In: *Journal of Geophysical Research: Atmospheres* 102.D12, pp. 13955–13973.

Noer, G. et al. (2011). "A climatological study of polar lows in the Nordic Seas". In: *Quarterly Journal of the Royal Meteorological Society* 137.660, pp. 1762–1772.

Nordeng, T. E. and E. A. Rasmussen (1992). "A most beautiful polar low. A case study of a polar low development in the Bear Island region". In: *Tellus A* 44.2, pp. 81–99.

Nordeng, T. E. and B. Røsting (2011). "A polar low named Vera: the use of potential vorticity diagnostics to assess its development". In: *Quarterly Journal of the Royal Meteorological Society* 137.660, pp. 1790–1803.

Økland, H. (1987). "Heating by organized convection as a source of polar low intensification". In: *Tellus A* 39A.4, pp. 397–407.

Ólafsson, H. and P. Bougeault (1997). "The effect of rotation and surface friction on orographic drag". In: *Journal of the Atmospheric Sciences* 54.1, pp. 193–210.

Orlanski, I. (1975). "A Rational Subdivision of Scales for Atmospheric Processes". In: *Bulletin of the American Meteorological Society* 56.5, pp. 527–530.

Outten, S. D., I. A. Renfrew, and G. N. Petersen (2009). "An easterly tip jet off Cape Farewell, Greenland. II: Simulations and dynamics". en. In: *Quarterly Journal of the Royal Meteorological Society* 135.645, pp. 1934–1949.

Overland, J. E. and M. Wang (2007). "Future regional Arctic sea ice declines". In: *Geophysical Research Letters* 34.17, p. L17705.

Pagowski, M. and G. W. K. Moore (2001). "A Numerical Study of an Extreme Cold-Air Outbreak over the Labrador Sea: Sea Ice, Air–Sea Interaction, and Development of Polar Lows". In: *Monthly Weather Review* 129.1, pp. 47–72.

Papritz, L. and T. Spengler (2017). "A Lagrangian climatology of wintertime cold air outbreaks in the Irminger and Nordic Seas and their role in shaping air-sea heat fluxes". In: *Journal of Climate* 30.8, pp. 2717–2737.

Parker, D. J. and A. J. Thorpe (1995). "Conditional Convective Heating in a Baroclinic Atmosphere: A Model of Convective Frontogenesis". In: *Journal of the Atmospheric Sciences* 52.10, pp. 1699–1711.

Petersen, G. N., I. A. Renfrew, and G. W. K. Moore (2009). "An overview of barrier winds off southeastern Greenland during the Greenland Flow Distortion experiment". In: *Quarterly Journal of the Royal Meteorological Society* 135.645, pp. 1950–1967.

Petersen, G. N., H. Ólafsson, and J. E. Kristjánsson (2003). "Flow in the Lee of Idealized Mountains and Greenland". In: *Journal of the Atmospheric Sciences* 60.17, pp. 2183–2195.

Rae, J. G. et al. (2017). "How much should we believe correlations between Arctic cyclones and sea ice extent?" In: *Cryosphere* 11.6, pp. 3023–3034.

Rasmussen, E. (1979). "The polar low as an extratropical CISK disturbance". en. In: *Quarterly Journal of the Royal Meteorological Society* 105.445, pp. 531–549.

Rasmussen, E. (1981). "An Investigation of a Polar Low with a Spiral Cloud Structure". In: *Journal of the Atmospheric Sciences* 38.8, pp. 1785–1792.

Rasmussen, E. A. and J. Turner (2003). *Polar Lows: Mesoscale Weather Systems in the Polar Regions*.

Reed, R. J. and C. N. Duncan (1987). "Baroclinic instability as a mechanism for the serial development of polar lows: a case study". In: *Tellus A* 39A.4, pp. 376–384.

Reeve, M. A. and E. W. Kolstad (2011). "The Spitsbergen South Cape tip jet". en. In: *Quarterly Journal of the Royal Meteorological Society* 137.660, pp. 1739–1748.

Renfrew, I. A. et al. (2008). "The Greenland Flow Distortion Experiment". In: *Bulletin of the American Meteorological Society* 89.9, pp. 1307–1324.

Renfrew, I. A. et al. (2009a). "A comparison of aircraft-based surface-layer observations over Denmark Strait and the Irminger Sea with meteorological analyses and QuikSCAT winds". In: *Quarterly Journal of the Royal Meteorological Society* 135.645, pp. 2046–2066.

Renfrew, I. A. (2003). "Polar lows". In: *Encyclopedia of Atmospheric Sciences*. Elsevier, pp. 1761–1768.

Renfrew, I. A., S. D. Outten, and G. W. K. Moore (2009b). "An easterly tip jet off Cape Farewell, Greenland. I: Aircraft observations". en. In: *Quarterly Journal of the Royal Meteorological Society* 135.645, pp. 1919–1933.

Rojo, M. et al. (2015). "Polar low tracks over the Nordic Seas: a 14-winter climatic analysis". In: *Tellus A: Dynamic Meteorology and Oceanography* 67.1, p. 24660.

Romero, R. and K. Emanuel (2017). "Climate Change and Hurricane-Like Extratropical Cyclones: Projections for North Atlantic Polar Lows and Medicanes Based on CMIP5 Models". In: *Journal of Climate* 30.1, pp. 279–299.

Sardie, J. M. and T. T. Warner (1983). "On the Mechanism for the, Development of Polar Lows". In: *Journal of the Atmospheric Sciences* 40.4, pp. 869–881.

Schär, C. and H. C. Davies (1990). "An Instability of Mature Cold Fronts". In: *Journal of the Atmospheric Sciences* 47.8, pp. 929–950.

Schär, C. and R. B. Smith (1993a). "Shallow-Water Flow past Isolated Topography. Part I: Vorticity Production and Wake Formation". In: *Journal of the Atmospheric Sciences* 50, pp. 1373–1400.

— (1993b). "Shallow-Water Flow past Isolated Topography. Part II: Transition to Vortex Shedding". In: *Journal of the Atmospheric Sciences* 50, pp. 1401–1412.

Sergeev, D. E. et al. (2017). "Structure of a shear-line polar low". In: *Quarterly Journal of the Royal Meteorological Society* 143.702, pp. 12–26.

Shapiro, M. A., L. S. Fedor, and T. Hampel (1987). "Research aircraft measurements of a polar low over the Norwegian Sea". In: *Tellus A* 39A.4, pp. 272–306.

Shimada, U. et al. (2014). "Roles of an upper-level cold vortex and low-level baroclinicity in the development of polar lows over the Sea of Japan". In: *Tellus A: Dynamic Meteorology and Oceanography* 66.1, p. 24694.

Sinclair, M. R. (1994). "An Objective Cyclone Climatology for the Southern Hemisphere". In: *Monthly Weather Review* 122.10, pp. 2239–2256.

Skeie, P. and S. Grønås (2000). "Strongly stratified easterly flows across Spitsbergen". In: *Tellus A: Dynamic Meteorology and Oceanography* 52.5, pp. 473–486.

Smirnova, J. E. et al. (2015). "Polar low climatology over the Nordic and Barents seas based on satellite passive microwave data". In: *Geophysical Research Letters* 42.13, pp. 5603–5609.

Smirnova, J. and P. Golubkin (2017). "Comparing polar lows in atmospheric reanalyses: Arctic System Reanalysis versus ERA-Interim". In: *Monthly Weather Review* 145, pp. 2375–2383.

Smith, R. B. (1989a). "Hydrostatic Airflow over Mountains". In: *Advances in Geophysics* 31.C, pp. 1–41.

— (1989b). "Mountain-induced stagnation points in hydrostatic flow". In: *Tellus A* 41A.3, pp. 270–274.

Spengler, T. et al. (2016). "High-Latitude Dynamics of Atmosphere–Ice–Ocean Interactions". In: *Bulletin of the American Meteorological Society* 97.9, ES179–ES182.

Sprenger, M. and H. Wernli (2015). "The LAGRANTO Lagrangian analysis tool – version 2.0". In: *Geoscientific Model Development* 8.8, pp. 2569–2586.

Stoll, P. et al. (2018). "An objective global climatology of polar lows based on reanalysis data". In: *Quarterly Journal of the Royal Meteorological Society*.

Tang, C. K. and J. C. L. Chan (2014). "Idealized simulations of the effect of Taiwan and Philippines topographies on tropical cyclone tracks". In: *Quarterly Journal of the Royal Meteorological Society* 140.682, pp. 1578–1589.

— (2015). "Idealized simulations of the effect of local and remote topographies on tropical cyclone tracks". In: *Quarterly Journal of the Royal Meteorological Society* 141.691, pp. 2045–2056.

Terpstra, A., C. Michel, and T. Spengler (2016). "Forward and reverse shear environments during polar low genesis over the North East Atlantic". In: *Monthly Weather Review*.

Terpstra, A., T. Spengler, and R. W. Moore (2015). "Idealised simulations of polar low development in an Arctic moist-baroclinic environment". In: *Quarterly Journal of the Royal Meteorological Society* 141.691, pp. 1987–1996.

Tilinina, N., S. K. Gulev, and D. H. Bromwich (2014). "New view of Arctic cyclone activity from the Arctic system reanalysis". In: *Geophysical Research Letters* 41.5, pp. 1766–1772.

Tilinina, N. et al. (2013). "Comparing cyclone life cycle characteristics and their interannual variability in different reanalyses". In: *Journal of Climate* 26.17, pp. 6419–6438.

Tourville, N. et al. (2015). "Remote Sensing of Tropical Cyclones: Observations from CloudSat and A-Train Profilers". In: *Bulletin of the American Meteorological Society* 96.April, pp. 609–622.

Valkonen, T., H. Schyberg, and J. Figa-Saldana (2017). "Assimilating Advanced Scatterometer Winds in a High-Resolution Limited Area Model Over Northern Europe". In: *IEEE Journal of Selected Topics in Applied Earth Observations and Remote Sensing* 10.5, pp. 2394–2405.

Vallis, G. K. (2006). *Atmospheric and Oceanic Fluid Dynamics*. Cambridge, U.K.: Cambridge University Press, p. 745.

Vaughan, D. G. et al. (2013). "Observations: Cryosphere". In: *Climate Change 2013: The Physical Science Basis. Contribution of Working Group I to the Fifth Assessment Report of the Intergovernmental Panel on Climate Change*. Ed. by T. F. Stocker et al. Cambridge, United Kingdom and New York, NY, USA: Cambridge University Press. Chap. 4, pp. 317–382.

Verezemskaya, P. S. and V. M. Stepanenko (2016). "Numerical simulation of the structure and evolution of a polar mesocyclone over the Kara Sea. Part 1. Model validation and estimation of instability mechanisms". In: *Russian Meteorology and Hydrology* 41.6, pp. 425–434.

Verezemskaya, P. et al. (2017). "Southern Ocean mesocyclones and polar lows from manually tracked satellite mosaics". In: *Geophysical Research Letters* 44.15, pp. 7985–7993.

Wagner, J. S. et al. (2011). "The mesoscale structure of a polar low: airborne lidar measurements and simulations". In: *Quarterly Journal of the Royal Meteorological Society* 137.659, pp. 1516–1531.

Walters, D. et al. (2017). "The Met Office Unified Model Global Atmosphere 6.0/6.1 and JULES Global Land 6.0/6.1 configurations". In: *Geoscientific Model Development* 10.4, pp. 1487–1520.

Watanabe, S.-i. I. and H. Niino (2014). "Genesis and Development Mechanisms of a Polar Mesocyclone over the Japan Sea". In: *Monthly Weather Review* 142.6, pp. 2248–2270.

Watanabe, S.-i. I., H. Niino, and W. Yanase (2016). "Climatology of Polar Mesocyclones over the Sea of Japan Using a New Objective Tracking Method". In: *Monthly Weather Review* 144.7, pp. 2503–2515.

— (2017). "Structure and Environment of Polar Mesocyclones over the Northeastern Part of the Sea of Japan". In: *Monthly Weather Review* 145.6, pp. 2217–2233.

— (2018). "Composite Analysis of Polar Mesocyclones over the Western Part of the Sea of Japan". In: *Monthly Weather Review* 146.4, pp. 985–1004.

Webster, S. et al. (2003). "Improvements to the representation of orography in the Met Office Unified Model". In: *Quarterly Journal of the Royal Meteorological Society* 129.591, pp. 1989–2010.

Wilhelmsen, K. (1985). "Climatological study of gale-producing polar lows near Norway". In: *Tellus A* 37 A.5, pp. 451–459.

Wilson, D. R. and S. P. Ballard (1999). "A microphysically based precipitation scheme for the UK meteorological office unified model". In: *Quarterly Journal of the Royal Meteorological Society* 125.557, pp. 1607–1636.

Wood, N. et al. (2014). "An inherently mass-conserving semi-implicit semi-Lagrangian discretization of the deep-atmosphere global non-hydrostatic equations". In: *Quarterly Journal of the Royal Meteorological Society* 140.682, pp. 1505–1520.

Wu, L., J. E. Martin, and G. W. Petty (2011). "Piecewise potential vorticity diagnosis of the development of a polar low over the Sea of Japan". In: *Tellus A: Dynamic Meteorology and Oceanography* 63.2, pp. 198–211.

Xia, L. et al. (2012). "A comparison of two identification and tracking methods for polar lows". In: *Tellus A: Dynamic Meteorology and Oceanography* 64.1, p. 17196.

Yanase, W. and H. Niino (2007). "Dependence of Polar Low Development on Baroclinicity and Physical Processes: An Idealized High-Resolution Numerical Experiment". In: *Journal of the Atmospheric Sciences* 64.9, pp. 3044–3067.

Yanase, W. et al. (2016). "Climatology of Polar Lows over the Sea of Japan Using the JRA-55 Reanalysis". In: *Journal of Climate* 29.2, pp. 419–437.

Yarnal, B. and K. G. Henderson (1989). "A Climatology of Polar Low Cyclogenetic Regions over the North Pacific Ocean". In: *Journal of Climate* 2.12, pp. 1476–1491.

Zabolotskikh, E. V., I. A. Gurvich, and B. Chapron (2016). "Polar Lows over the Eastern Part of the Eurasian Arctic: The Sea-Ice Retreat Consequence". In: *IEEE Geoscience and Remote Sensing Letters* 13.10, pp. 1492–1496.

Zabolotskikh, E. V., L. M. Mitnik, and B. Chapron (2013). "New approach for severe marine weather study using satellite passive microwave sensing". In: *Geophysical Research Letters* 40.April, pp. 3347–3350.

Zahn, M. and H. von Storch (2008). "A long-term climatology of North Atlantic polar lows". In: *Geophysical Research Letters* 35.22, p. L22702.

— (2010). "Decreased frequency of North Atlantic polar lows associated with future climate warming". In: *Nature* 467.7313, pp. 309–312.

Zahn, M., H. von Storch, and S. Bakan (2008). "Climate mode simulation of North Atlantic polar lows in a limited area model". In: *Tellus A* 60.4, pp. 620–631.

Zappa, G., L. Shaffrey, and K. Hodges (2014). "Can Polar Lows be Objectively Identified and Tracked in the ECMWF Operational Analysis and the ERA-Interim Reanalysis?" In: *Monthly Weather Review* 142.8, pp. 2596–2608.

Zhang, J. et al. (2013). "The impact of an intense summer cyclone on 2012 Arctic sea ice retreat". In: *Geophysical Research Letters* 40.4, pp. 720–726.

Zolina, O. and S. K. Gulev (2002). "Improving the Accuracy of Mapping Cyclone Numbers and Frequencies". In: *Monthly Weather Review* 130.1925, pp. 748–759.